University of California
Santa Barbara

Future Networks of Gravitational Wave Detectors: Quantum Noise and Space Detectors

A dissertation submitted in partial satisfaction
of the requirements for the degree

Doctor of Philosophy
in
Physics

by

Kevin A. Kuns

Committee in charge:

Professor Donald Marolf, Chair
Professor Gary Horowitz
Professor Mark Sherwin
Professor Rana Adhikari

March 2019

The Dissertation of Kevin A. Kuns is approved.

Professor Gary Horowitz

Professor Mark Sherwin

Professor Rana Adhikari

Professor Donald Marolf, Committee Chair

March 2019

Future Networks of Gravitational Wave Detectors:

Quantum Noise and Space Detectors

by

Kevin A. Kuns

Acknowledgements

Since I've taken a long and winding road through grad school, there are many people to thank.

First, I thank my advisor Don. He was a patient mentor when I was working with him on holography and always showed an interest in my career. He has never hesitated to help me and I am especially grateful for his patience in advising me remotely from UCSB while I have been living at Caltech for the past year and a half. I know it has not been easy, but I don't think I would have continued with a career in science if it wasn't for this opportunity to work on gravitational wave detection, and I appreciate his effort in making this work.

So I am, of course, equally grateful to Rana for mentoring me in his lab as an undergrad and then inviting me back seven years later to give me this second chance at a science career. I am constantly surprised by how much time he spends with me and the rest of the group. Through a steady stream of entertainment, I have been able to distill not only valuable physics knowledge, but examples of what it means to do science honestly and precisely. Now I hope I can do so myself.

I thank Boris for letting me try biophysics for awhile. He always showed genuine care for my well being and was always eager and available to talk. In addition to being brilliant, he is also one of the kindest scientists I have ever met.

Thanks to Yanbei for countless discussions about fundamental physics and for always being 10 dB more excited than anyone else in the room. And I thank Koji for his reliable interferometric wisdom.

I am especially grateful to Gautam for teaching me many practical things about how interferometers really work. I am also grateful to some of the other LIGO Caltech group members, Andrew, Johannes, Aaron, Chris, Craig, Anchal, Tom, Michael, and Zach, for

their friendship and knowledge, and to Jamie for having my back.

I thank the many UCSB colleagues on the sixth floor, Sebastian, Eric, Gavin, Christina, Teddy, Brayden, Keith, Ben, Will, Alex, Netta, Jason, Nick, Ahmed, and Milind. I have learned much about many areas of physics from them and they have been reliable friends as well.

I thank Alois Zauner for saving my brain. Without his hard work this thesis would have been physically impossible to complete. And I am indebted to Joe for conversations about brains and branes. Talking with Joe about brains was one of the most useful things I did in getting through grad school, and talking with him about branes was an honor.

Thanks to my roommates Eric and Naomi. In addition to becoming close friends, and Eric a valuable colleague, their help and support was crucial in getting through difficult times.

And finally, I thank my parents, Kyle and Debbie, who kindled my love of science from an early age and, together with my sister Sarah, encouraged me to finish this thesis despite the long, and at many points difficult, road it has taken.

Curriculum Vitæ

Kevin A. Kuns

Education

2019	Ph.D. in Physics (Expected), University of California, Santa Barbara.
2017	M.A. in Physics, University of California, Santa Barbara.
2012	B.S. in Physics, California Institute of Technology.

Publications

1. K. A. Kuns, A. M. Rey, and A. V. Gorshkov. *d-wave superfluidity in optical lattices of ultracold polar molecules.* Phys. Rev. A **84**, 063639 (2011); arXiv:1110.5330.
2. K. Kuns and D. Marolf. *Non-thermal behavior in conformal boundary states.* JHEP **09** (2014) 082; arXiv:1406.4926.
3. W. R. Kelley, K. Kuns, and D. Marolf. *'t Hooft suppression and holographic entropy.* JHEP **10** (2015) 059; arXiv:1507.03654.

Abstract

Future Networks of Gravitational Wave Detectors:

Quantum Noise and Space Detectors

by

Kevin A. Kuns

The current network of three terrestrial interferometric gravitational wave detectors have observed ten binary black holes and one binary neutron star to date in the frequency band from 10 Hz to 5 kHz. Future detectors will increase the sensitivity by up to a factor of 10 and will push the sensitivity band down to lower frequencies. However, observing sources lower than a few Hz requires going into space where the interferometer arms can be longer and where there is no seismic noise. A new 100 km space detector, TianGO, sensitive to the frequency band from 10 mHz to 100 Hz is described. Through its excellent ability to localize sources in the sky, TianGO can use binary black holes as standard candles to help resolve the current tension between measurements of the Hubble constant. Furthermore, all of the current and future detectors, on both the ground and in space, are limited by quantum shot noise at high frequencies, and some will be limited by quantum radiation pressure at low frequencies as well. Much effort is made to use squeezed states of light to reduce this quantum noise, however classical noise and losses severely limit this reduction. One would ideally design a gravitational wave transducer that, using its own ability to generate ponderomotive squeezing due to the radiation pressure mediated interaction between the optical modes of the light and the mechanical modes of the mirrors, approaches the fundamental limits to quantum measurement. First steps in this direction are described and it is shown that it is feasible that a large scale 40 m interferometer can observe this ponderomotive squeezing in the near future. Finally,

a method of removing the effects of the vacuum fluctuations responsible for the quantum noise in gravitational wave detectors and its application to testing for the presence of deviations from general relativity is described.

Contents

List of Figures

List of Tables

Chapter 1

Introduction

The ground based network of interferometric gravitational wave detectors, consisting of the LIGO observatories in Hanford and Livingston [1] and the Virgo observatory in Italy [2], have detected ten binary black holes and one binary neutron star to date [3–5]. The KAGRA detector in Japan [6] will join LIGO and Virgo soon, and construction on a third LIGO site in India will begin shortly. While not as sensitive as these detectors at lower frequencies, the GEO600 detector in Germany [7] is also part of this global network of detectors.

1.1 Future Gravitational Wave Detectors

With the focus of the current detectors moving from making the first detections to being a network of observatories routinely detecting sources, studies for the future of gravitational wave detectors are underway and focus on improvements to the current network in two ways. First, improving the sensitivity of the next generation of detectors, and, second, expanding the frequency range over which the network can observe. Fig. 1.1 shows the sensitivities of possible future detectors.

LIGO Voyager is a cryogenic upgrade to the existing LIGO facilities [8], and Cosmic Explorer (CE) would be a 40 km long interferometer [9, 10]. The Einstein Telescope (ET)

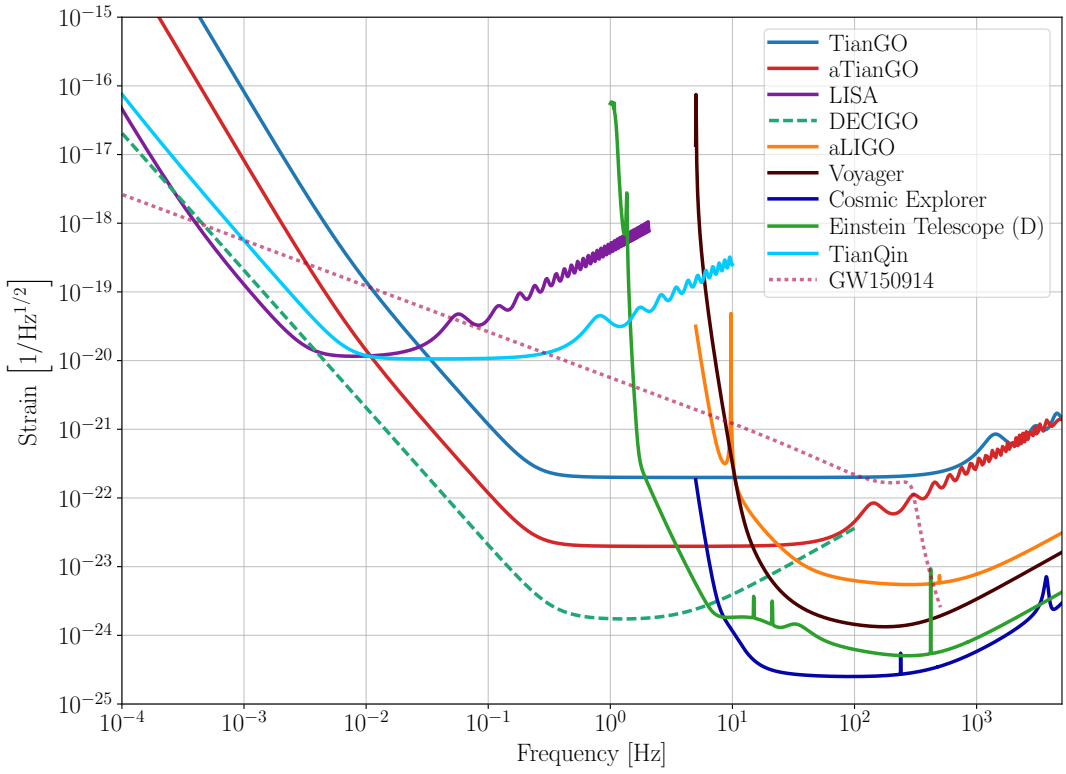

Figure 1.1: Sensitivities of future ground and space gravitational wave detectors. The trace labeled GW150914 is the waveform of the first direct detection of gravitational waves.

would be a set of six 10 km long interferometers forming an equilateral triangle [11–13]. Each corner has two interferometers: one cryogenic low-frequency interferometer and one high frequency interferometer.

These ground-based detectors are limited by seismic noise at low frequencies and cannot observe lower than a few Hz in the best case of ET. To see lower frequency sources, one needs to use space detectors which are not affected by these noises and where the arms can be significantly longer than ground-based interferometers.

LISA (Laser Interferometer Space Antenna) is perhaps the best known and furthest developed space detector [14]. It consists of three spacecraft in a triangular configuration forming three interferometers with 2×10^6 km long arms. The three satellite constellation is in a heliocentric orbit trailing the Earth by 20°. It uses time-delay interferometry with a 2 W, 1064 nm laser and 2 kg test masses. LISA is briefly discussed in Chap. 5. TianQin is similar to LISA but with 10^5 km long arms, a 4 W laser, and is in a geocentric orbit [15]. DECIGO is another three spacecraft constellation in a heliocentric Earth trailing orbit, but it has 1000 km long arms and does traditional interferometry [16, 17]. DECIGO's arms are Fabry-Perot cavities (with a finesse of 10) and it uses a 10 W, 515 nm laser with 100 kg test masses.

TianGO is a relatively simple and cheap space detector and is described in Chap. 5. TianGO has three satellites with 100 km long arms that form a simple Michelson interferometer and which will also likely be in a heliocentric Earth trailing orbit. It uses a 5 W, 532 nm laser with 10 kg test masses and employs 10 dB of phase squeezing to reduce quantum noise. Advanced TianGO (aTianGO) is a speculative idea that would use large lightweight foldable mirrors that would allow it to have 1000 km long arms.

The astrophysical reach of most of the detectors shown in Fig. 1.1 to compact binary systems is shown in Fig. 1.2 as a function of the total mass of the binary system. The ground detectors are sensitive to lower mass systems because they are sensitive to higher

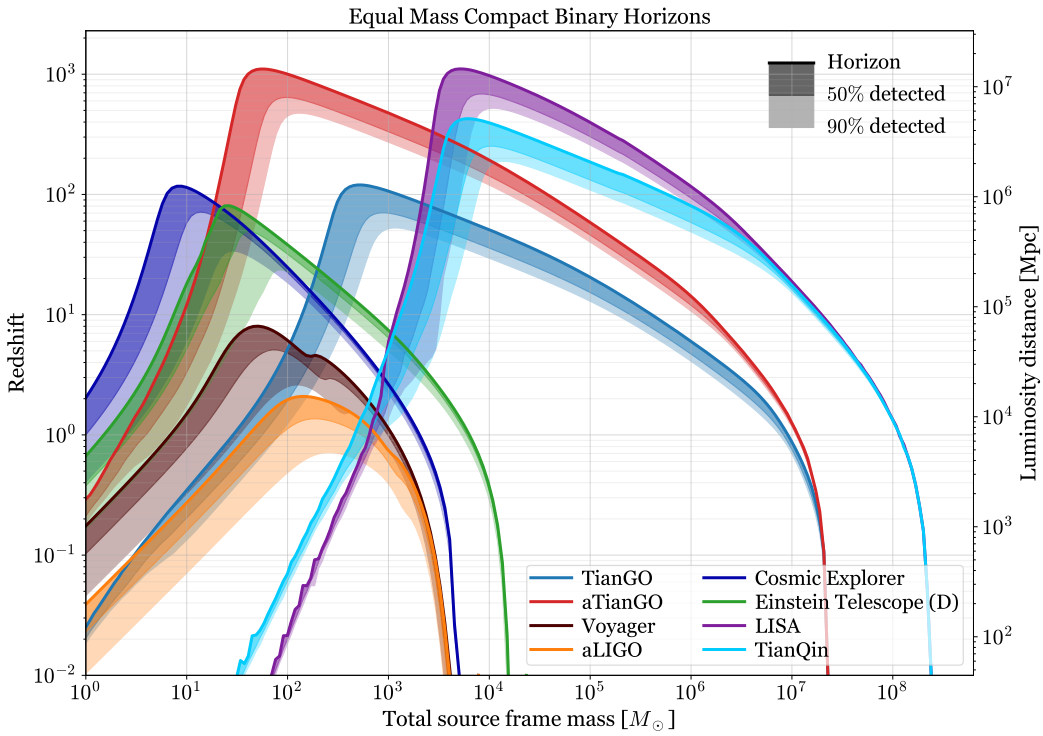

Figure 1.2: Compact binary horizons for different ground and space detectors. The binary systems are equal mass and oriented face on. The maximum detectable distance, defined as the distance at which a source has an SNR of 8 in a given detector, is computed for 48 source locations uniformly tiling the sky. The horizon is the maximum distance at which the best source is detected, 50% of these sources are detected within the dark shaded band, and 90% of the sources are detected within the light shaded band. If a source stays in a space detector's sensitivity band for more than 5 years, the 5 year portion of the system's evolution that gives the best SNR in each detector is used.

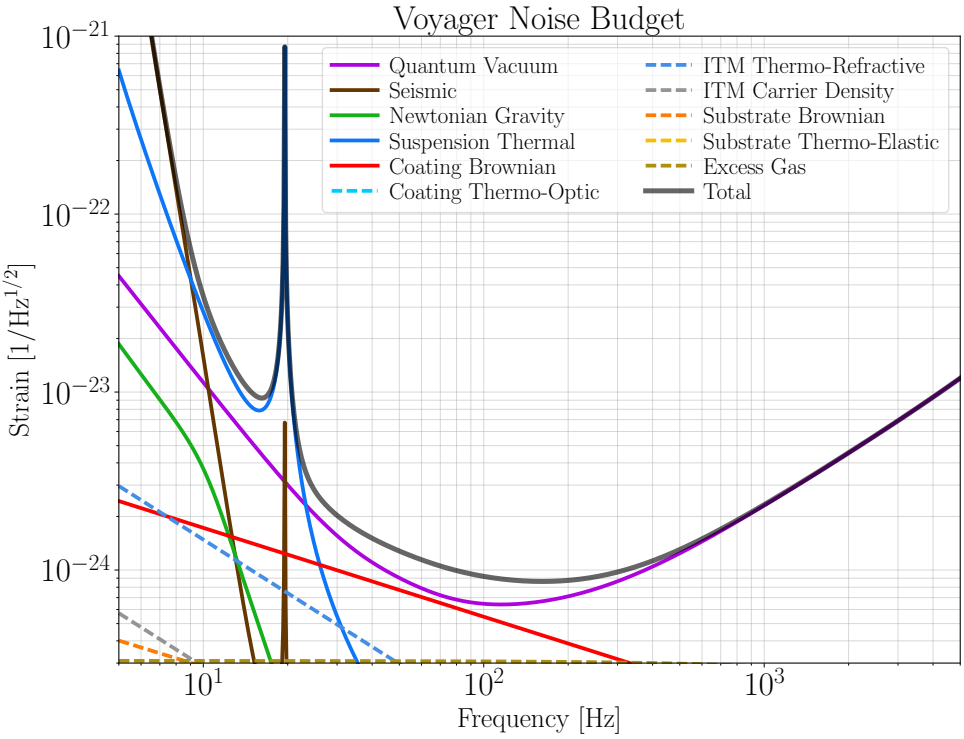

Figure 1.3: Voyager noise budget. The interferometer will be dominated by quantum noise from 20 Hz and above.

frequencies than the space detectors. The horizon is the furthest distance a given detector could see an optimally oriented source in the optimal orientation in the sky. The figure also shows how far a given detector can see binary systems that are not at the optimal orientation in the sky. A source is said to be detectable if it has a signal to noise ratio (SNR) of at least 8 in a given detector.

1.2 Quantum Noise in Gravitational Wave Detectors

All of the detectors shown in Fig. 1.1 will be limited by quantum shot noise at high frequencies, and some will be limited by quantum radiation pressure at low frequencies. The noise budget for LIGO Voyager [8] is shown in Fig. 1.3 and shows that the detector will be limited by quantum noise at all frequencies above 20 Hz, though coating Brownian

noise makes a significant contribution around 100 Hz. Since quantum noise is so important, much effort is made to use squeezed states of light in interferometers to reduce this noise. The relevant aspects of quantum noise are briefly reviewed in Sec. 2.1.

These fragile quantum states thus need to be protected from losses and other classical noises. A good way to do this is to get the interferometer to amplify the signal, and noise, itself through optomechanical interactions, known as ponderomotive squeezing [18], before the signal encounters the large sources of noise and losses. Sec. 2.2 introduces ponderomotive squeezing and Sec. 2.3 discusses the detrimental effects of losses and classical noise on quantum states and their mitigation with optomechanical amplifiers. Chap. 3 discusses progress towards observing ponderomotive squeezing in a large scale 40 m interferometer.

Finally, the source of quantum noise in gravitational wave detectors is the beating of vacuum fluctuations of the electromagnetic field with the strong laser, known as the local oscillator (LO), needed to detect the signals. Chap. 4 describes a scheme to remove the LO, and thus be free from the quantum noise of the vacuum fluctuations, when looking for deviations from general relativity (GR). To do so, the interferometer mirrors are driven in such a way that the predicted signal from general relativity is canceled; any signal exiting the interferometer thus signals a modification to GR. By counting photons instead of measuring the signal, the need for a local oscillator is removed and the noise due to the vacuum fluctuations is eliminated.

1.3 Permissions and Attributions

1. The content of Sec. 2.3 is the result of discussions with Rana Adhikari, Yanbei Chen, Gautam Venugopalan, Yuntao Bai, Aaron Markowitz, Chris Wipf, and Haixing Miao.

2. The content of Chap. 4 is the result of a collaboration with Zachary Mark, Rana Adhikari, and Yanbei Chen and is based off of a rough draft of a paper to be submitted soon.

3. The content of Chap. 5 is the result of a collaboration with Rana Adhikari and Geoffrey Lovelace and is based off of a rough draft of a paper to be submitted soon.

4. The content of Appendix. B is a slightly more detailed analysis of an idea due to Koji Arai [19] which is necessary for part of a noise analysis in Sec. 3.4.

Chapter 2

Quantum Noise in Optomechanical Systems

This chapter very briefly reviews quantum noise in states of the electromagnetic field in Sec. 2.1. Then Sec. 2.2 introduces the optomechanical interactions that are important in the rest of this thesis and explains their effects on quantum noise. Finally, Sec. 2.3 explains how classical noise degrades quantum states and describes schemes using these optomechanical interactions to ameliorate these effects.

2.1 Quantum States of the Electromagnetic Field and Their Noise

2.1.1 Quantization of the Electromagnetic Field

In this section we very briefly review the semiclassical quantization of the electromagnetic field. See, for example, Refs. [20–22] for more details. All topics in this thesis occur at sufficiently low energies that matter does not need to be quantized.

For simplicity, we consider a single polarization of the electromagnetic field describing a laser beam with an effective cross sectional area $\mathcal{A}$. To quantize the field, one starts by

expanding the electromagnetic field in a set of normal modes [23–26]

$$E(t) = \int_0^\infty \frac{\mathrm{d}\omega}{2\pi}\sqrt{\frac{2\pi\hbar\omega}{\mathcal{A}c}}a(\omega)\,\mathrm{e}^{-\mathrm{i}\omega t} + \mathrm{h.c.} \tag{2.1}$$

where $a(\omega)$ is the annihilation operator for the mode of frequency ω which is quantized according to

$$[a(\omega), a^\dagger(\omega')] = 2\pi\delta(\omega-\omega'), \qquad [a(\omega), a(\omega')] = 0. \tag{2.2}$$

Note that we will always be interested in evaluating fields at a particular point in space and so fields will be written as a function of time only.

For applications to interferometric gravitational wave detectors, it is inconvenient to use (2.1) directly. The lasers used in these interferometers have wavelengths of order $1\,\mu$m which corresponds to frequencies of order $\omega_0/2\pi = 300\,\mathrm{THz}$. On the other hand, the gravitational waves themselves have frequencies $\Omega/2\pi$ ranging from roughly 10^{-4} Hz for some space detectors to 10^4 Hz for the ground detectors. These signals that we are interested in detecting are imprinted on the light as phase fluctuations on top of the carrier oscillating at ω_0. The detectors do not directly measure signals at ω_0 but instead optically demodulate[1] the signals to measure the gravitational wave signals oscillating at Ω. It is thus convenient to have a description of the electromagnetic field in terms of the demodulated signal frequencies which is provided by the two-photon formalism [23, 24]. One defines the annihilation operators for the upper and lower signal sidebands as

$$a_\pm(\Omega) \equiv a(\omega_0 \pm \Omega)\sqrt{1 \pm \frac{\Omega}{\omega_0}} \approx a(\omega_0 \pm \Omega). \tag{2.3}$$

The only nonzero commutators are

$$[a_+(\Omega), a_+^\dagger(\Omega)] = 2\pi\,\delta(\Omega-\Omega')\left(1+\frac{\Omega}{\omega_0}\right) \approx 2\pi\,\delta(\Omega-\Omega') \tag{2.4a}$$

$$[a_-(\Omega), a_-^\dagger(\Omega)] = 2\pi\,\delta(\Omega-\Omega')\left(1-\frac{\Omega}{\omega_0}\right) \approx 2\pi\,\delta(\Omega-\Omega'). \tag{2.4b}$$

[1] This demodulation is done by combining the signal light with another beam, the local oscillator, before being measured on a photodiode. Appendix. B describes one method of doing this, known as homodyne detection, where the local oscillator is at the same frequency ω_0 as the signal field.

Since $\Omega/\omega_0 \ll 1$ for our applications, the Ω/ω_0 terms will be neglected.

In terms of the sideband annihilation operators (2.3), the field quantization (2.1) becomes

$$E(t) = \sqrt{\frac{2\pi\hbar\omega_0}{\mathcal{A}c}}\, \mathrm{e}^{-\mathrm{i}\omega_0 t} \int_0^\infty \frac{\mathrm{d}\Omega}{2\pi} \left[a_+(\Omega)\, \mathrm{e}^{-\mathrm{i}\Omega t} + a_-(\Omega)\, \mathrm{e}^{\mathrm{i}\Omega t}\right] + \mathrm{h.c.} \tag{2.5}$$

It is now useful to define the two-photon modes

$$a_1(\Omega) = \frac{1}{\sqrt{2}}\left[a_+(\Omega) + a_-^\dagger(\Omega)\right], \qquad a_2(\Omega) = \frac{1}{\sqrt{2}\mathrm{i}}\left[a_+(\Omega) - a_-^\dagger(\Omega)\right], \tag{2.6}$$

whose only nonzero commutators are

$$[a_1(\Omega), a_2^\dagger(\Omega)] = -[a_2(\Omega), a_1^\dagger(\Omega)] = 2\pi\mathrm{i}\,\delta(\Omega - \Omega'). \tag{2.7}$$

We can now expand the field (2.5) in terms of the quadrature operators

$$E_k(t) = \sqrt{\frac{4\pi\hbar\omega_0}{\mathcal{A}c}} \int_0^\infty \frac{\mathrm{d}\Omega}{2\pi} \left[a_k(\Omega)\, \mathrm{e}^{-\mathrm{i}\Omega t} + a_k^\dagger(\Omega)\, \mathrm{e}^{\mathrm{i}\Omega t}\right], \tag{2.8}$$

for which the full electromagnetic field becomes

$$E(t) = E_1(t)\cos\omega_0 t + E_2(t)\sin\omega_0 t. \tag{2.9}$$

Eq. (2.9) describes the state of a general field of frequency ω_0 with signals oscillating at frequencies of order $\Omega \ll \omega_0$. However, we will often be interested in the case where these signals are oscillating on top of a strong signal of amplitude E_0—the carrier. By convention the carrier is usually put in the cosine quadrature. In this case the field is

$$E(t) = [E_0 + E_1(t)]\cos\omega_0 t + E_2(t)\sin\omega_0 t. \tag{2.10}$$

For this reason, the cosine quadrature is also often referred to as the amplitude quadrature and the sine quadrature is often referred to as the phase quadrature.

2.1.2 Coherent States and Squeezed States

We now briefly review the quantum noise in commonly used quantum states of the electromagnetic field. The one-sided noise spectral density in the state $|\psi\rangle$ is defined as [23–25]

$$\left\langle \psi \middle| a_i(\Omega) a_i^\dagger(\Omega') \middle| \psi \right\rangle_{\text{sym}} = \frac{1}{2} 2\pi\delta(\Omega - \Omega') S_{a_i}, \tag{2.11}$$

where

$$\langle AB \rangle_{\text{sym}} = \frac{1}{2}\langle AB + BA \rangle. \tag{2.12}$$

Let $|0_a\rangle$ be the vacuum of the a modes, i.e.

$$a_+(\Omega)|0_a\rangle = a_-(\Omega)|0_a\rangle = 0. \tag{2.13}$$

From (2.6) and (2.7)

$$\left\langle 0_a \middle| a_i(\Omega) a_j^\dagger(\Omega') \middle| 0_a \right\rangle = \frac{1}{2} 2\pi\delta(\Omega - \Omega')\delta_{ij}. \tag{2.14}$$

The noise in the vacuum is, therefore,

$$S_{a_1} = S_{a_2} = 1, \qquad S_{a_1 a_2} = 0. \tag{2.15}$$

This is the minimum noise allowed by the Heisenberg uncertainty relations. A state for which $S_{a_1} S_{a_2} = 1$ is called a minimum uncertainty state. The a vacuum $|0_a\rangle$ is also called the unsqueezed vacuum or the coherent vacuum. It is useful to visualize quantum states by plotting ellipses that represent the shape of the quantum noise. Fig. 2.1 shows several examples. The horizontal axis represents the noise in the a_1, or amplitude, quadrature and the vertical axis represents the noise in the a_2, or phase, quadrature. The unsqueezed vacuum is represented by a circle at the origin with radius $S_{a_1} = S_{a_2} = 1$.

A coherent state is a non-zero minimum uncertainty state. It is obtained by using the one photon displacement operators

$$D(\alpha, a) = \mathrm{e}^{\alpha a^\dagger - \alpha^* a} \tag{2.16}$$

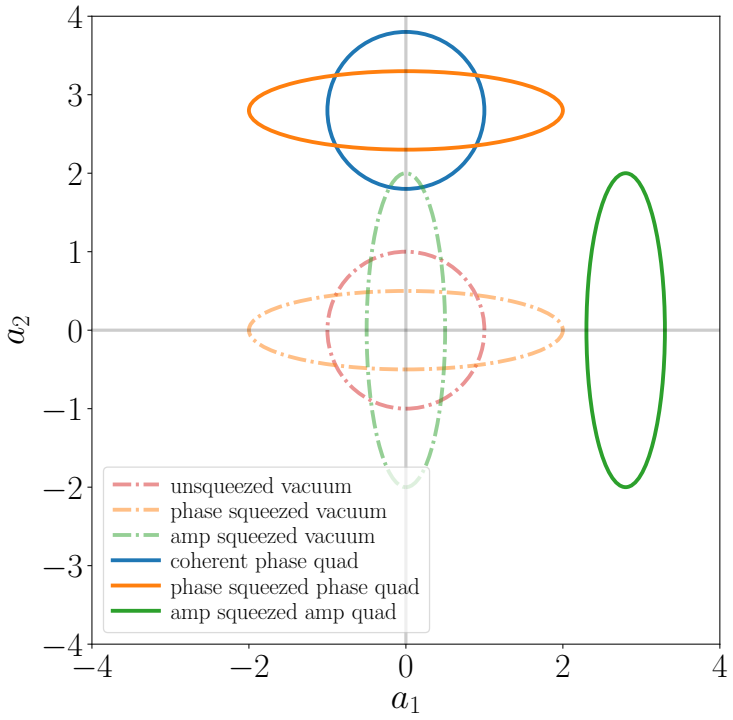

Figure 2.1: Quantum noise ellipses

to displace the vacuum state:

$$|\alpha_+, \alpha_-\rangle = D(\alpha_+, a_+)D(\alpha_-, a_-)|0_a\rangle = \mathrm{e}^{\alpha_+ a_+^\dagger - \alpha_+^* a_+}\mathrm{e}^{\alpha_- a_-^\dagger - \alpha_-^* a_-}|0_a\rangle \tag{2.17}$$

and has non-zero expectation value for the one-photon annihilation operators

$$\langle \alpha_+, \alpha_-|a_\pm|\alpha_+, \alpha_-\rangle = \alpha_\pm. \tag{2.18}$$

See Refs. [23, 24] for details and expectation values for the quadrature operators $a_{1,2}$. Physically, a coherent state is a classical signal with the minimum amount of quantum noise. It is the state of an ideal laser, for example. The noise ellipse of a coherent state is again a circle of radius $S_a = 1$, but it is displaced from the origin by the strength of the signal; see Fig. 2.1. The direction of the displacement is the quadrature of the signal. If the displacement is along the a_2 axis, as it is in Fig. 2.1, it is a phase signal; if it is along the a_1 axis it is an amplitude signal. The displacement can be in any direction in which

case it is a mixture of the two quadratures.

The uncertainty relations say only that the product of the noise in both quadratures is no less than one. Squeezed states are also minimum-uncertainty states but have the noise in one quadrature less than one at the expense of the noise in the other quadrature being greater than one. The squeezed vacuum state is made by acting on the unsqueezed vacuum with

$$S(r,\phi) = \exp\left[r\left(a_+ a_- \mathrm{e}^{-2\mathrm{i}\phi} - a_+^\dagger a_-^\dagger \mathrm{e}^{2\mathrm{i}\phi}\right)\right]. \tag{2.19}$$

The state $S(r,\phi)|0_a\rangle$ has noise e^{-2r} in the ϕ quadrature and e^{2r} in the $\phi+\pi/2$ quadrature. Again see Refs. [23, 24] for details. If $\phi = 0$ so that the uncertainty is reduced in the amplitude quadrature, the state is an amplitude squeezed state, and if $\phi = \pi/2$ so that the uncertainty is reduced in the phase quadrature, the state is a phase squeezed state. The noise of a squeezed state is plotted as an ellipse with semi-minor axis e^{-2r} and semi-major axis e^{2r} with the axis oriented along the direction of squeezing. Squeezed vacuum states can also be displaced. These are signals with reduced uncertainty in one quadrature. Fig. 2.1 shows several examples.

2.2 Optomechanical Interactions

2.2.1 Ponderomotive Squeezing

This thesis is concerned with the generation of squeezing through the optomechanical interaction between a laser and a movable mirror [18, 27, 28]. Intuitively what happens is the following. Suppose we send light towards a movable mirror where it is reflected and returns to the starting point where the phase is measured. Since the light exerts radiation pressure on the mirror, any fluctuations in the amplitude of this force results in fluctuations in the position of the mirror. But the phase of the light also changes when the

mirror moves since the distance it has to travel also fluctuates. Therefore, this radiation pressure induced optomechanical interaction converts amplitude fluctuations into phase fluctuations thus correlating the two quadratures and producing a squeezed state. This optomechanical generation of squeezing is known as ponderomotive squeezing. The rest of this section describes this process quantitatively.

Suppose we send the field $E_a(t)$ towards the mirror a distance L from the starting point and measure the field $E_b(t)$ that returns. The two fields are related by $E_b(t) = E_a(t - 2L/c)$. Let E_a have the form (2.10):

$$E_a(t) = [E_0 + E_{1a}(t)] \cos \omega_0 t + E_{2a}(t) \sin \omega_0 t, \tag{2.20}$$

where E_0 is the amplitude of the carrier, and similarly for E_b. This notation signifies that E_a is expanded as (2.8) with quadrature operators a_1 and a_2, and E_b is expanded as (2.8) with quadrature operators b_1 and b_2. If the position of the mirror is $L + x(t)$, the relation between E_a and E_b is, for small x/L, and $\dot{x}/c$,

$$E_b(t) = [E_0 + E_{1a}(t - 2L/c)] \cos \omega_0 t + \left[E_{2a}(t - 2L/c) + \frac{2\omega_0 E_0}{c} x(t - L/c) \right] \sin(\omega_0 t) \tag{2.21a}$$

$$= E_0 \left[1 + \frac{E_{1a}(t - 2L/c)}{E_0} \right] \cos \left[\omega_0 t - \frac{2\omega_0 E_0}{c} x(t - L/c) \right]. \tag{2.21b}$$

Indeed, the vacuum fluctuations a_1 are responsible for amplitude fluctuations and the vacuum fluctuations a_2 are responsible for phase fluctuations. In the frequency domain, (2.21) is

$$E_{1b}(\Omega) = \mathrm{e}^{2\mathrm{i}\beta} E_{1a}(\Omega) \tag{2.22a}$$

$$E_{2b}(\Omega) = \mathrm{e}^{2\mathrm{i}\beta} E_{2a} + \mathrm{e}^{\mathrm{i}\beta} \frac{2\omega_0 E_0}{c} x(\Omega), \tag{2.22b}$$

where $\beta = \Omega L/c$ is the phase gained going one way.

Now we relate the mirror position x to the amplitude vacuum fluctuations E_{1a}. The radiation pressure induced force on the mirror is

$$F = \frac{2P}{c} = 2\frac{\mathcal{A}c}{8\pi}[E_0 + E_{1a}(t - L/c)]^2 = \frac{\mathcal{A}E_0^2}{4\pi} + \frac{\mathcal{A}E_0 E_{1a}(t - L/c)}{2\pi} \equiv F_0 + F_{\mathrm{BA}}. \quad (2.23)$$

The first term F_0 is the DC contribution to the radiation pressure force which would be canceled by a control system. In gravitational wave detectors, the mirrors are suspended from pendula which cancel this force at DC. Above the mechanical resonance frequency of the pendula (roughly 1 Hz in the case of these detectors) the mirrors behave as free masses like we are considering here. The second term F_{BA} is the back action force due to the amplitude vacuum fluctuations a_1. The equations of motion for a free mass in the presence of this radiation pressure force are

$$-M\Omega^2 x(\Omega) = \mathrm{e}^{\mathrm{i}\beta} F_{\mathrm{BA}}(\Omega) = \mathrm{e}^{\mathrm{i}\beta}\frac{\mathcal{A}E_0}{2\pi} E_{1a}(\Omega), \quad (2.24)$$

where M is the mass of the mirror.

Plugging this into (2.22) and using (2.8) to write it in terms of the quadrature operators, the input output relations for reflection from a mirror are

$$b_1 = \mathrm{e}^{2\mathrm{i}\beta} a_1 \quad (2.25a)$$

$$b_2 = \mathrm{e}^{2\mathrm{i}\beta}(a_2 - \mathcal{K}a_1), \quad (2.25b)$$

where

$$\mathcal{K} = \frac{8P\omega_0}{M\Omega^2 c^2} \quad (2.26)$$

is the strength of the optomechanical coupling and P is the power of the light. The noise spectral densities are

$$S_{b_1} = 1, \qquad S_{b_2} = 1 + \mathcal{K}^2, \qquad S_{b_1 b_2} = -\mathcal{K} \quad (2.27)$$

This is a squeezed state with $r = \mathrm{arcsinh}(\mathcal{K}/2)$. Even though this is a very simple system, it captures the fundamental physics of ponderomotive squeezing. The structure

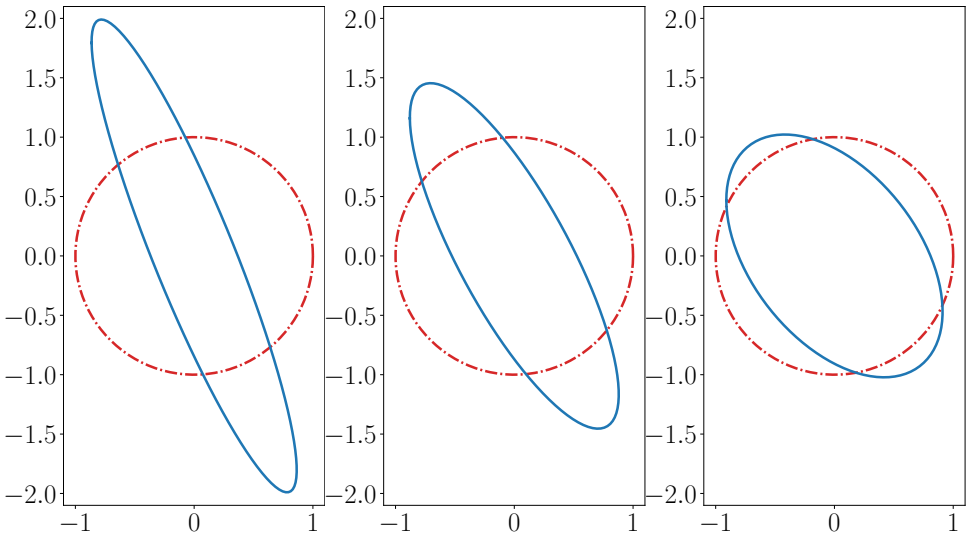

Figure 2.2: Quantum noise ellipses ponderomotively generated as a function of frequency. Frequency increases from left to right as the amount of squeezing is reduced.

of (2.25) and (2.27) is very general; it is mostly the optomechanical coupling $\mathcal{K}$ that changes for different systems. Eq. (2.25) says that amplitude fluctuations cause amplitude fluctuations and phase fluctuations cause phase fluctuations. But amplitude fluctuations also cause phase fluctuations with strength $\mathcal{K}$. Furthermore, the first term in (2.27) for the noise for the phase quadrature is the shot noise $S_{\text{shot}} = 1$, and the second term is the radiation pressure noise $S_{\text{RP}} = \mathcal{K}^2$. The origin of both comes from the vacuum fluctuations beating with the carrier: the beating of the phase fluctuations a_2 cause the shot noise and the beating of the amplitude fluctuations a_1 cause the radiation pressure noise.

Note that the optomechanical coupling from (2.26) is proportional to the power P and inversely proportional to the mass M and squared frequency Ω^2. This is also a general feature of ponderomotive squeezing in more complicated systems. The frequency dependence may be different but it will eventually decrease at higher frequencies. Note that this means the squeezing is frequency dependent and has a larger magnitude at lower frequencies. Fig. 2.2 shows the quantum noise ellipses for a ponderomotively squeezed

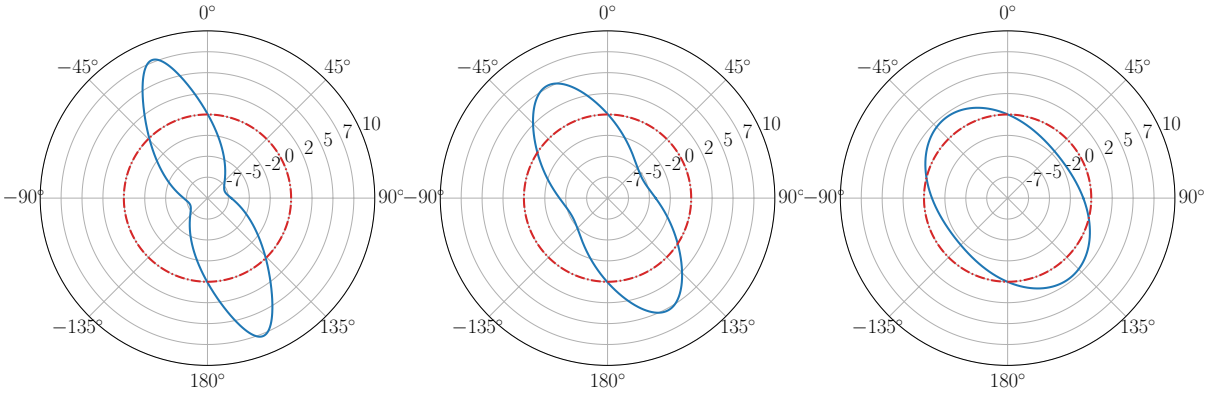

Figure 2.3: Quantum noise ellipses expressed as decibels relative to vacuum noise. The same ellipses are plotted here as are plotted in Fig. 2.2. The radial distance is measured in dBvac and the red dashed circle is the noise of the unsqueezed vacuum at 0 dBvac.

state for increasing frequency. Indeed, the magnitude of the squeezing decreases and the ellipse rotates counterclockwise as the frequency increases.

It is difficult to plot these ellipses when the magnitude of the squeezing becomes large. For this reason we also plot them in terms of decibels relative to unsqueezed vacuum noise (dBvac), i.e. $10\log_{10}(S_b/S_a)$. Fig. 2.3 shows these noise ellipses for the same noise ellipses plotted in Fig. 2.2. The radial direction is measured in dBvac. The red dashed circle is the unsqueezed vacuum ellipse and is at 0 dBvac. We will use these plots exclusively in Chap. 3 since the magnitude of squeezing can be as much as 50 dBvac.

The input output relations for a Michelson interferometer with Fabry-Perot cavities as arms (FPMI) also has the form (2.25). In fact, the response to differential arm motion of such an interferometer is equivalent to that of a single Fabry-Perot cavity.[2] We will discuss this in detail in Chap. 3 where we also include the signal recycling mirror. In that case, the interferometer acts like a three mirror cavity; see Fig. 3.2. For now we stick with the FPMI, or PRFPMI, which is equivalent to a single Fabry-Perot cavity.

[2]The same is true for a power recycled Fabry-Perot Michelson interferometer (PRFPMI). For the purposes of differential arm motion, the only difference is the relationship between the amount of power incident on the interferometer and the amount of power in the arms.

The input output relations are [25]

$$\begin{bmatrix} b_1 \\ b_2 \end{bmatrix} = \mathrm{e}^{2\mathrm{i}\beta} \begin{bmatrix} 1 & 0 \\ -\mathcal{K} & 1 \end{bmatrix} \begin{bmatrix} a_1 \\ a_2 \end{bmatrix} + \frac{\sqrt{2\mathcal{K}}}{h_{\mathrm{SQL}} L} \begin{bmatrix} 0 \\ 1 \end{bmatrix} \Delta L, \tag{2.28}$$

where L is the length of the arms, the strength of the optomechanical coupling is

$$\mathcal{K} = \frac{2P_{\mathrm{BS}}/P_{\mathrm{SQL}}}{(\Omega/\gamma)^2[1 + (\Omega/\gamma)^2]} \tag{2.29}$$

$\gamma = cT_i/4L$ is the cavity pole, $\beta = \arctan \Omega/\gamma$, P_{BS} is the power on the beam splitter, and

$$h_{\mathrm{SQL}} = \sqrt{\frac{8\hbar}{M\Omega^2 L^2}}, \qquad P_{\mathrm{SQL}} = \frac{ML^2\gamma^4}{4\omega_0}. \tag{2.30}$$

We will explore the behavior of Fabry-Perot cavities (and thus interferometers) in detail in Chap. 3, but for now notice the form of the optomechanical coupling (2.29). As with the free mass $\mathcal{K}$, it is proportional to the power P_{BS} and inversely proportional to the mass M. For $\Omega < \gamma$, the coupling also has the behavior of the free mass coupling falling like Ω^{-2}; for $\Omega > \gamma$, it falls faster like Ω^{-4}.

2.2.2 Optical Spring

When a Fabry-Perot cavity is detuned from resonance, the radiation pressure force produces a spring-like coupling between the two mirrors known as an optical spring [27–29]. Fig. 2.4 shows a Fabry-Perot cavity with one movable mirror suspended from a pendulum as well as the circulating power in the cavity as a function of mirror position. The force between the mirrors is due to the radiation pressure of the circulating power and is proportional to P_{circ}. When the cavity is held on resonance, the circulating power P_{circ} is maximized and there is no first order change in the power as the position of the mirror moves $\partial P_{\mathrm{circ}}/\partial x = 0$.

When the length of the cavity is made slightly longer, also known as blue-detuning, the circulating power is reduced. Now, if the mirror moves slightly to the right, the

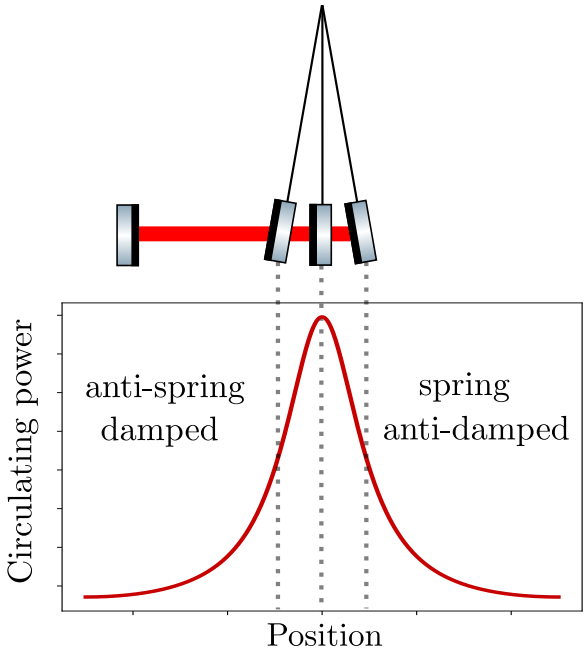

Figure 2.4: Optical spring

circulating power is reduced, which reduces the radiation pressure, which then forces the mirror back towards the left until the radiation pressure force balances the restoring force from the pendulum. Similarly, if the mirror moves to the left the circulating power increases which pushes the mirror back to the right. The detuning has created an optical spring between the two mirrors with spring constant proportional to $-\partial P_{\text{circ}}/\partial x > 0$.

If the length of the cavity is made slightly shorter, also known as red-detuning, the circulating power is again reduced. Now, however the situation is the opposite as with the blue-detuned case. Motion to the right increases the circulating power and forces the mirror further to the right; motion to the left decreases the circulating power and forces the mirror further to the left. This detuning has created an optical anti-spring with spring constant proportional to $-\partial P_{\text{circ}}/\partial x < 0$.

Note that the force slightly lags the position of the mirror. This leads to the spring being anti-damped by this phase delay and the anti-spring being damped. Thus, optical

springs or anti-springs are always unstable: the spring is statically stable and dynamically unstable, but the anti-spring is statically unstable and dynamically stable. Thus any use of an optical spring in an experiment requires a control system to stabilize.[3]

2.3 The Effects of Classical Noise on Quantum States

Anytime there are losses, unsqueezed vacuum is added in quadrature with the signal thus degrading the squeezing. This can be thought of as circularizing the quantum noise ellipse; see Fig. 2.5. If a is the input signal before losses and b is the output signal after ϵ losses, the resulting state is

$$b = \sqrt{1-\epsilon}\, a + \sqrt{\epsilon}\, c \tag{2.31}$$

where c is unsqueezed vacuum. Since c is, by definition, uncorrelated with a and, since $S_c = 1$, the noise becomes

$$S_b = (1-\epsilon)S_a + \epsilon. \tag{2.32}$$

If a was squeezed so that $S_a < 1$, the unsqueezed vacuum has degraded the squeezing. In gravitational wave detectors, and elsewhere, much effort may be made to squeeze the light so that a small signal can be detected. The presence of classical noise seriously limits the benefit of such efforts. Even if the signal is not appreciably reduced by losses or noise, the quantum noise can become significantly worse as is shown in Fig. 2.5.

An interferometric gravitational wave detector can have significant squeezing inside the interferometer, but then encounter losses in the readout chain between the interferometer and the photodetectors. To ameliorate these effects, one can consider amplifying the signal and the noise before encountering losses that could reduce the signal below detectable levels, and this should be done as soon as possible after the signal exits the

[3] Ref. [30] suggests a scheme where two optical springs can be combined to produce a stable composite system.

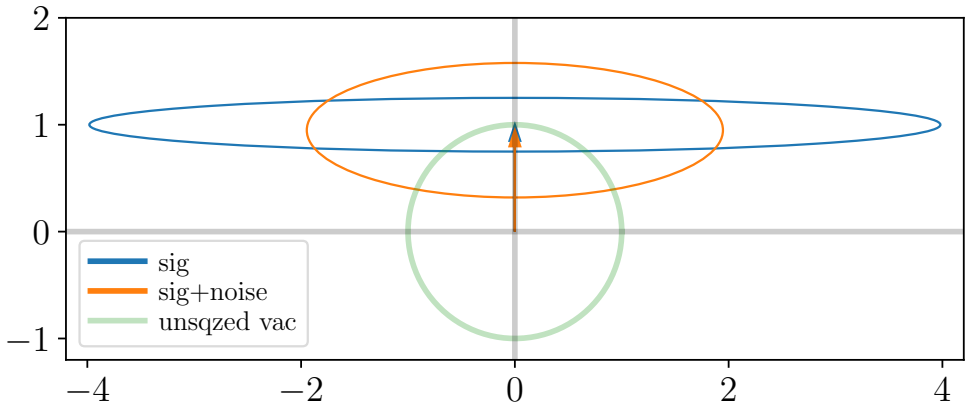

Figure 2.5: Degradation of a squeezed state by classical noise. A signal with 12 dB phase squeezing in the phase quadrature encounters 10% losses, which mixes in 10% unqueezed vacuum. The arrows denote the signal.

interferometer. This is similar to the idea of a classical amplifier where both the signal and noise are amplified but the signal to noise ratio stays the same, if it is an ideal amplifier. In reality the amplifier will add some noise itself.

When dealing with very weak signals near the quantum limit, however, a more careful analysis is required. Furthermore, we want the output signal to be in a highly quantum squeezed state with reduced uncertainty in the signal quadrature. In addition to degrading the signal itself, any noise added to such a state decreases the squeezing and thus also decreases the SNR. So the amplification is extra important here.

To prevent the amplifier itself from adding extra quantum noise to the signal, a phase insensitive amplifier which amplifies all quadratures equally cannot be used, however. Such phase insensitive amplifiers must add at least half a quantum of vacuum noise to the signal [31–34]. This can be understood physically by noting that some other mode must be present to provide the energy for the amplification. It is the quantum noise from this mode that is added to the signal. This additional quantum noise can be avoided, however, if a phase sensitive amplifier is used which amplifies the quadratures differently. If the signal quadrature is amplified by a factor of e^r then the orthogonal quadrature is

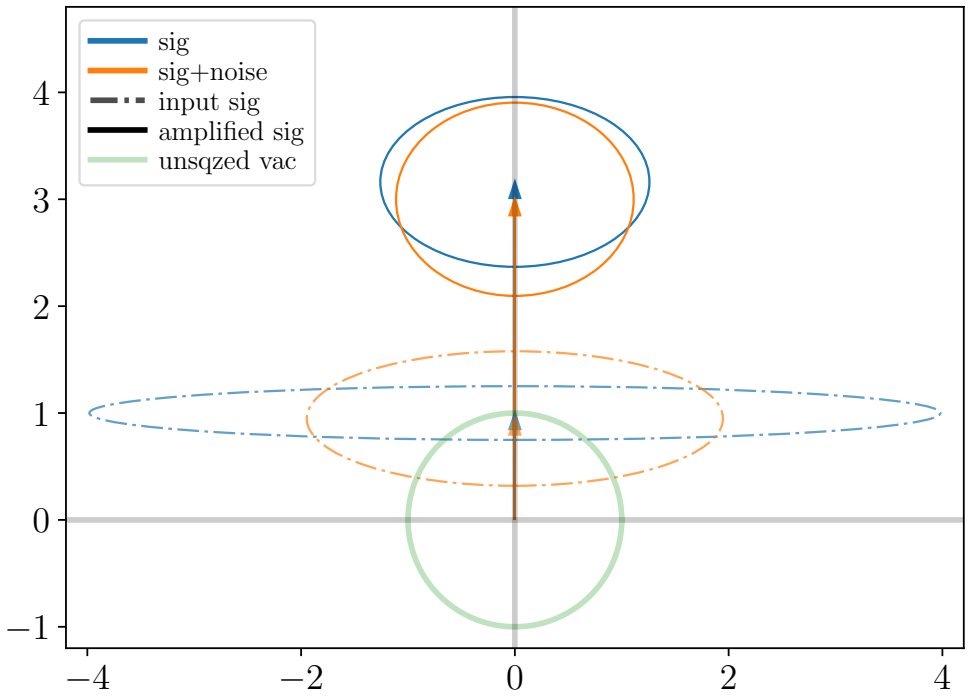

Figure 2.6: Amplification of a squeezed state before degradation by classical noise. The same original 12 dB squeezed state from Fig. 2.5 is shown as the blue dashed ellipse. The orange dashed ellipse is the noise that would be found with no amplification. The blue solid ellipse is the input state amplified by 10 dB, and the state after 10% losses is shown as the solid orange ellipse.

reduced by the same amount. Thus, if the signal is in the a_2 quadrature, the amplifier should output the state

$$b_1 = \mathrm{e}^{-r} a_1, \qquad b_2 = \mathrm{e}^{r} a_2. \tag{2.33}$$

Such a phase sensitive amplification scheme is shown in Fig. 2.6.

It is possible to make such phase sensitive amplifiers out of optomechanical systems using ponderomotive squeezing. Such amplifiers are known as phase-sensitive optomechanical amplifiers (PSOMAs). The general amplifier scheme as used in interferometers is shown in Fig. 2.7. The input and output from the main interferometer are the fields a_{IFO} and b_{IFO}, respectively. These signals are sent through an amplifier which has its own input and output fields α and β. (The amplifier fields α and β would be responsible for the extra quantum noise if the amplifier was phase insensitive.) The full input and output from the detector are the fields a and b. So the output from the interferometer b_{IFO} is amplified to the detected signal b and input vacuum a enters the interferometer as a_{IFO}.

Such PSOMAs will have the general form (2.25). The signal to be amplified should be put in the amplitude quadrature. The general interaction (2.25) will than amplify the signal into the phase quadrature. Explicitly, suppose the signal exits the interferometer in the amplitude quadrature $b_{\mathrm{IFO},1}$. The amplifier should then amplify the signal like

$$\begin{bmatrix} b_1 \\ b_2 \end{bmatrix} = \begin{bmatrix} 1 & 0 \\ -\mathcal{K} & 1 \end{bmatrix} \begin{bmatrix} b_{\mathrm{IFO},1} \\ b_{\mathrm{IFO},2} \end{bmatrix} \tag{2.34}$$

The signal that exits the interferometer as $b_{\mathrm{IFO},1}$ gets amplified by $\mathcal{K}$ and should be measured in the output phase quadrature b_2.

The form of $\mathcal{K}$ will be determined by the details of the amplifier. The amplifier field α is responsible for the amplification and one of the α quadratures will have the strong carrier, or pump. Note that the quadrature is defined by where the carrier or pump is. So

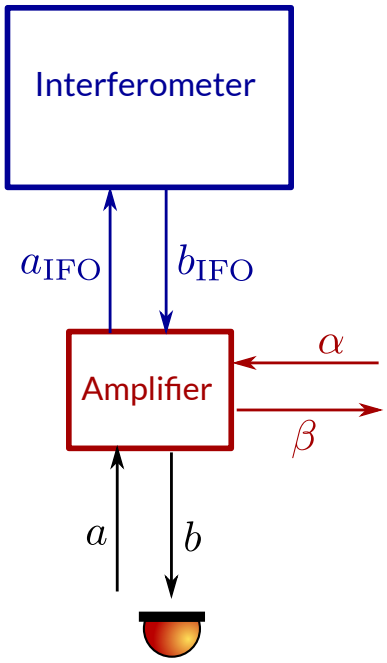

Figure 2.7: General scheme for phase sensitive optomechanical amplifier

even if a signal is in the phase quadrature when it exits the interferometer $b_{\mathrm{IFO},2}$ it can be in the amplitude quadrature with respect to the amplifier by making the amplifier pump field α_2 instead of α_1. The important thing is that the signal that exits the interferometer be in the same quadrature as the amplifier pump. Whichever quadrature that is gets amplified by the optomechanical interaction into the other quadrature where it should be measured.

One way of realizing such an optomechanical amplifier in practice is with another interferometer, as is illustrated in Fig. 2.8. The details of this kind of interferometer are given by (2.28). A Faraday isolator serves as an optical circulator and is used to send the signal from the main interferometer b_{IFO} into the dark port of the amplifier interferometer. The amplified signal b exits the dark port and is detected. The noise entering the full detector a is routed through the Faraday into the main interferometer and bypasses the amplifying interferometer. That the vacuum entering the main interferometer bypasses

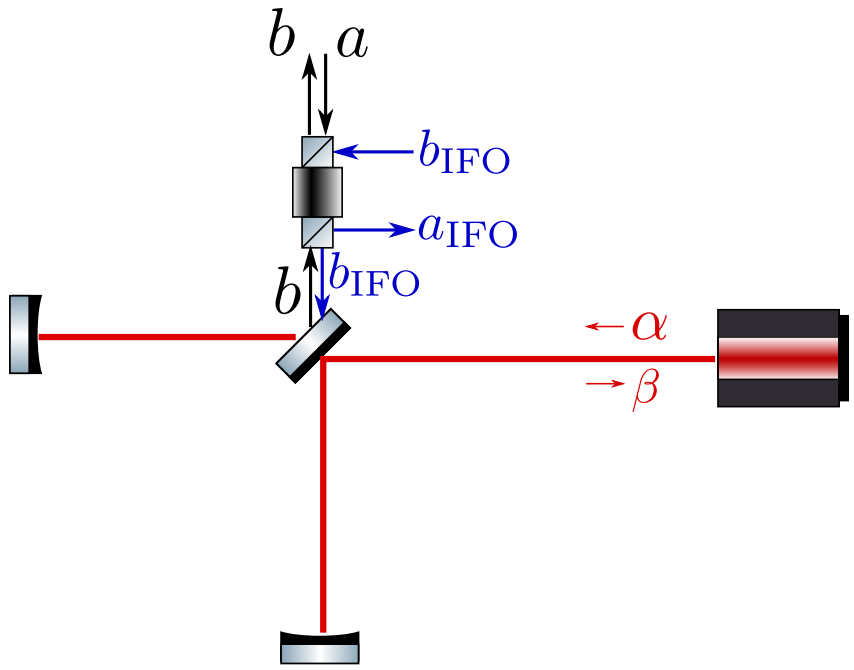

Figure 2.8: Using an interferometer as a phase sensitive optomechanical amplifier. The Faraday isolator acts as an optical circulator.

the amplifier is important so that the amplifier doesn't make the quantum noise of the main interferometer itself worse. In this case, the amplifier pump field α is the laser of the amplifier interferometer.

Another way of realizing such an optomechanical amplifier is to use a ring cavity, as is illustrated in Fig. 2.9. A strong pump field is sent into the ring and travels in the same direction as the signal field b_{IFO} exiting from the interferometer. This amplifies the output signal b which is detected. The noise a entering the detector travels in the opposite direction around the ring and so the noise a_{IFO} entering the interferometer is not amplified. The ring thus acts as an amplifer and a circulator. There are also two sets of modes that couple into the amplifier in this case denoted by $\alpha, \beta, \tilde{\alpha}$, and $\tilde{\beta}$. If the input noise a is squeezed then the noise $\tilde{\alpha}$ coupled in through the amplifier will degrade the resulting squeezing a_{IFO} entering the dark port of the interferometer.

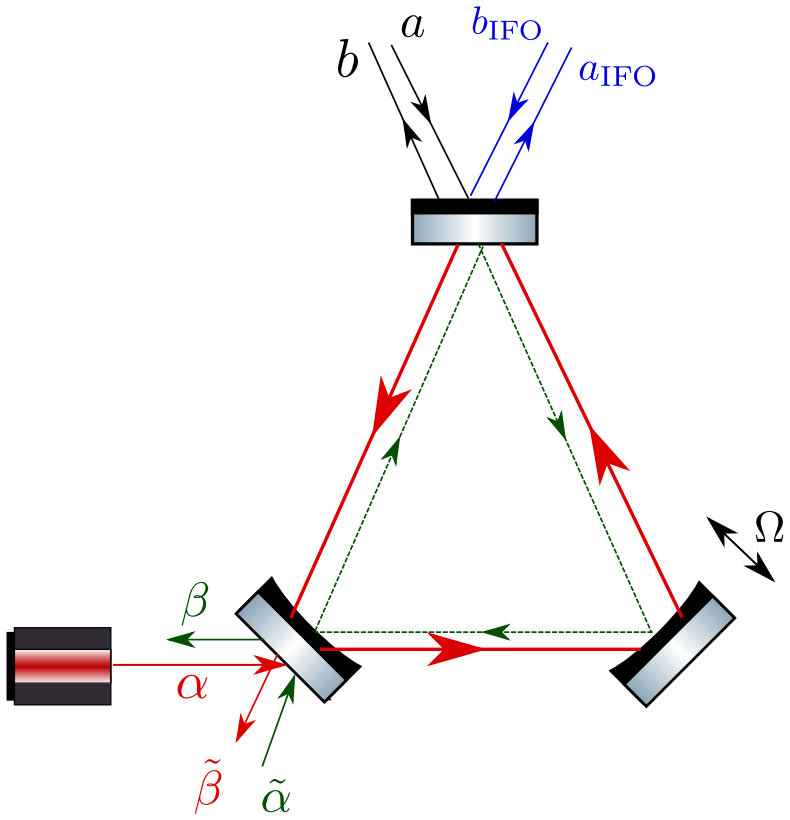

Figure 2.9: Using a ring cavity as a phase sensitive optomechanical amplifier. The one-way direction of the pump makes turns the ring cavity into an optical ciculator.

Chapter 3

Towards the Observation of Ponderomotive Squeezing in a 40 m Interferometer

In this chapter we discuss the possibility of observing ponderomotive squeezing at the Caltech 40 m interferometer. The goal is to measure the output vacuum noise at the asymmetric port of the interferometer and observe it squeezed, through the ponderomotive interactions of the interferometer, below the level of vacuum fluctuations entering the interferometer in some quadratures. Sec. 3.1 describes the optomechanical response of the interferometer. Sec. 3.2 describes the propagation of quantum noise throughout the interferometer and the optimization of the interferometer to maximize the observable squeezing. In Sec. 3.3, we add classical noise to get an understanding of what the fundamental limits to the observable squeezing are, and in Sec. 3.4 we discuss further technical challenges that must be overcome. Finally, in Sec. 3.5 we discuss the prospects of observing squeezing below vacuum with different upgrades to the current state of the interferometer.

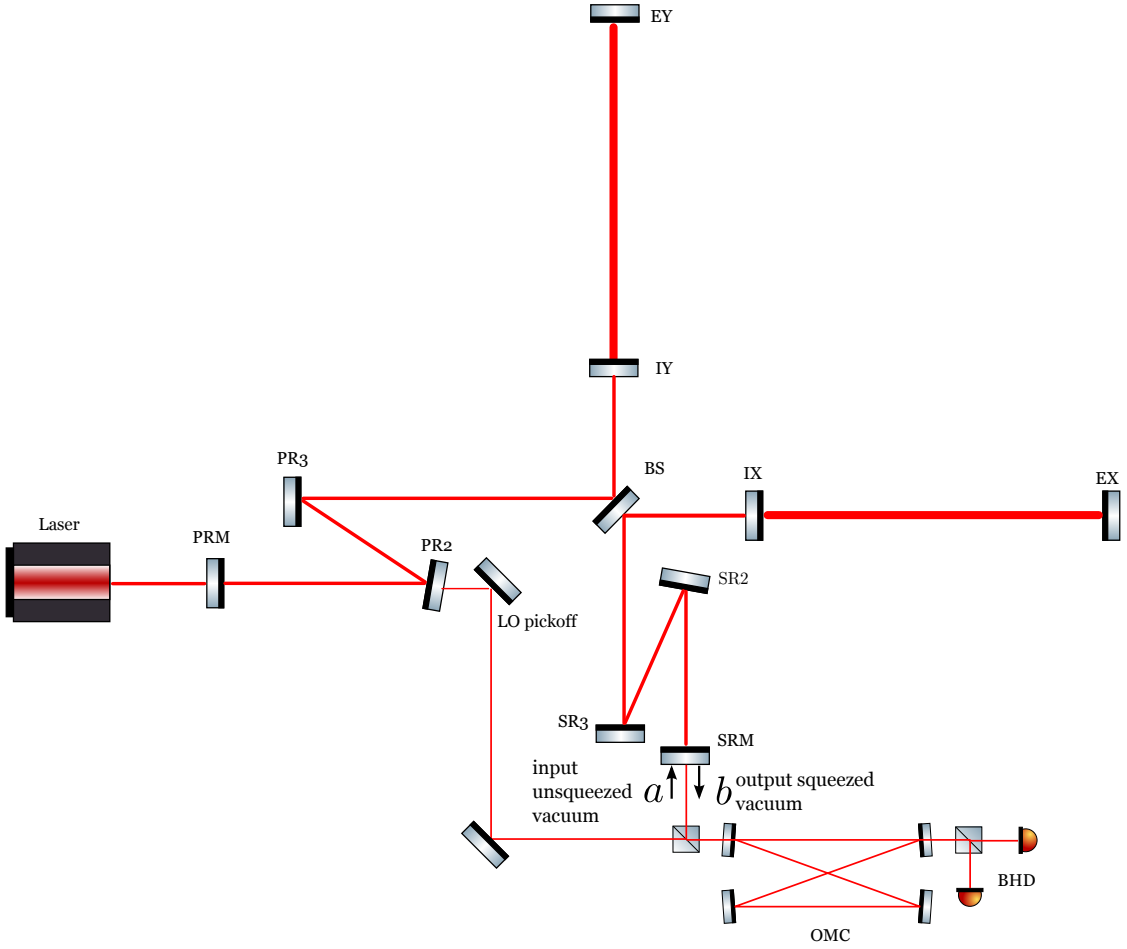

Figure 3.1: Schematic of a dual-recycled Fabry-Perot Michelson interferometer. In reality, the vacuum noises a and b enter and exit at the detector (labeled BHD); however, all calculations are done with them entering and exiting the interferometer as shown here. For our purposes, the only difference is losses going through the readout train to the photodiode, and these losses are included in the calculations.

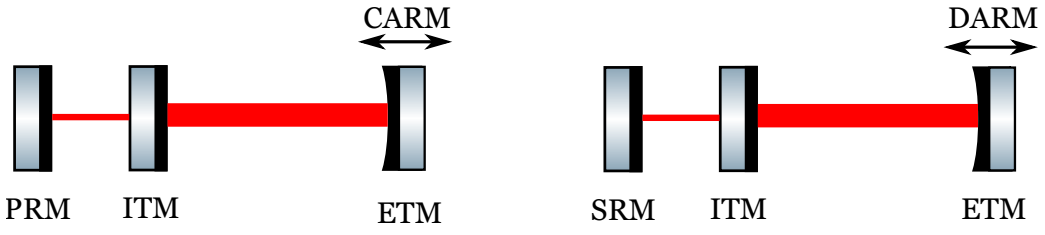

Figure 3.2: The CARM and DARM degrees of freedom are equivalent to two independent three mirror cavities. The CARM cavity is formed by the PRM, ITMs, and ETMs, and the DARM cavity is formed by the SRM, ITMs, and ETMs.

3.1 Optomechanical Response of a DRFPMI

The 40 m interferometer is a dual-recycled Fabry-Perot Michelson interferometer (DRFPMI), as is LIGO. Fig. 3.1 shows a schematic of a DRFPMI. Fabry-Perot Michelson means that, rather than being a simple Michelson with a beam splitter and two end mirrors, the interferometer has Fabry-Perot optical cavities for arms. Each cavity has an input test mass (ITM) and end test mass (ETM). Dual-recycled means that it employs both power and signal recycling: a power recycling mirror (PRM) forms a power recycling cavity (PRC) and a signal recycling mirror (SRM) forms a signal recycling cavity (SRC).

The optomechanical response of a DRFPMI can be reduced to that of coupled three mirror cavities: the differential arm length changes and common arm length changes each behave as independent coupled cavities. In both cases, the ETMs and ITMs form effective mirrors and the recycling mirror is the third; see Fig. 3.2. If L_x and L_y are the lengths of the X and Y arms, respectively, the common arm length (CARM) is defined as $L_+ = (L_x + L_y)/2$ and the differential arm length (DARM) is defined as $\Delta L = L_x - L_y$.[1]

The reflectivity of one of the simple Fabry-Perot cavities making one of the arms of the interferometer is[2]

$$r_{\mathrm{arm}} = \frac{-r_i + r_e \mathrm{e}^{-2\mathrm{i}\phi_{\mathrm{arm}}}}{1 - r_i r_e \mathrm{e}^{-2\mathrm{i}\phi_{\mathrm{arm}}}} \tag{3.1}$$

where $\phi_{\mathrm{arm}} = \omega L/c$ is the phase the light accrues traveling one-way in the cavity, r_i is the ITM mirror reflectivity, r_e is the ETM mirror reflectivity, and we have neglected losses in the mirrors. If a third mirror is added, any two look like an effective mirror to the third. In an interferometer, the arm cavities are always held on resonance $\phi_{\mathrm{arm}} = 0$. Furthermore, the end mirrors are almost perfectly reflecting $r_e \approx 1$, so the effective mirror

[1] This definition of CARM and DARM with differing factors of 2 is unfortunate but seems to be standard when actually plotting data, so we begrudgingly use it for calculations here. Note that some references use symmetric factors of 2 in calculations, however.

[2] We use the convention that the reflection from the front of a mirror is positive and the reflection from the back of a mirror is negative.

formed by the ETMs and ITMs is $r_{\rm arm} \approx 1$.

Now consider the compound mirror formed by one of the recycling mirrors and the ITM of one of the effective DARM or CARM cavities. The reflectivity of this mirror is

$$r_{\rm rec} = \frac{r_i + r_r e^{-2i\phi_{\rm rec}}}{1 + r_i r_r e^{-2i\phi_{\rm rec}}} \tag{3.2}$$

where $\phi_{\rm rec}$ is the phase the light accrues traveling one way in the recycling cavity. There are three possible tunings for this recycling cavity that lead to qualitatively different behavior for the full coupled three mirror cavity.

First, $\phi_{\rm rec} = 0$ gives the reflectivity $r_{\rm rec} = (r_i + r_r)/(1 + r_i r_r)$, which is greater than the reflectivity r_i of the single ITM. The coupled cavity therefore has a higher finesse, stores more power, and has a lower bandwidth than the original cavity. This is the tuning always used for the power recycling cavity for two reasons. First, we always want more power in the arms since, everything else being equal, this increases the response to gravitational waves and reduces the shot noise. Second, optical cavities act as low pass filters and attenuate signals outside of their bandwidth. The power recycling cavity passively filters laser noise outside of its bandwidth and, since this tuning lowers the bandwidth, this noise is filtered more aggressively. If this tuning is used for the signal recycling cavity it is called signal recycling (SR). With signal recycling, the interferometer is more sensitive to low frequency signals at the expense of losing sensitivity at higher frequencies. This tuning for the SRC is not used for gravitational wave detectors.

Second, the tuning $\phi_{\rm rec} = \pi/2$ gives the reflectivity $r_{\rm rec} = (r_i - r_r)/(1 - r_i r_r)$, which is less than the reflectivity of the single ITM. The coupled cavity therefore has a lower finesse, stores less power, and has a higher bandwidth than the original cavity. This is the tuning commonly used for gravitational wave detectors and is known as resonant sideband extraction (RSE).[3] One of the main motivations for having an SRC is to store

[3]It is called *resonant* sideband extraction because, with $\phi_{\rm rec} = \pi/2$, the carrier is resonant in the

more power in the arms while minimizing thermal loads on the optics. One way to store more power in the arms is to increase the power into the arms, either by getting a bigger laser or by increasing the power recycling gain, but this requires more power to be dissipated in the beam splitter and ITMs. Another way of storing more power is to increase the ITM mirror reflectivity, but this reduces the bandwidth of the detector. So the power can be increased by increasing the ITM reflectivity and then the bandwidth of the detector increased by adding an SRM and tuning it so that $\phi_{\mathrm{rec}} = \pi/2$.

Finally, the recycling cavity can be detuned, meaning ϕ_{rec} is any angle other than 0 or $\pi/2$. This leads to a more complicated response, which we discuss in detail now, and which we will exploit to observe ponderomotive squeezing below vacuum. The input output relations for a DRFPMI are[4] [29, 35]

$$\begin{bmatrix} b_1 \\ b_2 \end{bmatrix} = \begin{bmatrix} C_{11} & C_{12} \\ C_{21} & C_{22} \end{bmatrix} \begin{bmatrix} a_1 \\ a_2 \end{bmatrix} + \begin{bmatrix} D_1 \\ D_2 \end{bmatrix} \Delta L, \tag{3.3}$$

where $a_{1,2}$ are the input and $b_{1,2}$ are the output vacuum fields at the asymmetric port. The expressions for the matrices C and D in the presence of losses are also given in Refs. [29, 35], but they are complicated and unilluminating so we do not write them here; however, all calculations done in this chapter are done with losses included.

Rather than writing the matrices C and D in (3.3) in the parametrization of Refs. [29, 35], we use the parametrization of Ref. [36]. Any linear combination of the output quadratures b_1 and b_2 can be readout. The quadrature measured is

$$b_\zeta = b_1 \sin\zeta + b_2 \cos\zeta, \tag{3.4}$$

where ζ is known as the homodyne angle. One method, and the method planned for

recycling cavity if the arm is not resonant, i.e. if the ETM is removed so that it is just the recycling mirror and ITM. When the arm is brought into resonance the sign of the effective ITM reflectivity changes and so the carrier becomes non-resonant.

[4]Some multiplicitive constants have been absorbed into the definitions of the matrices C and D from their definitions in Refs. [29, 35].

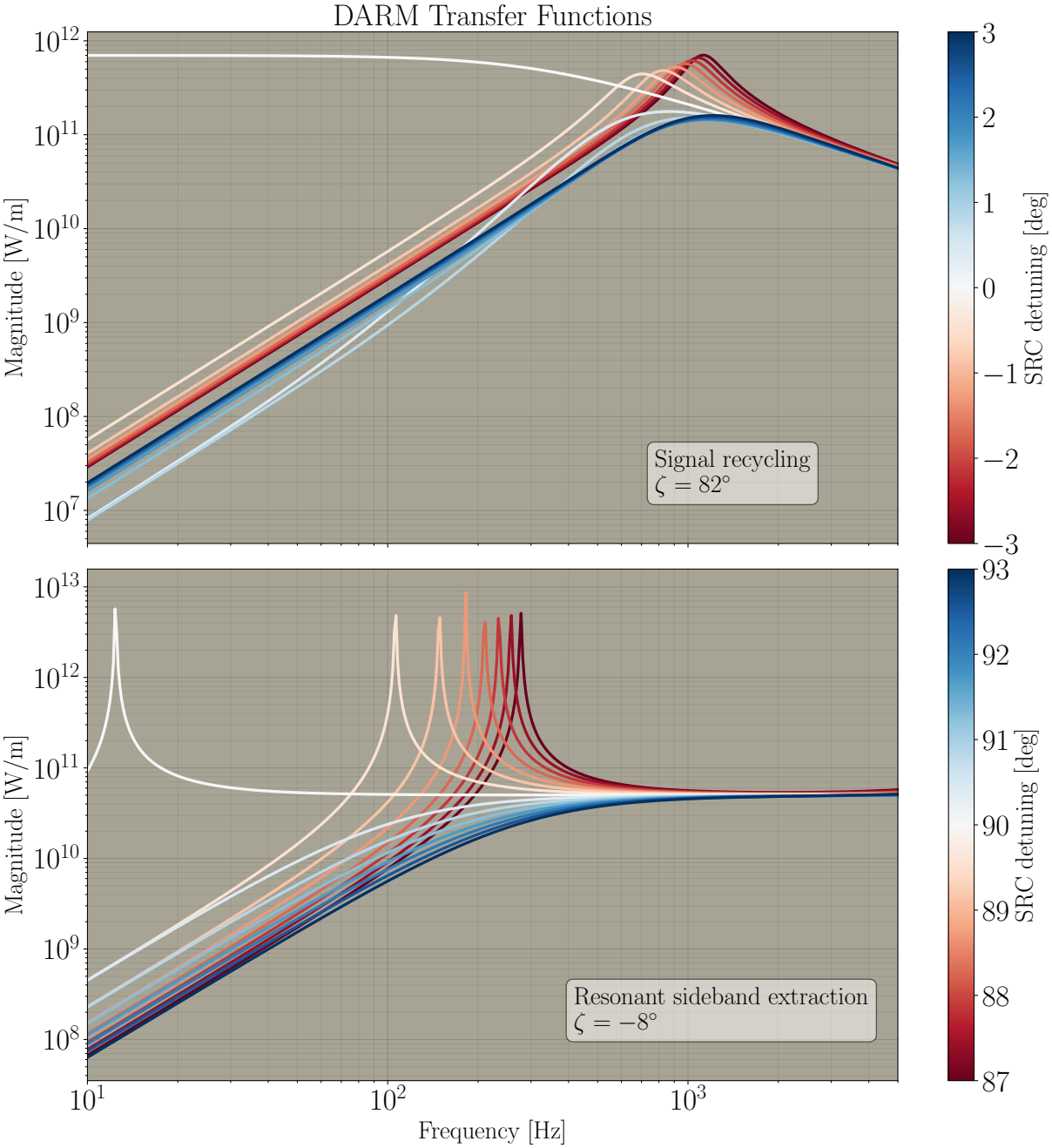

Figure 3.3: DARM transfer functions for typical 40 m parameters given in Tab. 3.1. The magnitude is the power detected at the asymmetric port per differential arm length change $\Delta L = L_x - L_y$.

this experiment and some future GW detectors, of measuring this signal is described in Appendix. B and is known as homodyne readout. This angle is defined so that the phase quadrature, and thus the quadrature with a gravitational wave signal, is at $\zeta = 0$ and the amplitude quadrature is at $\zeta = \pi/2$. The response of this quadrature to differential arm motion is[5]

$$b_\zeta = g_0 \frac{\cos(\phi+\zeta) - r_s\cos(\phi-\zeta)}{1 - 2r_s\cos 2\phi + r_s^2} \frac{(1+\mathrm{i}f/z)\mathrm{e}^{-2\pi\mathrm{i}fL/c}}{1+\mathrm{i}f/(f_pQ_p) - (f/f_p)^2 - (\xi/f)^2}\Delta L \tag{3.5a}$$

$$\equiv g_{\Delta L}\, G\,(1+\mathrm{i}f/z)\,\mathrm{e}^{-2\pi\mathrm{i}fL/c}\,\Delta L \tag{3.5b}$$

$$\equiv H\,\Delta L, \tag{3.5c}$$

where H is known as the DARM transfer function and we have defined

$$G = \frac{1}{1+\mathrm{i}f/(f_pQ_p) - (f/f_p)^2 - (\xi/f)^2}, \tag{3.6}$$

and the optical gain

$$g_{\Delta L} = g_0\left[\cos(\phi+\zeta) - r_s\cos(\phi-\zeta)\right] g_{\mathrm{vac}}. \tag{3.7}$$

The gain in the response of the interferometer due to differential arm motions ΔL is increased from the gain due to quantum vacuum fluctuations entering the asymmetric port described below by the first factor in (3.7). The gain due to the vacuum fluctuations is

$$g_{\mathrm{vac}} = \frac{1}{1 - 2r_s\cos 2\phi + r_s^2}, \tag{3.8}$$

and the constant g_0 sets the scale of the overall gain of the interferometer.

The other parameters defined in (3.5) have the following interpretations. The frequency $f_a = cT_i/8\pi L$ is the cavity pole of *the arm cavities* and is the frequency at which the response of the interferometer would start to roll off if there was no signal recycling

[5]The operator b_ζ has units of $\sqrt{\text{photons/Hz}}$ and so the units of g_0 as written are $\sqrt{\text{photons/Hz}}$/m. However, this transfer function is also valid for the physical power measured at the asymmetric port. In this case the numerical value of g_0 changes and has units of W/m.

mirror. As discussed above, the presence of the SRM modifies the bandwidth of the effective DARM cavity formed by the coupled cavity consisting of the arms and the SRM. The complex coupled DARM pole is

$$p = f_a \frac{1 - r_s e^{2i\phi}}{1 + r_s e^{2i\phi}}, \tag{3.9}$$

which is often useful to write in terms of it's magnitude

$$f_p = |p| = f_a \sqrt{\frac{1 - 2r_s \cos 2\phi + r_s^2}{1 + 2r_s \cos 2\phi + r_s^2}} \tag{3.10}$$

and Q factor

$$Q_p = \frac{f_p}{2\,\mathrm{Re}\,p} = \frac{\sqrt{1 - 2r_s^2 \cos 4\phi + r_s^4}}{2(1 - r_s^2)}. \tag{3.11}$$

For SR tuning ($\phi = 0$), the coupled pole $f_p = f_a(1 - r_s)/(1 + r_s)$ is less then the arm pole and the bandwidth is reduced; for RSE tuning ($\phi = \pi/2$), $f_p = f_a(1 + r_s)/(1 - r_s)$ is greater than the arm pole and the bandwidth is increased, as described above.

When the SRC is detuned, the DARM cavity forms an optical spring with the squared spring frequency

$$\xi^2 = f_a^2 \left(\frac{c P_{\mathrm{bs}}}{2\pi^3 \lambda_0 f_a^4 M L^2} \right) \left(\frac{2 r_s \sin 2\phi}{1 - 2 r_s \cos 2\phi + r_s^2} \right). \tag{3.12}$$

The mechanical resonance of the mirror pendula is shifted from its free value ω_m^2 to ξ^2. If $\xi^2 > 0$ the interaction is that of a spring, and if $\xi^2 < 0$ it is an anti-spring. Note that $\xi^2 \propto \phi(P_{\mathrm{BS}}/ML^2)/(1-r_s)^2$ for detunings near SR, and that $\xi^2 \propto -\tilde{\phi}(P_{\mathrm{BS}}/ML^2)/(1+r_s)^2$ for detunings near RSE where $\phi = \pi/2 + \tilde{\phi}$. The mechanical resonance is thus shifted to higher frequencies with SR tuning than with RSE tuning.

Finally, the homodyne zero

$$z = f_a \frac{\cos(\phi + \zeta) - r_s \cos(\phi - \zeta)}{\cos(\phi + \zeta) + r_s \cos(\phi - \zeta)} \tag{3.13}$$

is a zero of the DARM transfer function.

Fig. 3.3 shows several DARM transfer functions H for different SRC tunings ϕ near signal recycling ($\phi = 0$) and resonant sideband extraction ($\phi = \pi/2$) for parameters characteristic of the 40 m interferometer. For $\phi \approx 0$, the spring frequency is greater than the coupled pole; for $\phi \approx \pi/2$ the spring frequency is less than the coupled pole and the resonance is clearly seen in the transfer functions.

3.2 Quantum Noise in a DRFPMI

In Sec. 3.1, we described the response of the interferometer to differential arm motion, and thus to gravitational waves. In this section we describe the response to vacuum fluctuations entering the asymmetric port. The input output relations are

$$\begin{bmatrix} b_1 \\ b_2 \end{bmatrix} = g_{\mathrm{vac}}\, G \left[1 + (f/f_a)^2\right] \begin{bmatrix} \bar{C}_{11} & \bar{C}_{12} \\ \bar{C}_{21} & \bar{C}_{22} \end{bmatrix} \begin{bmatrix} a_1 \\ a_2 \end{bmatrix}, \tag{3.14}$$

where [29, 35]

$$\bar{C}_{11} = \bar{C}_{22} = (1 + r_s^2)\left(\cos 2\phi + \frac{\mathcal{K}}{2}\sin 2\phi\right) - 2r_s \frac{1 - (f/f_a)^2}{1 + (f/f_a)^2} \tag{3.15a}$$

$$\bar{C}_{12} = -t_s^2(\sin 2\phi + \mathcal{K}\sin^2\phi) \tag{3.15b}$$

$$\bar{C}_{21} = t_s^2(\sin 2\phi - \mathcal{K}\cos^2\phi). \tag{3.15c}$$

The function

$$\mathcal{K} = \frac{cP_{\mathrm{bs}}}{\pi^3 \lambda_0 f_a^4 M L^2} \frac{1}{(f/f_a)^2[1 + (f/f_a)^2]} \tag{3.16}$$

quantifies the strength of the optomechanical coupling. Below the cavity pole f_a, it behaves as a free mass falling like f^{-2}. At frequencies above the cavity pole, the low pass filtering of the cavity causes the response to fall faster like f^{-4}.

When reading out the quadrature b_ζ defined in (3.4) the quantum noise is

$$S_{b_\zeta} = S_{b_1}\sin^2\zeta + S_{b_2}\cos^2\zeta + S_{b_1 b_2}\sin 2\zeta. \tag{3.17}$$

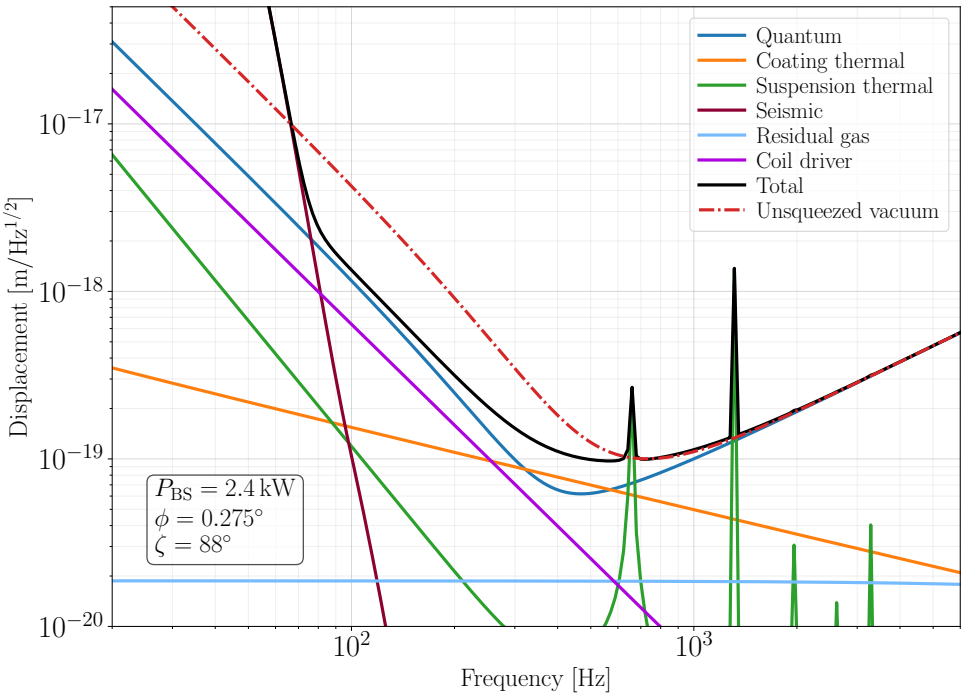

Figure 3.4: 40 m displacement noise budget. The dashed red trace is the noise of the unsqueezed vacuum, i.e. the vacuum noise measured if the output from the interferometer is blocked.

Quantity	Symbol	Value
Arm length	L	37.795 m
Mirror mass	M	264.2 g
Arm cavity pole	f_a	4.4 kHz
Arm finesse	$\mathcal{F}$	450
Input power	P_{in}	30 W
Power recycling gain	g_{prc}	80
Power on the beam splitter	P_{BS}	2.4 kW
Power in the arms	P_{arm}	344 kW
SRM power transmissivity	T_s	0.245
ITM power transmissivity	T_i	0.01384
ETM power transmissivity	T_e	13.7 ppm
Round trip losses in the arms	$\mathcal{L}$	20 ppm
Loss in the SRC	λ_{SR}	150 ppm
Downstream losses	λ_{PD}	0.05

Table 3.1: Optimistic 40 m parameters. Not all parameters are independent.

Since we only consider unsqueezed vacuum entering the interferometer, $S_{a_1} = S_{a_2} = 1$ and $S_{a_1 a_2} = 0$, so (3.17) becomes

$$S_{b_\zeta} = \left|g_{\mathrm{vac}}\, G\left[1 + (f/f_a)^2\right]\right|^2 \left[\bar{C}_{11}^2 - t_s^2 \mathcal{K} \bar{C}_{11} \sin 2\zeta \right. \\ \left. + \mathcal{K}^2(\cos^4\phi \cos^2\zeta + \sin^4\phi \sin^2\zeta) - 2\mathcal{K} \sin 2\phi \cos(\phi - \zeta)\cos(\phi + \zeta)\right]. \quad (3.18)$$

Now we take a detailed look at the quantum noise in the 40 m interferometer and ways to maximize the observable squeezing below vacuum. We will use the optimistic but plausible parameters given in Tab. 3.1 and briefly discuss other scenarios in Sec. 3.5.

When investigating squeezing below vacuum, there are two useful ways of plotting the relevant noises. The first is to directly plot the displacement noises on a standard noise budget, an example of which is shown in Fig. 3.4. It is important to note that these noises are *signal referred*. This means that the output from the interferometer is divided by the DARM transfer function H given by (3.5) so that the noises are what they would be if they were added directly to ΔL rather than to $H\Delta L$. In this noise budget, the red dashed trace labeled "Unsqueezed vacuum" is the (signal referred) unsqueezed

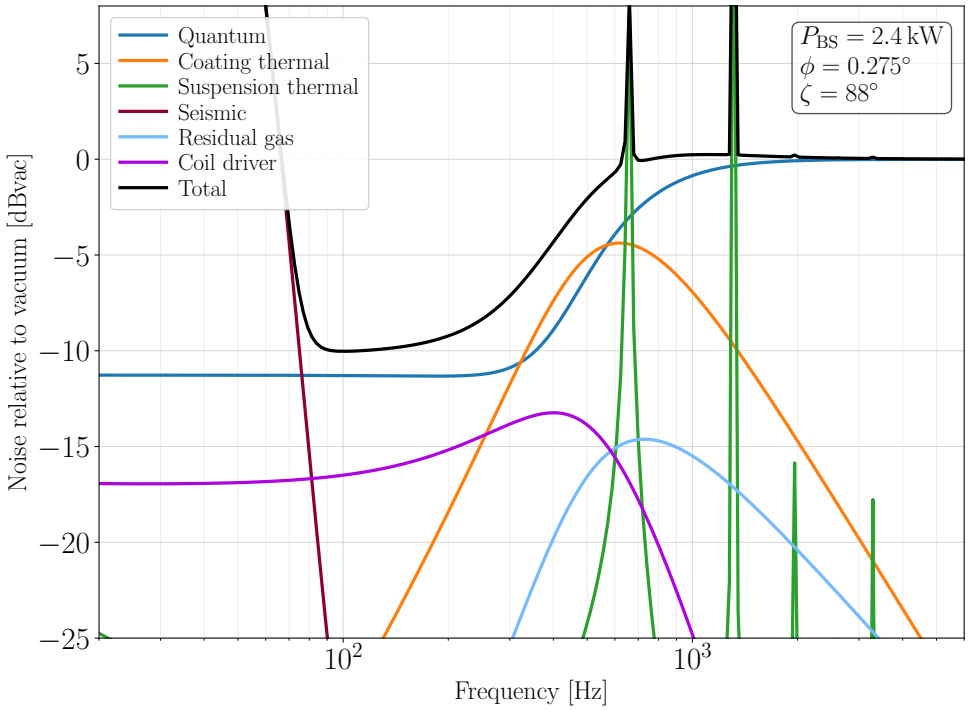

Figure 3.5: 40 m noise budget expressed as noise relative to unsqueezed vacuum noise in decibels below vacuum, i.e. $20\log_{10}\left(S_{b_\zeta}^{1/2}/S_a^{1/2}\right)$. Squeezing below vacuum occurs for negative values.

vacuum noise that would be observed in the photodiode if no signal was being measured, i.e. $S_a^{1/2}/|H|$. This is the noise we are trying to beat. The blue trace labeled "Quantum" is the (signal referred) quantum noise that exits the interferometer, i.e. $S_{b_\zeta}^{1/2}/|H|$. The black trace is the sum of the quantum noise exiting the interferometer and the classical noises described in Sec. 3.3. Squeezing below vacuum is observed when there is less noise exiting the interferometer than unsqueezed vacuum, i.e. when the black total noise is below the red vacuum noise.

The second way of thinking about the noises is to directly look at their magnitude relative to the unsqueezed vacuum S_a, an example of which is shown in Fig. 3.5. To convert a displacement noise as shown in Fig. 3.4 to a relative noise as shown in Fig. 3.5, one multiplies by the DARM transfer function $|H|$. To convert a relative noise as shown in Fig. 3.5 to a displacement noise as shown in Fig. 3.4, one divides the relative noise by

the DARM transfer function. For the following discussion we will mostly use this second method of plotting the relative noises since it directly captures our goal of observing noise below standard vacuum noise: negative values are places where the noise is squeezed below vacuum levels.

Once the parameters given in Tab. 3.1 are set, two questions remain. First, "What should the SRC detuning ϕ be?" And second, "At what homodyne angle ζ should we measure?" It is important to note that, unlike in an interferometer used for detecting gravitational waves, we are not trying to measure a differential arm signal generated in the phase quadrature $b_{\zeta=0}$. In order to maximize the signal to noise ratio of a signal, the readout angle should neither be along the signal to maximize the signal nor in the direction of lowest noise to minimize the noise [37, 38]. But we are not trying to measure a signal at all and are thus just looking for the direction of minimal noise. In fact, as is discussed below in Sec. 3.3, we want to be as insensitive to a differential arm signal as possible.

It follows from (3.18) that the maximum squeeze factor below vacuum is

$$r_{\max} = \frac{1}{2}\operatorname{arcsinh}\left(\frac{1}{2}\sqrt{(S_{b_1} - S_{b_2})^2 - 4S_{b_1 b_2}}\right) \tag{3.19}$$

and occurs at a homodyne angle of[6]

$$\begin{aligned}\zeta_{\max} &= \frac{1}{2}\operatorname{arccot}\left(\frac{S_{b_2} - S_{b_1}}{2S_{b_1 b_2}}\right) = \frac{1}{2}\operatorname{arccot}\left(\frac{\bar{C}_{21}^2 - \bar{C}_{12}^2}{2\bar{C}_{11}}\right) \\ &= \frac{1}{2}\operatorname{arccot}\left(t_s^2\frac{2\sin 2\phi - \mathcal{K}\cos 2\phi}{2\bar{C}_{11}}\right).\end{aligned} \tag{3.20}$$

It is important to note that these values are *frequency dependent*, due to the frequency dependence of the optomechanical interaction $\mathcal{K}$ described above in (3.16), and illustrated

[6] Unless

$$\frac{\partial^2 S_\zeta}{\partial \zeta^2} = 2(S_{b_1} - S_{b_2})\cos 2\zeta - 4S_{b_1 b_2}\sin 2\zeta < 0,$$

in which case $\zeta_{\max} \to \zeta_{\max} + \pi/2$.

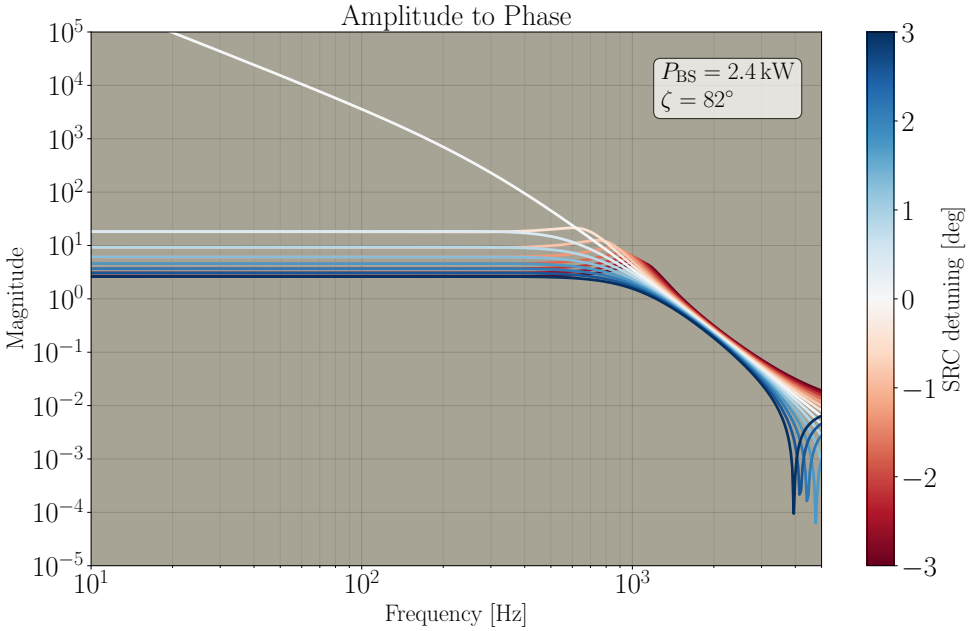

Figure 3.6: Amplitude to phase conversion for signal recycling

in Figs. 2.2 and 2.3, and so it is not a well defined task of simply finding a set of angles that minimizes the noise. Though it is in principle possible to measure the optimal angle at all frequencies by sending the output from the interferometer through a filter cavity [25], we do not consider this extreme complication here.

Signal Recycling We start by analyzing the noise near signal recycling $\phi \approx 0$, which will ultimately be the optimum configuration for the measurement. Since the carrier does not get a net phase rotation in the SRC for $\phi = 0$, the amplitude quadrature is still at $\zeta = \pi/2$ and the phase quadrature, where a differential arm signal would be, is still at $\zeta = 0$. It is therefore still mainly the amplitude to phase conversions, given by the C_{21} matrix element of the matrix C in (3.3), that are responsible for ponderomotive squeezing. The C_{21} amplitude to phase matrix element is plotted in Fig. 3.6 for several SRC detunings near $\phi = 0$. It is clear that $\phi = 0$ has the most amplitude to phase conversion, and therefore the most squeezing. For $\phi = 0$, the free mass behavior of the

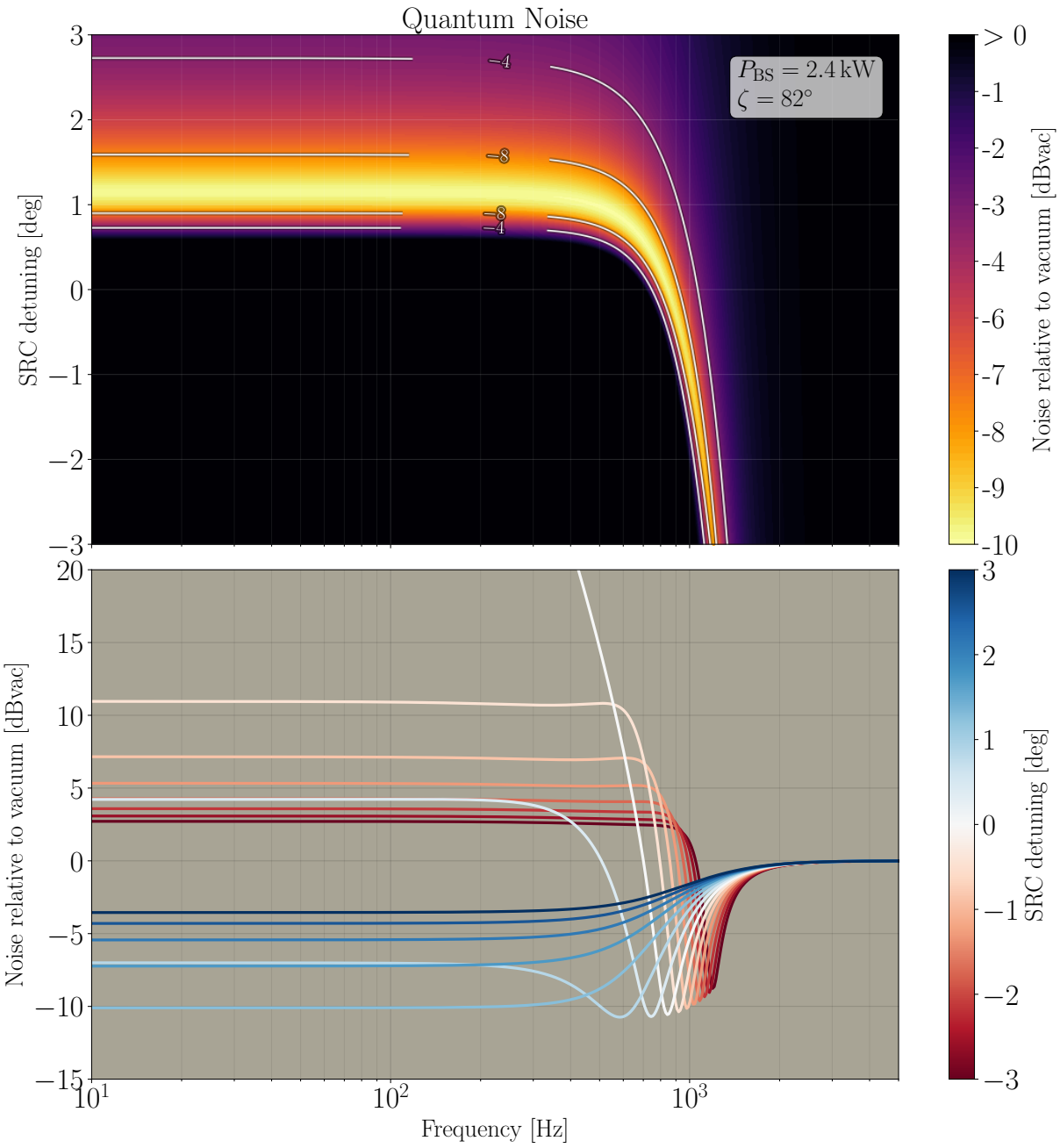

Figure 3.7: Squeezing as a function of SRC detunings near signal recycling with quantum noise only

coupling falling like f^{-2} is evident below the cavity pole f_a with the coupling falling like f^{-4} above the coupled cavity pole f_p due to the f^{-2} filtering of the DARM cavity. For $\phi \neq 0$, the coupling is flat below f_p. This is because the presence of an optical spring or anti-spring leads to the response rising like f^2 below the spring frquency ξ^2; see (3.6), (3.14), and Fig. 3.3. This f^2 rise from the spring or anti-spring cancels the f^{-2} fall from the free mass response to radiation pressure and reduces the overall conversion of amplitude to phase fluctuations below the coupled pole.

Fig. 3.7 shows squeezing as a function of SRC detuning ϕ at fixed homodyne angle ζ. Fig. 3.8 show the corresponding quantum noise ellipses at several detunings at a fixed frequency. The left plot of Fig. 3.8 shows the standard quantum noise ellipses, the radial black line in the plots is the homodyne angle used in Fig. 3.7, and the red dashed circle is the unsqueezed vacuum noise. It is clear from the left plot in Fig. 3.8 that $\phi = 0$ has the most squeezing below vacuum as discussed above and shown in Fig. 3.6. However, $\phi = 0$ is not a good choice. When actually measuring the field at a certain homodyne angle ζ, it is not the value of the noise on a noise ellipse at the angle ζ but rather the projection of the noise ellipse onto a radial line extending from the origin in the ζ direction that is measured. It is true that $\phi = 0$ has the most squeezing in the amplitude quadrature, but it also has the most anti-squeezing in the phase quadrature. As soon as one moves off the axis orthogonal to the anti-squeezing, the anti-squeezing swamps the squeezing and the observed noise is above vacuum noise. The right plot in Fig. 3.8 shows this projection of the noise on the observation direction. In this plot, every angle where the projected noise is below the red vacuum noise is an angle where squeezing would be observed. As is evident from this figure, the $\phi = 0$ noise does indeed have the maximum squeezing below vacuum, but this occurs only for an extremely narrow range of homodyne angles.

Note that as the SRC detuning is increased from negative values to positive values, the noise ellipses in Fig. 3.8 rotate counterclockwise. For $\phi = 0$ the direction of squeezing

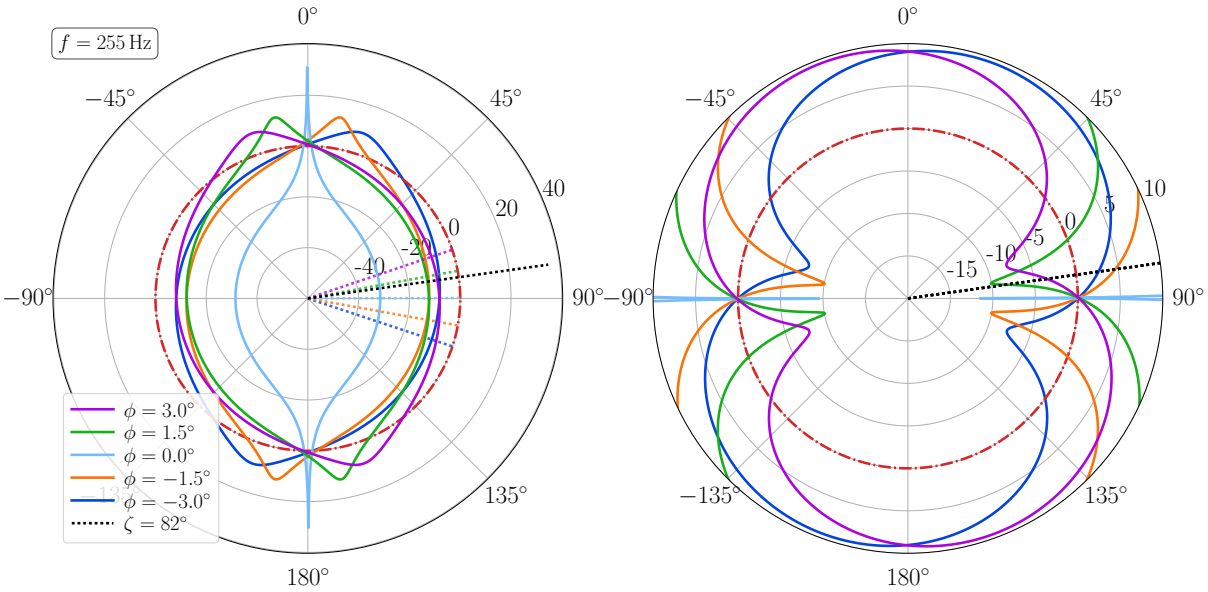

Figure 3.8: Quantum noise curves as a function of SRC detuning near signal recycling. The radial dotted lines in the left plot show the optimum homodyne angle to readout to observe the most squeezing below vacuum (at this frequency). The radial black dotted lines show the homodyne angle used in Fig. 3.7. The red dashed circle is the unsqueezed vacuum noise. The left plot is the standard quantum noise ellipse as introduced in Fig. 2.3 where the radial distance is the noise relative to vacuum noise measured in dBvac. The right plot is the noise one would see by observing at a given homodyne angle, i.e. the projection of the noise in the left plots in the direction of observation, again measured in dBvac. For the right plots, squeezing below vacuum occurs anywhere the noise curve is below the red vacuum noise; it is not as straightforward to see by eye where the noise is squeezed below vacuum in the left plots. Note that the right plots are zoomed very far in so that the large anti-squeezing is not visible for all angles. See text for details.

is along $\zeta = \pi/2$.[7] For negative ϕ, the carrier gains less phase in the SRC than for $\phi = 0$ and so these ellipses are rotated clockwise of the $\phi = 0$ ellipse. For positive ϕ, the carrier gains more phase in the SRC and so these ellipses are counterclockwise of the $\phi = 0$ ellipse.

We can now understand the structure of the quantum noise in Fig. 3.7. For detunings from around 1° to 3°, the noise is squeezed below vacuum and is approximately constant until around 600 Hz. Recall that the noise ellipses rotate counterclockwise and become more circular as frequency is increased and the effects of radiation pressure subside; see Figs. 2.2 and 2.3. In Fig. 3.8, it is only the $\phi = 1.5°$ and $\phi = 3°$ angles that are below vacuum at the given homodyne angle. The ellipses don't start to appreciably rotate until around 600 Hz, at which time the dip below vacuum for both of these detunings has rotated counterclockwise past the observed homodyne angle. At the same time, the dip below vacuum for the $\phi = -1.5°$ and $\phi = -3°$ ellipses is clockwise of the observed homodyne angle for the frequency plotted in Fig. 3.8. But, as the frequency increases, this dip briefly rotates counterclockwise through the observed homodyne angle. This explains why the band of squeezing in Fig. 3.7 is relatively constant for positive detunings and low frequencies and then rapidly moves up in frequency as the detuning becomes more negative.

Finally, note that the squeezing (and anti-squeezing) is reduced as $|\phi|$ is increased. This is because the gain g_{vac} given by (3.8) decreases from $(1 - r_s)^{-2}$ for SR at $\phi = 0$ to $(1 + r_s)^{-2}$ for RSE at $\phi = \pi/2$. The tuning of ϕ thus provides a trade off: small ϕ has more squeezing but for a smaller range of homodyne angles and frequencies, while large ϕ has less squeezing but for a larger range of homodyne angles and frequencies. This trade off can be seen from the depth and width of the dips below vacuum in Fig. 3.8.

[7] This is true for the frequency plotted in Fig. 3.8 since the frequency is low enough that the ellipses have not yet started to appreciably rotate counterclockwise as the effects of radiation pressure diminish. At higher frequencies the direction of squeezing for $\phi = 0$ would be counterclockwise of $\zeta = \pi/2$.

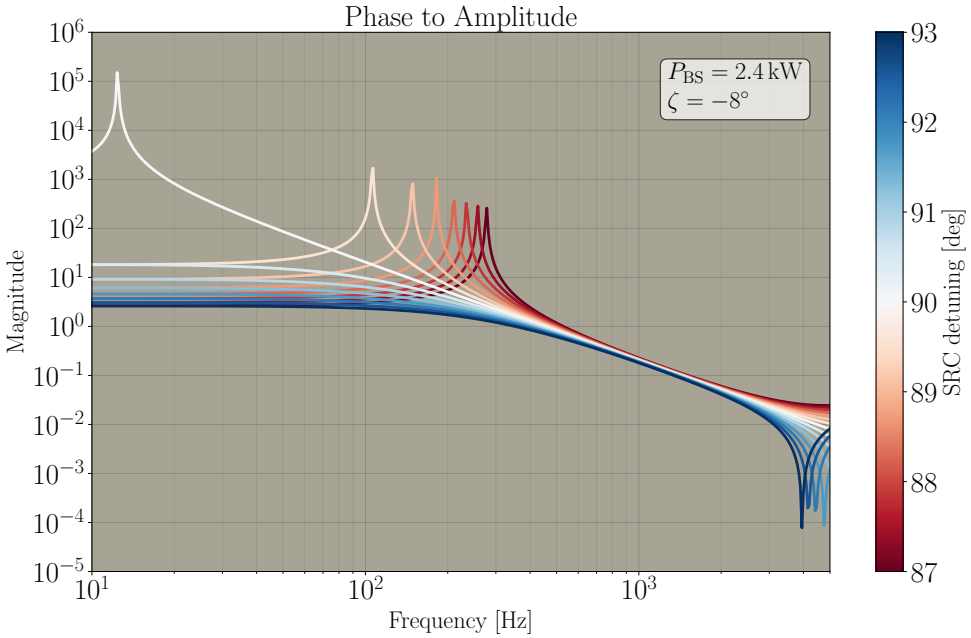

Figure 3.9: Phase to amplitude conversion for resonant sideband extraction

Resonant Sideband Extraction Next, consider the noise near resonant sideband extraction $\phi \approx \pi/2$. Since the carrier gets a $\pi/2$ phase shift traveling one way in the SRC, the amplitude quadrature is now at $\zeta = 0$ and the phase quadrature, where a differential arm signal would be, is now at $\zeta = \pi/2$. It is therefore mainly the phase to amplitude conversions, given by the C_{12} matrix element of the matrix C in (3.3), that are responsible for ponderomotive squeezing. The C_{12} phase to amplitude matrix element is plotted in Fig. 3.9 for several SRC detunings near $\phi = \pi/2$.

The physics responsible for generating the ponderomotive squeezing for $\phi \approx \pi/2$ is the same as is responsible for squeezing for $\phi \approx 0$: it is still a radiation pressure induced modulation of the mirrors getting converted to a phase fluctuation in the light. The difference is that what are the amplitude and phase quadratures at the input to the asymmetric port are swapped by the $\pi/2$ rotation in the SRC when they enter the arms. That the squeezing generation is the same in both cases can be seen quantitatively by

expanding (3.15) for an interferometer operating near SR with $|\phi| \ll 1$

$$\bar{C}_{11} = (1+r_s^2)(1+\mathcal{K}\phi)-2r_s\frac{1-(f/f_a)^2}{1+(f/f_a)^2}, \qquad \bar{C}_{12} = -2t_s^2\phi, \qquad \bar{C}_{21} = t_s^2(2\phi-\mathcal{K}) \tag{3.21a}$$

and for an interferometer operating near RSE with $\phi = \pi/2 + \tilde{\phi}$ where $|\tilde{\phi}| \ll 1$

$$\bar{C}_{11} = -(1+r_s^2)(1+\mathcal{K}\tilde{\phi}) - 2r_s\frac{1-(f/f_a)^2}{1+(f/f_a)^2}, \qquad \bar{C}_{12} = t_s^2(2\tilde{\phi}-\mathcal{K}), \qquad \bar{C}_{21} = -2t_s^2\tilde{\phi}. \tag{3.21b}$$

Indeed, the conversion of amplitude to phase fluctuations responsible for ponderomotive squeezing for SR $\bar{C}_{21}$ is the same as the conversion of phase to amplitude fluctuations responsible for the squeezing for RSE $\bar{C}_{12}$. The other off-diagonal matrix elements are similarly swapped. Once the squeezing is generated in the arms, however, the propagation through the rest of the interferometer, described by the prefactor in (3.14), is responsible for the different behaviors between the two tunings.

In comparing the amplitude to phase coupling of the SR tuning shown in Fig. 3.6 with the phase to amplitude coupling of the RSE tuning shown in Fig. 3.9, the free mass behavior of the phase to amplitude coupling falling like f^{-2} is still visible for $\phi = \pi/2$ at low frequencies. Furthermore, the RSE coupling is still flat in frequency for low frequencies because the f^2 rise of the spring or anti-spring cancels the f^{-2} fall from the free mass response. However, in the RSE case shown in Fig. 3.9, the coupling continues to fall like f^{-2} instead of falling faster like f^{-4}. As is discussed in Sec. 3.1, the spring/anti-spring frequency ξ^2 is below the coupled pole frequency f_p for RSE but above it for SR—in the case of the 40 m with these parameters at least where the coupled pole f_p is greater than the arm pole $f_a = 4.4\,\mathrm{kHz}$ for RSE. Because it is the low pass filtering of the DARM cavity that is responsible for the extra f^{-2} decay, the phase to amplitude coupling continues to fall like f^{-2} for a free mass above the spring frequency.

Fig. 3.10 shows squeezing as a function of SRC detuning near RSE, and Fig. 3.11 shows the corresponding quantum noise ellipses. The fact that the phase and amplitude

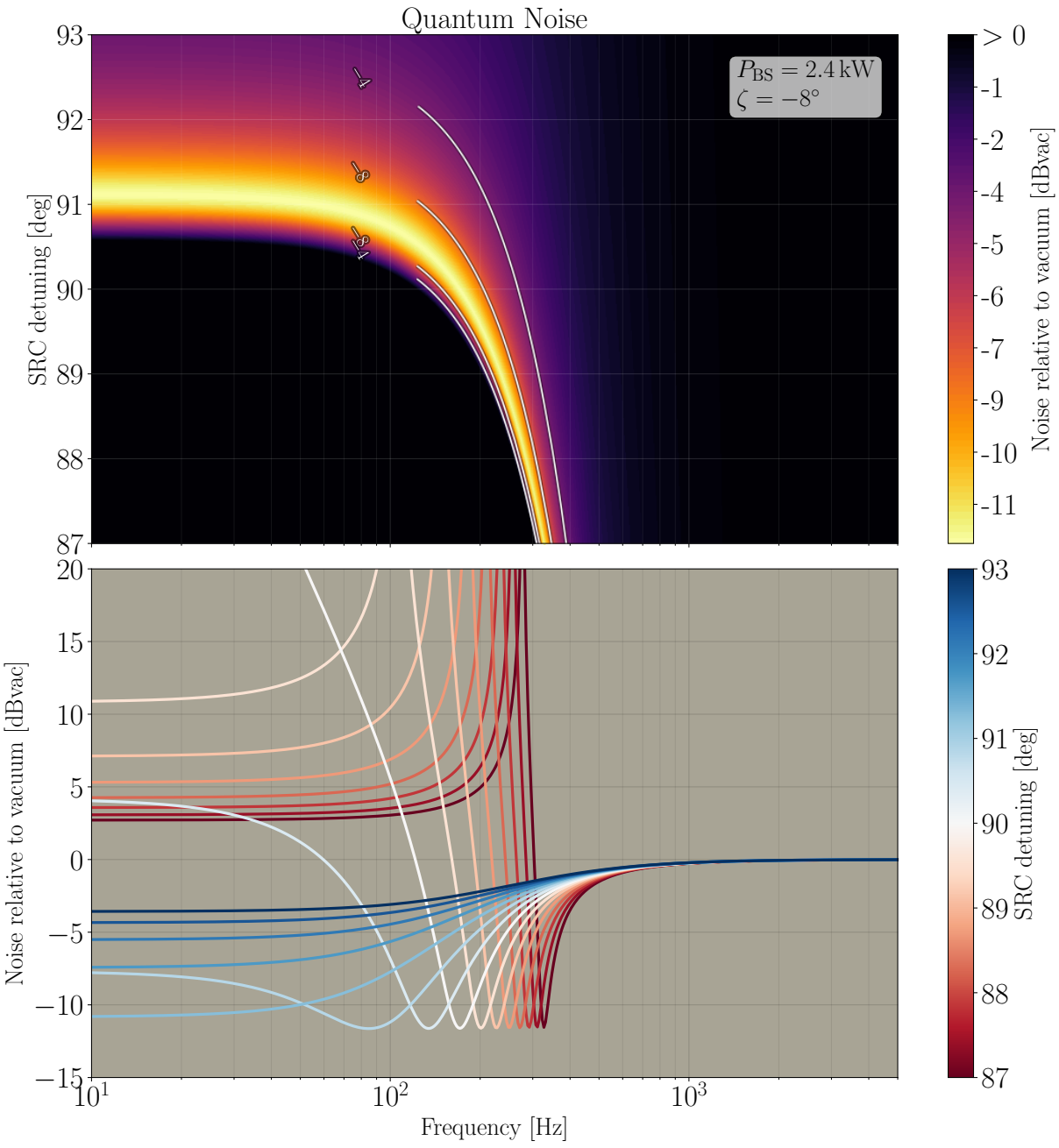

Figure 3.10: Squeezing as a function of SRC detunings near resonant sideband extraction with quantum noise only

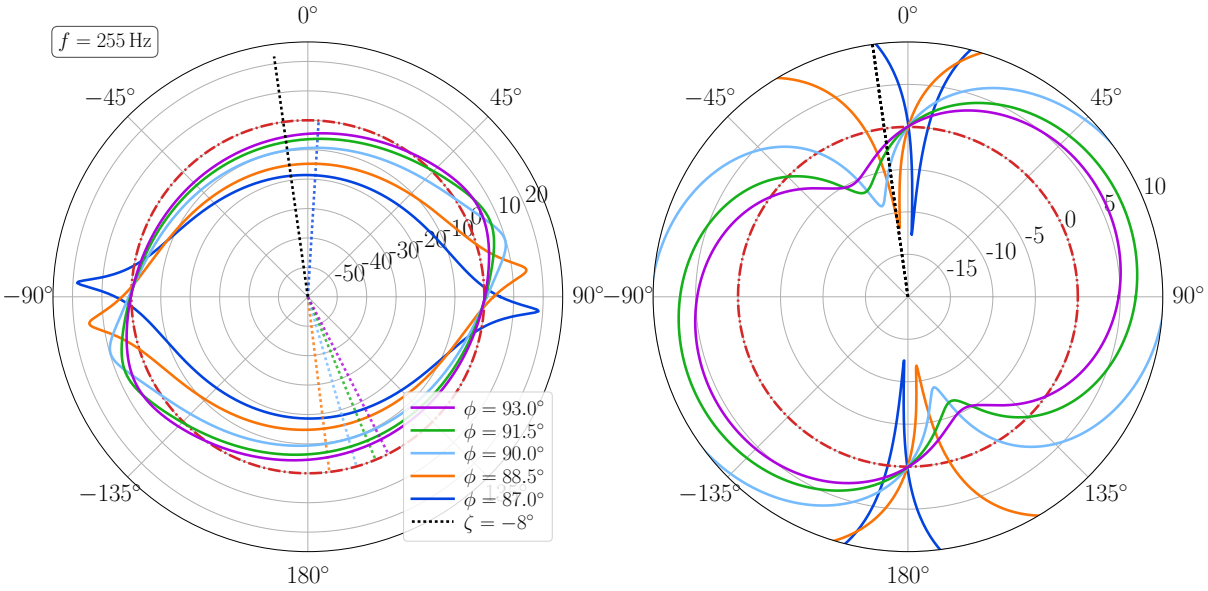

Figure 3.11: Quantum noise curves as a function of SRC detuning near resonant sideband extraction. The radial black dotted lines show the homodyne angle used in Fig. 3.10. See caption for Fig. 3.8

quadratures have been rotated by $\pi/2$ is evident in Fig. 3.11. The overall structure of the quantum noise for RSE shown in Fig. 3.10, with the exception of the resonance from the optical spring, is similar to that for SR shown in Fig. 3.7. The same considerations about the noise ellipses rotating counterclockwise both as the detuning is increased and as the frequency is increased apply in both cases. The major difference is that the region of squeezing below vacuum is shifted to lower frequencies for RSE as compared to SR. This is because the noise ellipses don't start to appreciably rotate counterclockwise as frequency is increased until the optomechanical coupling starts to decrease. As can be seen from Figs. 3.6 and 3.9 this starts to happen at lower frequencies for RSE than for SR. This is also evident by looking at the rotation of the noise ellipses for RSE in Fig. 3.11 compared to that for SR in Fig. 3.8.

3.3 Ponderomotive Squeezing in the Presence of Classical Noise

In reality there are several sources of classical and technical noise which must be considered in addition to the quantum noise discussed in Sec. 3.2 when trying to observe noise squeezed below the vacuum level. These noises are shown along with the quantum noise in the noise budgets in Figs. 3.4 and 3.5.

The displacement noises shown in Fig. 3.4 couple to the fields at the output of the interferometer through the DARM transfer function (3.5). The total noise at the output is therefore

$$S_{b_\zeta}^{(\mathrm{tot})} = S_{b_\zeta} + |H|^2 S_x^{(\mathrm{class})}, \tag{3.22}$$

where S_{b_ζ} is the quantum noise given by (3.18) and analyzed in Sec. 3.2, and $S_x^{(\mathrm{class})}$ are all of the classical displacement noises. To reduce the effects of classical noise, we therefore want the sensitivity to differential arm signals, and thus to gravitational waves, to be as small as possible.

The DARM transfer functions for the SRC detunings shown in Figs. 3.7 and 3.10 are shown in Fig. 3.3. From the perspective of reducing the effects of classical noise, detuning is beneficial because the presence of an optical spring or anti-spring reduces the sensitivity to classical noises below the spring frequency. As can be seen from Fig. 3.3, even though the low frequency response for RSE ($\phi = \pi/2$) is less than that for SR ($\phi = 0$), the response for small detunings away from RSE is about an order of magnitude greater than that for small detunings away from SR. Furthermore, the f^2 rise in the low frequency sensitivity for the detunings away from RSE flattens out before the rise for detunings near SR. Both of these effects are due to the spring frequency being lower near RSE than near SR as discussed above.

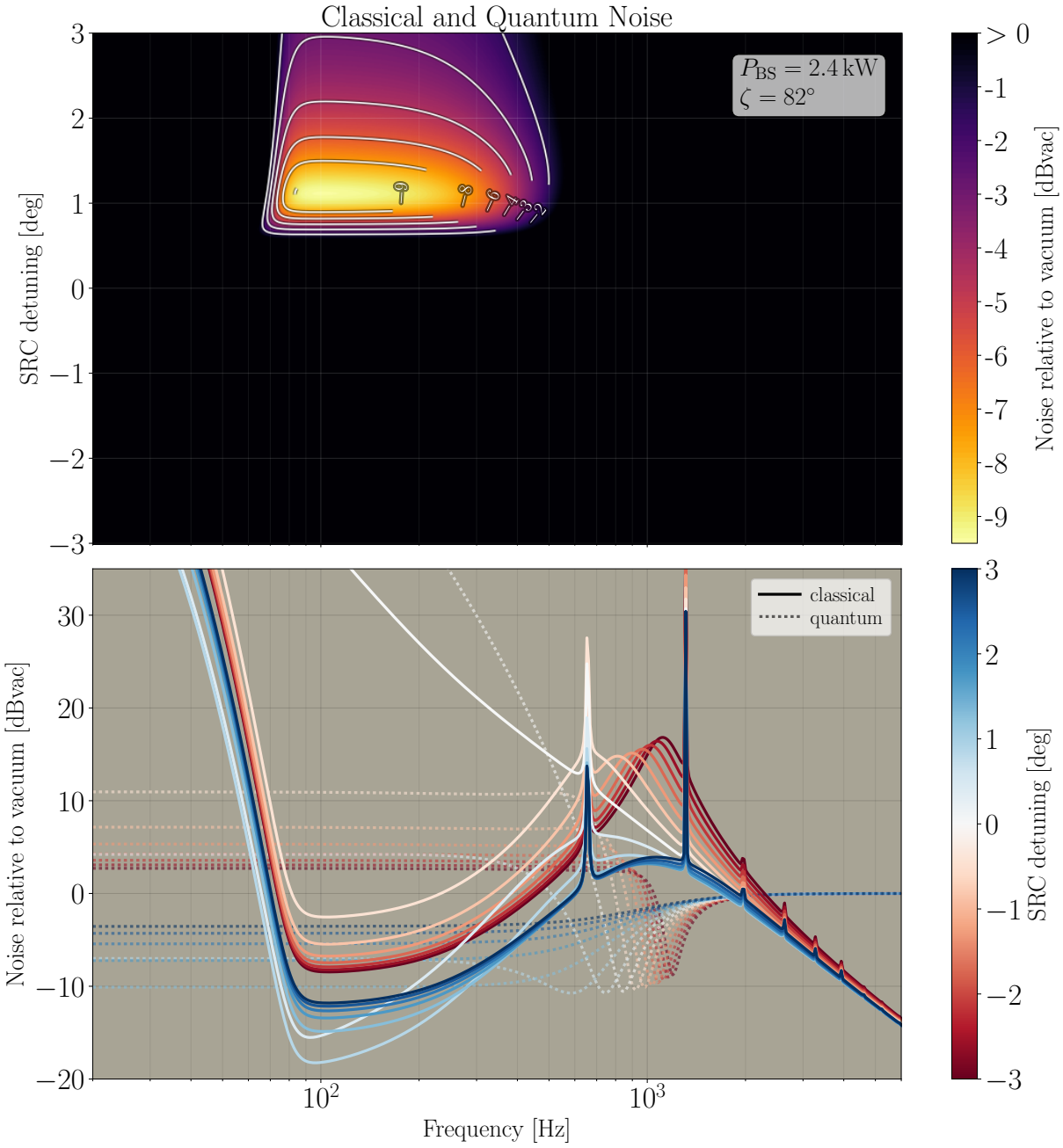

Figure 3.12: Squeezing as a function of SRC detunings near signal recycling with both classical and quantum noise. The light dotted traces in the bottom figure are the quantum contributions to the total noise and are the same as those plotted in the lower figure of Fig. 3.7.

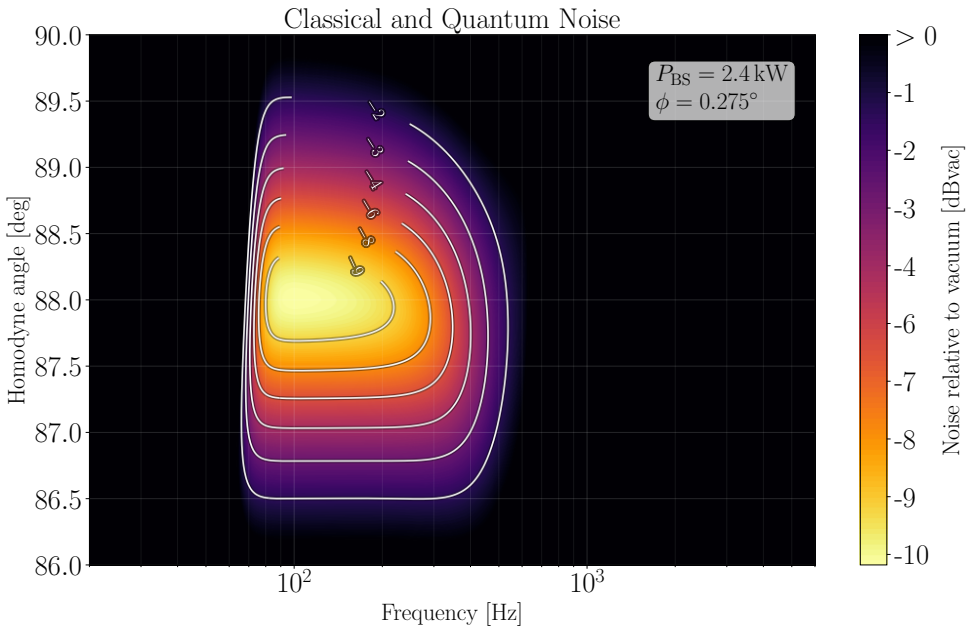

Figure 3.13: Squeezing as a function of homodyne angle with both classical and quantum noise

From the standpoint of reducing classical noise, tunings near SR are therefore better. Fig. 3.12 shows squeezing as a function of SRC detuning when the classical noise is included. The light dotted traces are the quantum contributions to the total noise and are the same as those shown in Fig. 3.7. The squeezing has been reduced to a bucket from around 70 Hz to 500 Hz and exists only for positive detunings $\phi > 0$, which corresponds to the spring. At low frequencies it is limited by seismic noise. At higher frequencies, the noise ellipses are starting to rotate and so the only place the quantum noise is below vacuum is for negative detunings $\phi < 0$, which corresponds to the anti-spring; see Fig. 3.7. But for these tunings, the resonances caused by the coupled pole and the optical anti-spring lead to the peak in the sensitivity to classical noises which causes the total noise to be greater than vacuum. There is no squeezing below vacuum when classical noise is included with any of the tunings near $\phi = \pi/2$ shown in Fig. 3.10 due to the higher sensitivity to classical noise here.

For illustrative purposes, the examples used in the last two sections have used a homodyne angle of 82° for detunings near $\phi = 0°$ and a homodyne angle of $-8°$ for detunings near $\phi = 90°$. There is, however, a trade off between the amount of squeezing and the range of frequencies and homodyne angles over which that squeezing occurs, as was discussed in Sec. 3.2. There is more squeezing confined to a smaller region of parameter space for detunings closer to 0° and homodyne angles closer to 90°. For these reasons, the optimal angles to use for this experiment are closer to $\phi = 0.275°$ and $\zeta = 88°$. These are the parameters used for the noise budgets in Figs. 3.4 and 3.5. Fig. 3.13 shows squeezing as a function of homodyne angle for the detuning set at $\phi = 0.275°$.

3.4 Technical Challenges

Sec. 3.3 described the fundamental limits to observing squeezing; however, there are several sources of technical noise that exceed these fundamental noise sources, and which, if not reduced, will make the observation of squeezing impossible.

Coil driver The positions of the suspended optics are controlled electromagnetically. As is shown in Fig. 3.14, each mirror has five magnets glued onto it: four on the back at the corners of a square and one on the side. Around each magnet a coil of wire is attached to the suspension cage. By adjusting the current through each coil, the position and angular orientation of the mirrors can be controlled. This also means that current noise in the coils is converted to a displacement noise on the optics.

A simplified schematic of the circuit controlling the current to a single coil is also shown in Fig. 3.14. The Johnson noise of the series resistor R_s is $S_V^{1/2} = \sqrt{2k_\mathrm{B}TR_s}$ and is the dominant source of current noise in the coil driver circuit at the values necessary to observe squeezing. The current in a coil produces a force $F = \alpha I$ on the optic where

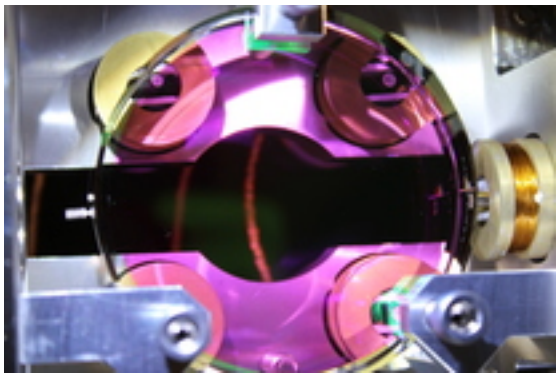

Figure 3.14: Electromagnetic control of suspended optics. Left: the 40 m ETMY showing the five electromagnets used to control its position and angular orientation. The steel wire suspension is also visible. Right: a highly simplified schematic of the coil driver circuit.

α is approximately 0.016 N/A. The displacement noise due to Johnson noise of the series resistor of a single coil is thus

$$S_x^{1/2} = \sqrt{\frac{2k_{\text{B}}T}{R_s}} \frac{\alpha}{m(2\pi f)^2}. \tag{3.23}$$

The total noise on one mirror is the quadrature sum of the four electromagnets controlling position $2S_x^{1/2}$. To decrease this coil driver noise, the series resistance should be increased, however this requires higher input voltages V_{in} to produce a given force on an optic. The current through the series resistor R_s is $I_s = V_{\text{in}}R_2/R_1R_s$. So if the maximum force needed to control the mirrors is F_{max}, the maximum input voltage necessary is $V_{\text{in}} = (R_1R_s/R_2)(F_{\text{max}}/\alpha)$. High voltage coil driver circuits are currently being designed so that the series resistance can be increased sufficiently high to observer squeezing.

Local oscillator intensity noise As is discussed in Appendix B, the output from the interferometer is mixed with a strong local oscillator (LO) in order to measure the signal in a method known as balanced homodyne readout. In principle, any noise on the LO is canceled if the signal is small. Unfortunately, the output from the interferometer is not small in practice and is dominated by "junk light."

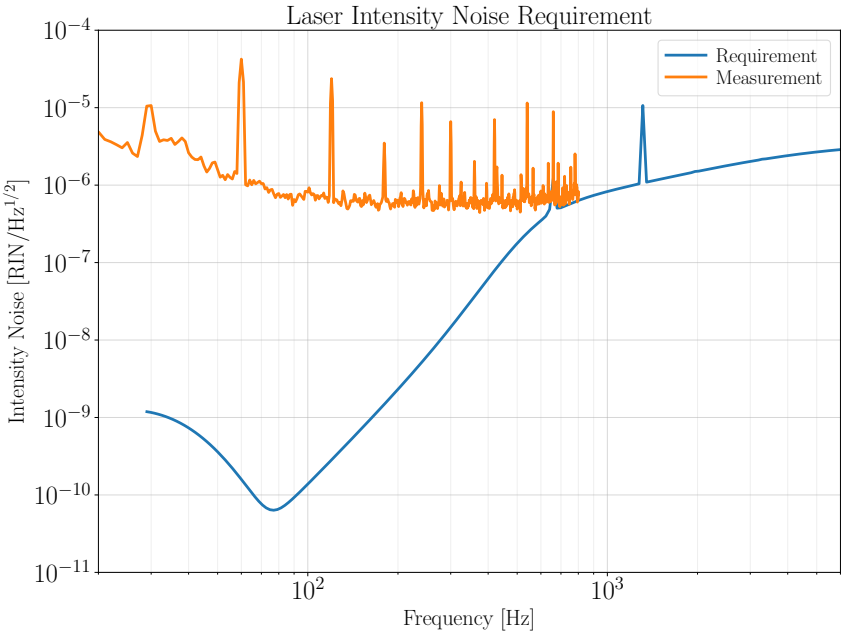

Figure 3.15: Requirements for laser intensity noise at the input to the interferometer (back of PRM) to be ten times less than the total noise goal in Fig. 3.4 for a contrast defect of 1 mW.

In a perfect Michelson interferometer with a perfect 50/50 beam splitter and end mirrors with the exact same reflectivity, there is no light at the asymmetric port in the absence of a differential arm signal. However, if these conditions are not exactly met, there will not be a perfect cancellation at the beam splitter and some light, known as the contrast defect, will leak out to the asymmetric port. In a Fabry-Perot Michelson interferometer, differences in the two arms lead to different arm reflectivities and cavity poles. The contrast defect caused by the presence of these imperfections exits the interferometer in the amplitude quadrature.

The contrast defect can then beat with the local oscillator light creating a signal that is not canceled in the balanced homodyne readout. Since the contrast defect is in the amplitude quadrature, its presence makes the measurement susceptible to amplitude noise on the LO. Since some light from the power recycling cavity (about 50 mW) would be taken to make the LO in the 40 m, this sets a requirement on the intensity noise

present on the light going into the interferometer, as is shown in Fig. 3.15. Taking the LO from the power recycling cavity rather than from some other source, such as another laser, benefits from the LO automatically having the amplitude stability of the main beam and getting passively filtered by the power recycling cavity.

OMC displacement noise As is mentioned in Appendix. A, the laser is phase modulated with two sets of RF sidebands so that the interferometer length degrees of freedom can be controlled. Ref. [39] explains the need for these sidebands and their use in controlling the interferometer. However, these sidebands need to be removed from both the signal and LO before the homodyne detection is done. This is done by sending the signal and LO through a resonant bowtie cavity called the output mode cleaner (OMC). Since the OMC has a bandwidth less than the RF sideband frequencies, the sidebands do not resonate and are filtered from the signal and LO.

Early plans to use homodyne detection in gravitational wave detectors assumed that separate OMCs would be used for both the LO and signal before the beamsplitter where the two are mixed [40]; see Appendix. B. However, displacement noise in the OMC gets converted into phase noise, and subsequent analysis found that this sets very stringent requirements [41]. For this experiment we are considering using a single OMC, described in Appendix B and shown in Fig. B.2, where the signal and LO have different polarizations. We would use the second option shown in Fig. B.2, where the half-waveplate is after the OMC, and where the displacement noise is (B.13). This noise is proportional to $\sin\zeta$ and, since we are reading out almost entirely the amplitude quadrature $|\zeta| < 1°$, we are not affected by OMC displacement noise.

Angular instabilities As we have seen, when a cavity formed by two suspended mirrors is detuned from resonance, the power circulating in the cavity creates an optical

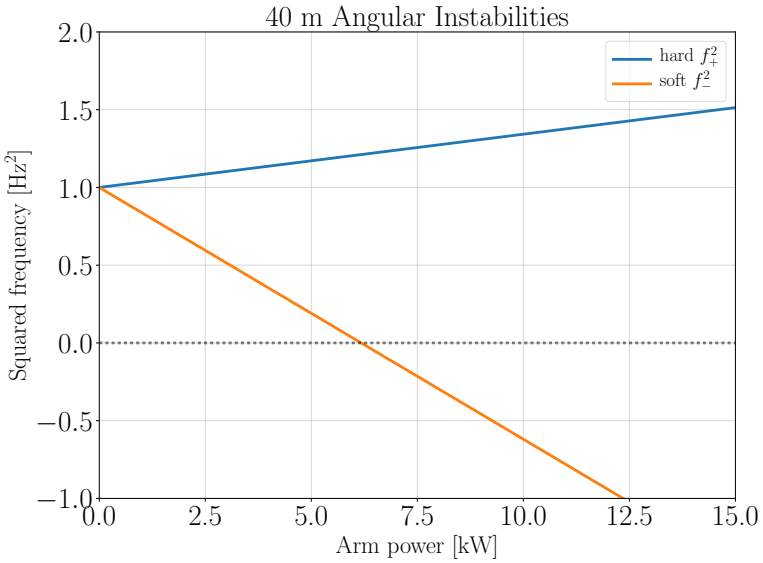

Figure 3.16: Frequencies of the hard and soft modes for the 40 m interferometer

spring: the two mirrors can now excert a force on one another and the mechanical resonance of the free mirrors is increased through the interaction. Similarly, if the laser beams are not centered on the optics, the optomechanical interaction will allow the two mirrors to excert a torque on one another. This interaction modifies the torsional resonance of the free mirrors.

A two mirror cavity has two torsional modes modified by the optomechanical coupling [42–44]. The first mode, called the hard mode, occurs when the beam is off center on opposite sides of the optic. This mode becomes stiffer as the power in the cavity is increased. The second mode, called the soft mode, occurs when the beam is off center on the same sides of the optic. This mode becomes softer as the power in the cavity is increased. If the power in the cavity is sufficiently high, the torque caused by the radiation pressure will exceed the restoring torque of the free mirrors and the soft mode will become unstable.

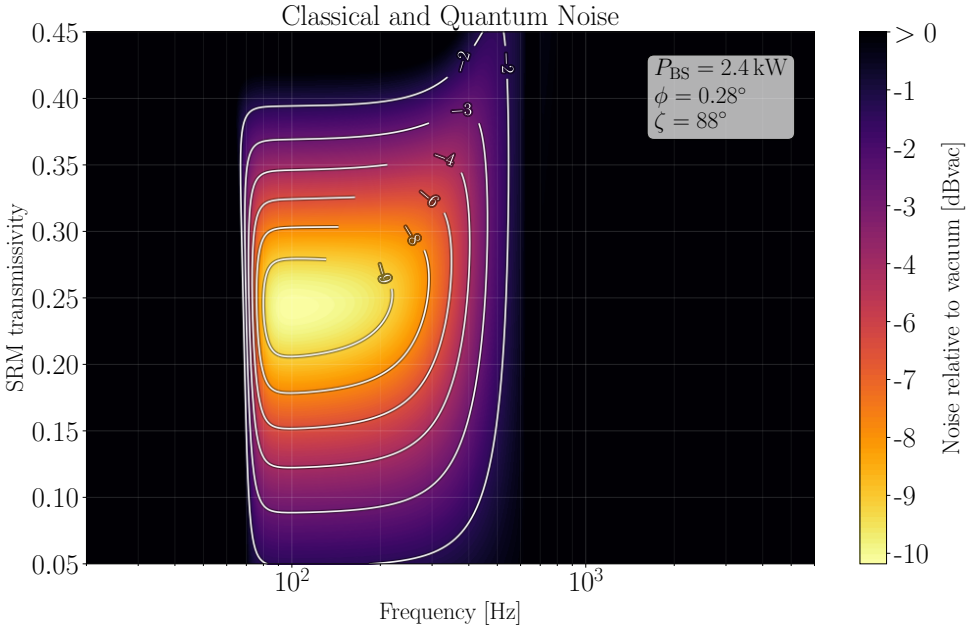

Figure 3.17: Squeezing below vacuum as a function of SRM transmissivity

The resonance frequencies of the hard (+) and soft (-) modes are

$$\omega_{\pm}^2 = \omega_0^2 + \frac{PL}{Ic}\frac{-(g_1+g_2) \pm \sqrt{4+(g_1-g_2)^2}}{1-g_1g_2} \tag{3.24}$$

where ω_0 is the torsional resonance of the free mirror, P is the power in the cavity, L is the cavity length, I is the moment of inertia of a mirror, and $g_{1,2} = 1 - L/R_{1,2}$ are the stability factors of the cavity where $R_{1,2}$ are the radii of curvature of the mirrors. When the power is increased to the point that ω_-^2 becomes negative, the soft mode becomes unstable. Fig. 3.16 shows the resonance frequencies of the hard and soft mode as a function of cavity power for the 40 m interferometer. The arm cavities are predicted to become unstable for arm powers of about 6 kW.

	P_{in} [W]	g_{prc}	T_s	P_{BS} [W]	P_{arm} [kW]	ϕ	ζ	$S_{\text{min}}^{1/2}$ [dBvac]	f_{min} [Hz]
A	1	40	0.099	40	2.9	0.002°	89.7°	−2.5	98
B	1	80	0.099	80	5.7	0.004°	89.7°	−3.6	107
C	10	80	0.099	800	57	0.015°	89.7°	−8.3	95
D	30	80	0.245	2400	340	0.275°	88°	−10.1	100

Table 3.2: Achievable squeezing below vacuum for different 40 m upgrades. Case A is close to the state of the interferometer today and Case D is the configuration considered in the rest of the chapter. The noise for each case is shown in Fig. 3.18. $S_{\text{min}}^{1/2}$ is the minimum total noise which occurs at the frequency f_{min}.

3.5 Prospects for the Future

The parameters from Tab. 3.1 used in the rest of this chapter are not those of the 40 m interferometer today. The current input power to the interferometer is $P_{\text{in}} = 1\,\text{W}$, the power recycling mirror transmissivity is $T_p = 0.056$, and the signal recycling mirror transmissivity is $T_s = 0.099$. After installing new folding mirrors in the power recycling cavity and with the current $T_p = 0.056$, it is expected that a power recycling gain of 40 can be achieved in the near future. In order to maximize the power in the PRC, the reflectivity of the PRM should be equal to the reflectivity of the compound mirror of the effective common arm cavity minus the losses in the cavity. With current estimates of these losses, a new PRM with $T_p = 0.01$ should be able to achieve a recycling gain of about 80, which is the number used in the rest of this chapter.

The possibility of getting a fiber amplifier for the laser is also being considered. It is conceivable that an input power of $P_{\text{in}} = 30\,\text{W}$, the number used in the rest of this chapter, can be achieved with an amplifier.

Though focussing on increasing the power in the arms, either through increasing the input power or by increasing the recycling gain, is most important in increasing the ponderomotive squeezing, adjusting the SRM transmissivity can improve the situation as well. As can be seen from Fig. 3.17, increasing T_s from the current value of 0.099 to

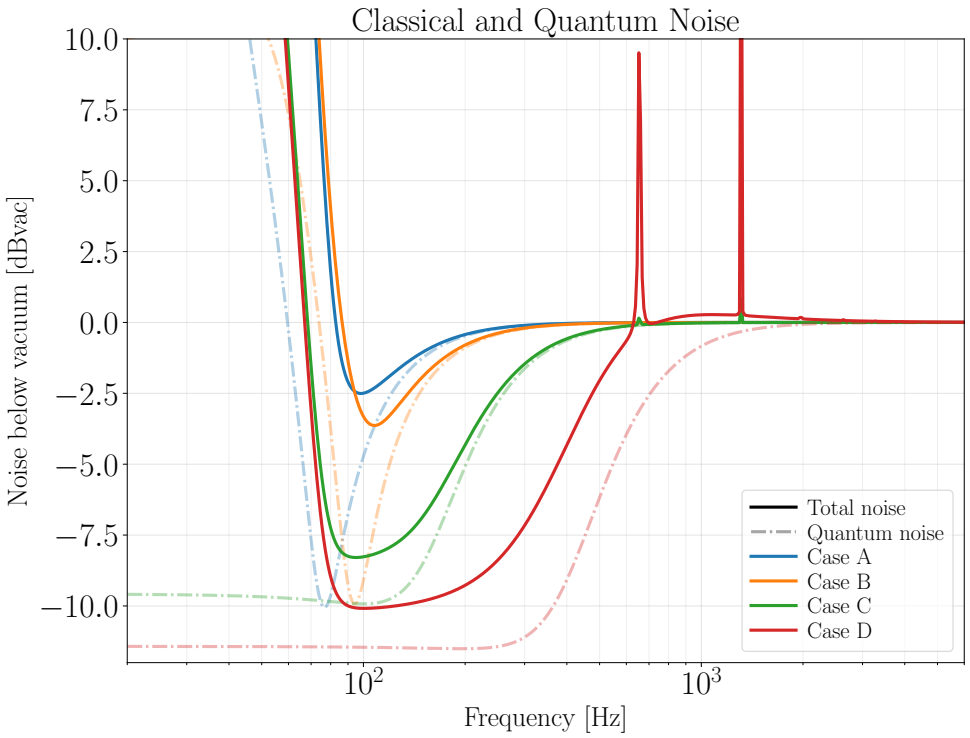

Figure 3.18: Squeezing below vacuum for the different 40 m upgrades listed in Tab. 3.2. The thick lines show the total classical and quantum noise for each case and the light dashed lines show the quantum noise only.

about 0.245, the number used in the rest of this chapter, can increase squeezing by a few dBvac. Since the 40 m is currently setup to operate in RSE, the SRM will need to be moved to operate in SR, as is discussed in Appendix A. Since the radius of curvature of the SRM will then need to be adjusted so that the SRM stays mode-matched with the rest of the interferometer, a new SRM needs to be installed. This gives us the opportunity to choose the SRM transmissivity to maximize squeezing.

Tab. 3.2 lists a few different upgrades to the 40 m interferometer; the noise for each case is shown in Fig. 3.18. As can be seen from the figure, there are two regimes: a low power regime (Cases A and B) and a high power regime (Cases C and D). As the power is reduced, the optomechanical coupling (3.16) is also reduced. As a consequence, the region of squeezing below vacuum shown in Fig. 3.7 moves down to lower detunings and

left to lower frequencies. At high power, the approximately constant region of squeezing below vacuum extends to high enough frequencies for classical noise to also be below vacuum. However, as the power is reduced, the noise ellipses start to appreciably rotate at lower frequencies and it is only the momentary dip below vacuum, shown in Fig. 3.7 and described in the surrounding text, that extends to high enough frequencies for the classical noise to also be below vacuum.

Chapter 4

Quantum Hypothesis Testing and Model Independent Tests of General Relativity

4.1 Introduction

Direct observations of gravitational waves provide a new way to look for deviations from the theory of general relativity. Such tests of general relativity have been carried out [45, 46] with the recent observations of binary black hole and binary neutron star mergers [3–5]. Such searches are an example of hypothesis testing.

There are two classes of hypothesis testing in this context [45–47]. In the first, one has a specific set of alternative theories and asks specifically, "Is this theory or general relativity more likely?" In this case, the data is analyzed with both theories to see if the alternative theory explains the data *significantly* better than GR does. In the second class, one just asks, "Is there any evidence for a deviation from general relativity?" In this case, the data is only analyzed to see if it is consistent with GR. There is no other theory it is being explicitly compared with. It is in this case that the test is "model independent." If the signals are weak, we may be content at first knowing only whether a deviation from GR exists and not in what the details of that deviation are.

In the following, we describe testing whether a signal is or is not present in a coherent state of the electromagnetic field. The discussion is general, but we keep the example of testing for a deviation from GR in mind. In the case of interferometric gravitational wave detectors, we measure the light coming out of the interferometer to see if there is a signal present or not, but there is nothing special to the light exiting an interferometer. Typically one would just measure the signal by mixing it with a strong local oscillator and observing it on a photodiode, with a homodyne detector for example. This measurement suffers from shot noise arising from vacuum fluctuations beating with the local oscillator. Since we are not trying to measure the signal and are content knowing only if one exists, there is another option: we can count photons. By removing the local oscillator, we no longer suffer from the vacuum fluctuations.

Sec. 4.2 gives an example of the benefits of counting photons over measuring a signal directly by looking at the coherent state of a quantum harmonic oscillator. Sec. 4.3 develops the general theory of hypothesis testing with coherent states of the electromagnetic field. Sec. 4.4 describes combining multiple measurements to do hypothesis testing. Finally, Sec. 4.5 gives an example of using these methods to look for deviations from general relativity. Throughout, we compare hypothesis testing using photon counting with hypothesis testing using homodyne detection and always find that photon counting is more sensitive than homodyne detection.

4.2 Hypothesis Testing: A Single Mode

To illustrate the idea of quantum hypothesis testing, suppose we want to measure the displacement α of the coherent state

$$|\alpha\rangle = \mathrm{e}^{-|\alpha|^2/2} \sum_{n=0}^{\infty} \frac{\alpha^n}{\sqrt{n!}} |n\rangle \tag{4.1}$$

of the quantum harmonic oscillator. We could measure the position of the oscillator $X = (a + a^\dagger)/\sqrt{2}$, in which case the distribution of measurement outcomes would be Gaussian

$$P(x|\alpha) = |\langle x|\alpha\rangle|^2 = \frac{1}{\sqrt{\pi}}\mathrm{e}^{-(x-\mu)^2}, \tag{4.2}$$

where the mean is $\mu = \mathrm{Re}\,\alpha$; or, we could measure the number of quanta $N = a^\dagger a$ in the state, in which case the distribution of measurement outcomes would be Poissonian

$$P(n|\alpha) = |\langle n|\alpha\rangle|^2 = \frac{\bar{N}^n}{n!}\mathrm{e}^{-\bar{N}}, \tag{4.3}$$

where the mean number of quanta is $\bar{N} = |\alpha|^2$. In either case, one would make multiple measurements of identical states and, using either (4.2) or (4.3), would infer the value of α.

Now suppose α is small and that we are content knowing only whether α is zero or not. In this case, we could perform hypothesis testing between the null hypothesis $\mathcal{H}_0$ that $\alpha = 0$, signaling the absence of an effect such as a deviation from GR, and the alternate hypothesis that $\alpha \neq 0$, signaling the presence of such an effect. To do so we need to set the criteria for deciding between $\mathcal{H}_0$ and $\mathcal{H}_1$ based on the outcome of a measurement of either X or N. We need to minimize the probability of missing the presence of an effect, the false dismissal rate $P_{\mathrm{FD}} = P(\mathcal{H}_0|\alpha \neq 0)$, while at the same time minimizing the probability of claiming the presence of an effect when there is none, the false alarm rate $P_{\mathrm{FA}} = P(\mathcal{H}_1|\alpha \neq 0)$.

First consider the case where the position X is measured. We will claim $\mathcal{H}_1$ if $|x| \geq r_c$ and claim $\mathcal{H}_0$ if $|x| < r_c$ for some cutoff r_c chosen to minimize P_{FA} and P_{FD}. The false alarm rate is

$$P_{\mathrm{FA}|X} = P(|x| \geq r_c|\alpha = 0) = \frac{2}{\sqrt{\pi}}\int_{r_c}^{\infty}\mathrm{e}^{-x^2}\,\mathrm{d}x = 1 - \mathrm{erf}\,r_c, \tag{4.4}$$

where erf is the error function, and the false dismissal probability is

$$P_{\mathrm{FD}|X} = P(|x| < r_c|\alpha \neq 0) = \frac{1}{\sqrt{\pi}} \int_{-r_c}^{r_c} \mathrm{e}^{-(x-\mu)^2}\, \mathrm{d}x$$
$$= \frac{1}{2}[\mathrm{erf}(\mu + r_c) - \mathrm{erf}(\mu - r_c)]. \tag{4.5}$$

Next consider the case where the number of quanta N is measured. In this case we can actually claim $\alpha \neq 0$ by observing even a single quanta since we know with certainty that $\alpha \neq 0$ if $n > 0$: from (4.3),

$$P_{\mathrm{FA}|N} = P(n > 0|\alpha = 0) = 0. \tag{4.6}$$

The false dismissal rate is

$$P_{\mathrm{FD}|N} = P(n = 0|\alpha \neq 0) = \mathrm{e}^{-\bar{N}}. \tag{4.7}$$

Fig. 4.1 compares the minimum detectable displacement α for counting quanta and measuring position. Quantum noise enters these measurements in different ways. In the case of the position measurement, the Heisenberg uncertainty relation prevents us from perfectly measuring α. In the case of counting quanta, it is the counting statistics of the coherent state, i.e. the shot noise, that prevent a perfect measurement of $\bar{N}$.

4.3 Coherent States of the Electromagnetic Field with Classical Noise

We now describe testing whether signals are present in the electromagnetic field and consider the effects of classical noise on such measurements. Suppose we want to look for signals oscillating at frequencies Ω on top of a strong carrier oscillating at ω_0. For example, the carrier could be a laser and the signals phase fluctuations imprinted on it

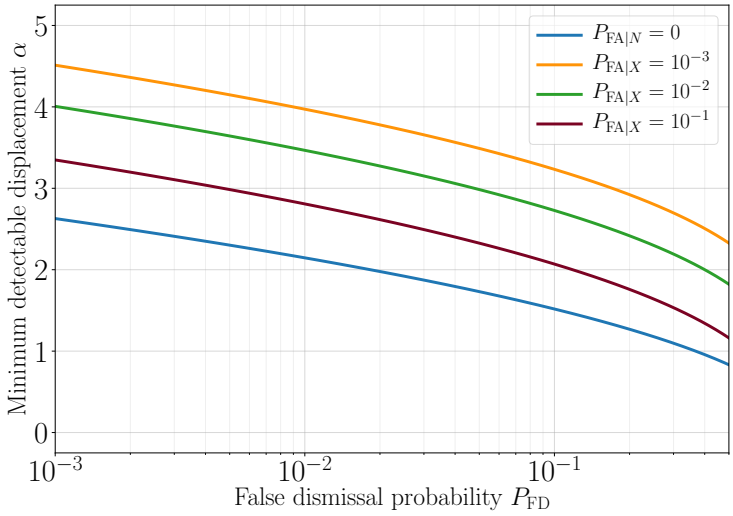

Figure 4.1: Minimum detectable displacement of the quantum harmonic oscillator for counting quanta vs. measuring position. As the false dismissal rate is decreased for position measurements, the minimum displacement increases. The false dismissal rate is zero for counting quanta and the minimum detectable displacement is smaller than that of position measurements even tolerating an error rate as high as 10%.

from a gravitational wave. If $\Omega \ll \omega_0$, as is always the case for lasers, the field can be quantized in the Heisenberg picture as [23–25]

$$E(t) = \sqrt{\frac{2\pi\hbar\omega_0}{\mathcal{A}c}} \mathrm{e}^{-\mathrm{i}\omega_0 t} \int_0^\infty \frac{\mathrm{d}\Omega}{2\pi} \left[a_+(\Omega)\mathrm{e}^{-\mathrm{i}\Omega t} + a_-(\Omega)\mathrm{e}^{\mathrm{i}\Omega t} \right] + \mathrm{hc}. \tag{4.8}$$

where $a_\pm(\Omega) \equiv a(\omega_0 \pm \Omega)$ are the annihilation operators for the upper and lower signal sidebands and $\mathcal{A}$ is the effective cross sectional area of the carrier. To describe such signals it is useful to use the two-photon formalism [23, 24] where states are described by the quadrature operators

$$a_1(\Omega) = \frac{a_+(\Omega) + a_-^\dagger(\Omega)}{\sqrt{2}}, \qquad a_2(\Omega) = \frac{a_+(\Omega) - a_-^\dagger(\Omega)}{\sqrt{2}\mathrm{i}}. \tag{4.9}$$

Any linear combination $a_\zeta = a_1 \sin\zeta + a_2 \cos\zeta$ can be measured but, since it is not important which quadrature is measured in the following discussion, we simply write a to denote an arbitrary quadrature of the field. A two-photon coherent state displaces

both the upper and lower sidebands:

$$b = D_+^\dagger(\alpha_+)D_-^\dagger(\alpha_-)aD_+(\alpha_+)D_-(\alpha_-) = b + \alpha \tag{4.10}$$

where the displacement operators

$$D_\pm(\alpha_\pm) = \exp\left(\alpha_\pm a_\pm^\dagger - \alpha_\pm^* a_\pm\right) \tag{4.11}$$

are the usual one-photon displacement operators exciting either the upper or lower sideband. From the definitions (4.9), we see that the upper and lower sidebands are themselves the excited states

$$D^\dagger(\alpha_+)a_+D(\alpha_+) = a_+ + \frac{\mathrm{i}\alpha}{\sqrt{2}}, \qquad D^\dagger(\alpha_-)a_-D(\alpha_-) = a_- + \frac{\mathrm{i}\alpha^*}{\sqrt{2}}. \tag{4.12}$$

Suppose we are trying to make a linear measurement of a classical signal $h(f)$ with a detector which adds the classical noise $\xi(f)$; see Fig. 4.2. If the field of the carrier is described by the operator a, the total signal measured in the detector will be

$$b(f) = a(f) + H_{\mathrm{det}}(f)[h(f) + \xi(f)] \tag{4.13a}$$

$$= a(f) + s(f) + \frac{\xi(f)}{S_{\mathrm{shot}}^{1/2}(f)}. \tag{4.13b}$$

Here, $H_{\mathrm{det}}(f)$ is the frequency response of the detector and $s(f) = H_{\mathrm{det}}(f)h(f)$ is the signal as actually measured. In the case of an interferometric gravitational wave detector, h is the gravitational wave strain and s is the electromagnetic field measured by a photodiode at the output of the interferometer. If the time-domain signal has the units $[h(t)] = [h]$, then the frequency-domain signal has the units $[h(f)] = [h]/\mathrm{Hz}$, the frequency response has the units $[H_{\mathrm{det}}(f)] = \sqrt{\mathrm{photons/Hz}}/([h]/\mathrm{Hz})$, and the signals measured in the photodiode have units $[b(f)] = [a(f)] = [s(f)] = \sqrt{\mathrm{photons/Hz}}$.

Quantum noise is added to the measurement through the shot noise S_a of the mode $a(f)$, which is described by the single-sided noise spectral density defined as [23–25]

$$\frac{1}{2}\left\langle a(f')^\dagger a(f) + a(f)a(f')^\dagger \right\rangle = \frac{1}{2}\delta(f - f')S_a(f). \tag{4.14}$$

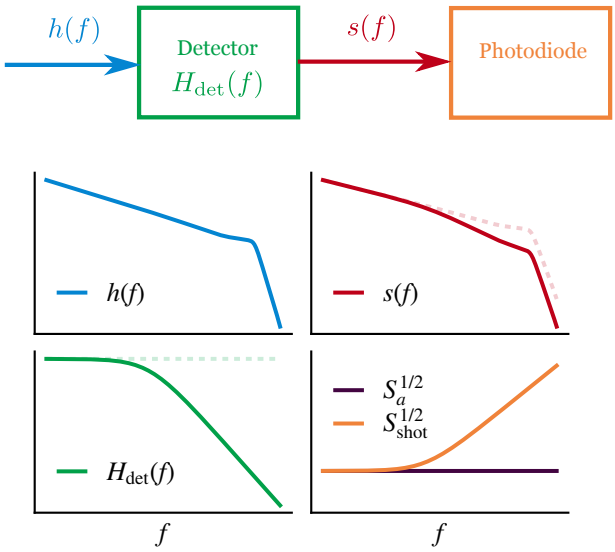

Figure 4.2: Cartoon of the detection process described by (4.13). An incoming signal h is measured by a detector and filtered through the detector's response $H_{\rm det}$. The resulting signal $s = H_{\rm det}h$ is then measured by a photodiode where the shotnoise $S_a^{1/2}$ of the signal field is added in the photodetection process. In order to analyze signals in terms of the signal h itself rather than s, the measurement is divided by $|H_{\rm det}|$. The effective shotnoise is therefore $S_{\rm shot}^{1/2} = S_a^{1/2}/|H_{\rm det}|$. The detector response shown here is that of a low pass filter. The light dotted line is the response for an all pass detector, and the light dotted line in the plot for s is the corresponding signal that would be measured in such a detector. Not shown is the classical noise ξ which can enter this process at any point.

We will only be concerned with coherent states, for which $S_a = 1$. Instead of looking at the noise of the state $b(f)$, it is oftentimes useful to look at the noise of the state $b(f)/H_{\rm det}(f)$ so that the noise is relative to the original signal h itself instead of the signal s filtered through the detector's response. In this case, the shot noise is $S_{\rm shot} = S_a/|H_{\rm det}|^2$ and so the detector response can also be written as $|H_{\rm det}(f)| = 1/S_{\rm shot}^{1/2}(f)$.

We can now consider testing the hypothesis $\mathcal{H}_1$ that there is a signal h, and therefore s, present vs. the hypothesis $\mathcal{H}_0$ that there are no signals. As with the case of the harmonic oscillator of Sec. 4.3.2, we can do this in two ways. First, we can count the number of photons in the state b as is described in Sec. 4.3.1. Second, we can measure the quadrature b directly, which is analogous to measuring the position of the harmonic oscillator, as is described in Sec. 4.3.2. We refer to this method as homodyne detection since this is one method of measuring this quadrature. In both cases we measure signals for a time T over a frequency band B.

4.3.1 Photon Counting

Suppose we measure the number of photons with frequencies within the frequency band B. The number density of photons at frequency f is described by $a_+^\dagger(f)a_+(f) + a_-^\dagger(f)a_-(f)$ and the mean total number of photons is the sum of the number of photons in the upper and lower sidebands:

$$\bar{N} = \int_B \mathrm{d}f \left(|\alpha_+|^2 + |\alpha_-|^2\right) = \int_B \mathrm{d}f\, |\alpha|^2, \tag{4.15}$$

where (4.12) was used. Now if we measure the number of photons in the state (4.13), the expected number of photons averaged over classical noise realizations of ξ is

$$\bar{N} = \int_B \mathrm{d}f \left(|s|^2 + \frac{\langle|\xi|^2\rangle}{S_{\rm shot}}\right). \tag{4.16}$$

The classical noise spectral density is

$$\langle \xi^*(f')\xi(f)\rangle = \frac{1}{2}\delta(f-f')S_\xi(f). \tag{4.17}$$

Since the signal lasts for a finite time T, the delta function should be taken as $\delta(0) \to T$ so that

$$\bar{N} = \int_B \mathrm{d}f\ |s|^2 + \frac{T}{2}\int_B \mathrm{d}f\ \frac{S_\xi}{S_{\text{shot}}} \tag{4.18a}$$

$$= \int_B \mathrm{d}f\ n_s(f) + T\int_B \mathrm{d}f\ n_\xi(f) = \bar{N}_s + \bar{N}_\xi. \tag{4.18b}$$

The terms in (4.18) have the following interpretations. The photon number density $n_s(f)$ is the expected number of photons due to the signal detected per unit frequency and $n_\xi(f)$ is the expected number of photons due to noise detected per unit frequency per unit time. $\bar{N}_s$ and $\bar{N}_\xi$ are the total expected number of photons detected due to signal and noise, respectively. The number of photons N_γ actually detected is then Poisson distributed

$$P(N_\gamma) = \frac{(\bar{N}_s+\bar{N}_\xi)^{N_\gamma}}{N_\gamma!}\mathrm{e}^{-(\bar{N}_s+\bar{N}_\xi)}. \tag{4.19}$$

If we test the hypothesis that $\bar{N}_s$ is either zero or nonzero, as we did with the harmonic oscillator, the false alarm rate $1-\mathrm{e}^{-\bar{N}_\xi}$ becomes unacceptably large for noisy detectors. To deal with this, we can require detecting at least N_c photons before declaring a detection. Fig. 4.3 shows the necessary photon number cutoff as a function of noise for different false alarm rates. Note the discrete nature of this cutoff which is responsible for many of the jagged features in the examples below. In the context of photon counting, one is penalized for increasing the bandwidth B or the time of the measurement T by increasing the total number of noise photons $\bar{N}_\xi$ detected.

Finally, it is important to note that this analysis, and the benefits of photon counting, depends crucially on the state a being a coherent state. For example, suppose a is a squeezed state, as is often used in gravitational wave detectors and elsewhere to reduce

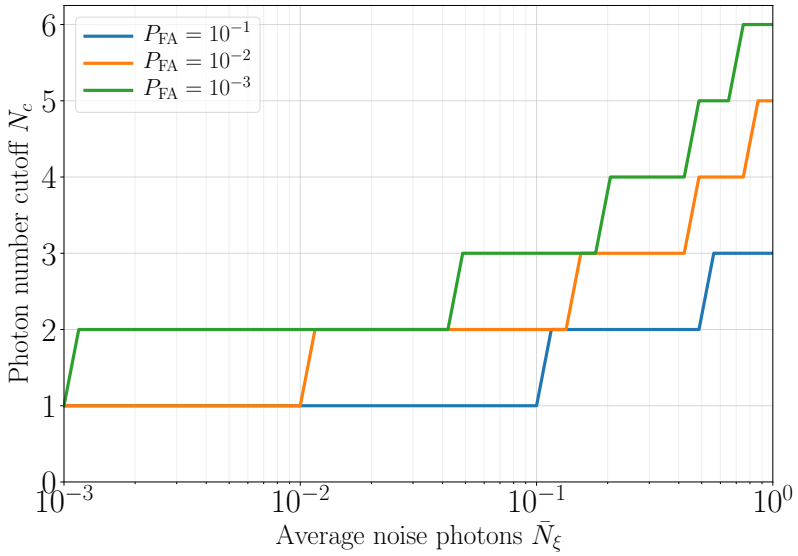

Figure 4.3: Minimum number of photons N_c required to claim a detection for different false alarm rates.

quantum noise. In this case, even in the absence of classical noise ($\bar{N}_\xi = 0$), there are photons in the absence of a signal: the probability distribution for the number of photons in the squeezed vacuum with squeeze factor r is [24]

$$P(N_\gamma) = \left(\frac{\tanh^{N_\gamma} r}{\cosh r}\right)^2. \tag{4.20}$$

The false alarm rate is now $1 - \cosh^{-2} r$ rather than 0.

4.3.2 Homodyne Detection

When doing homodyne detection we measure an infinite number of modes and we should consider how the signal is recorded and analyzed. As with the photon counting case, consider making the measurement for a signal lasting for time T sampled at a rate of Δt and analyze the part of the signal in a bandwidth B. We can measure the excess

power statistic defined as [48]

$$\mathcal{E} = 4 \sum_{k=Tf_{\min}}^{Tf_{\max}} \frac{|\alpha_k|^2}{S_{b,k}} \tag{4.21}$$

where α_k is the discrete Fourier transform of the signal

$$\alpha_k = \frac{1}{\Delta t}[s(k/T) + H_{\det}(k/T)\xi(k/T)] \tag{4.22}$$

and $S_{b,k}$ is the discrete noise spectral density, including both quantum and classical noise, of the b quadrature

$$S_{b,k} = \frac{T}{\Delta t^2} S_b(k/T) = \frac{T}{\Delta t^2}\left(S_a + \frac{S_\xi}{S_{\text{shot}}}\right) = \frac{T}{\Delta t^2}(1 + 2n_\xi). \tag{4.23}$$

The excess power, averaged over classical noise realizations, can thus be written as

$$\mathcal{E} = 4 \sum_{k=Tf_{\min}}^{Tf_{\max}} \left[\frac{1}{T}\frac{n_s(k/T)}{1 + 2n_\xi(k/T)} + \frac{n_\xi(k/T)}{1 + 2n_\xi(k/T)}\right] = \lambda_s + \lambda_\xi. \tag{4.24}$$

The excess power statistic is distributed as a noncentral χ^2 distribution with $\mathcal{N} = 2BT$ degrees of freedom

$$P(\mathcal{E}) = \frac{1}{2}\mathrm{e}^{-(\mathcal{E}+\lambda)/2}\left(\frac{\mathcal{E}}{\lambda}\right)^{\mathcal{N}/4-1/2} I_{\mathcal{N}/2-1}\left(\sqrt{\lambda\mathcal{E}}\right) \tag{4.25}$$

with noncentral parameter λ. As in the case of photon counting, we must choose a cutoff power $\mathcal{E}_c$ below which we will not claim a detection. In the context of homodyne detection, one is penalized for increasing the bandwidth B or the time of the measurement T by increasing the number of samples $\mathcal{N} = 2BT$.

4.3.3 Example Signal

To fully compare hypothesis testing with photon counting to hypothesis testing with homodyne detection, we need a model of a signal. To that end, consider a signal that, once filtered through the detector, is white noise

$$\langle s^*(f')s(f)\rangle = \frac{1}{2}\delta(f - f')S_s \tag{4.26}$$

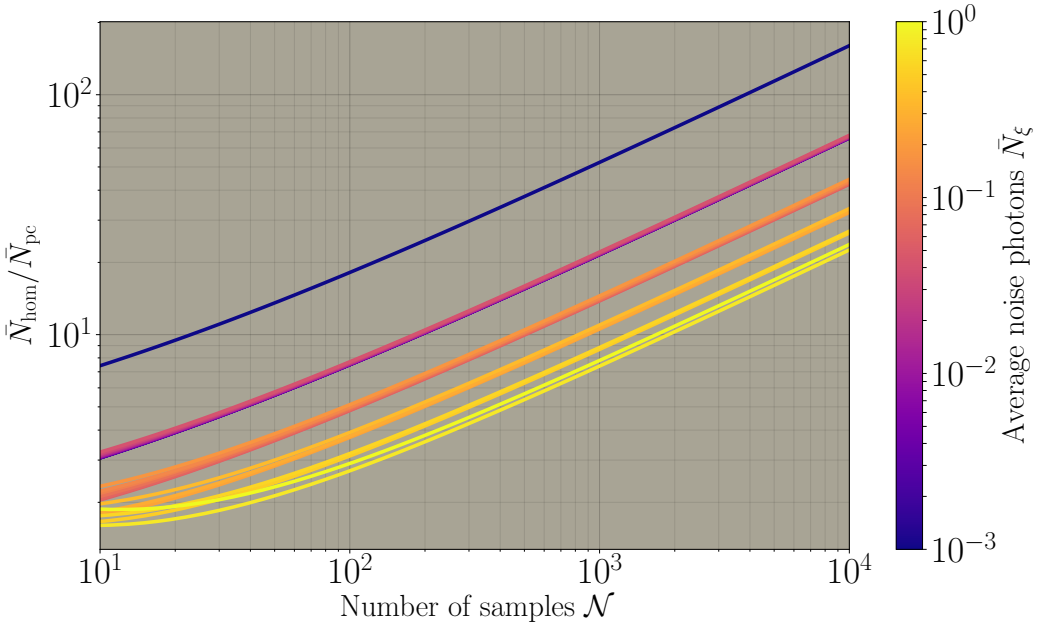

Figure 4.4: Ratio of the minimum detectable signal for hypothesis testing with homodyne detection to that for photon counting, i.e. the amount by which photon counting outperforms homodyne detection, as a function of the number of samples $\mathcal{N} = 2BT$ and average noise photons $\bar{N}_\xi$ using the model signal (4.26) for $P_{\rm FA} = 10^{-3}$ and $P_{\rm FD} = 0.5$.

where $S_s \equiv 2\alpha_s = 2n_s(f)/T$ is constant. (In the gravitational wave example below, we consider the case where the signal h is itself white.) Furthermore, we take the noise photon number density to be constant $n_\xi(f) = \alpha_\xi$. Plugging this into (4.18) gives

$$\bar{N} = BT(\alpha_s + \alpha_\xi) = \frac{\mathcal{N}}{2}(\alpha_s + \alpha_\xi) = \bar{N}_s + \bar{N}_\xi. \tag{4.27}$$

Since there are $\mathcal{N}/2$ terms in the sum in (4.24),

$$\mathcal{E} = \frac{\mathcal{N}}{2}\frac{4}{T}\frac{T(\alpha_s + \alpha_\xi)}{1 + 2\alpha_\xi} = \frac{4(\bar{N}_s + \bar{N}_\xi)}{1 + 4\bar{N}_\xi/\mathcal{N}} = \lambda_s + \lambda_\xi. \tag{4.28}$$

Now we want to compare the minimum detectable signal amplitude α_s for photon counting and homodyne detection. Let $\bar{N}_{\text{pc}}$ be the minimum number of signal photons required for a photon counting detection and λ_{hom} be the minimum non-central parameter λ_s necessary for a homodyne detection. The number of signal photons in a signal that would produce a non-central parameter λ_{hom} is, from (4.28),

$$\bar{N}_{\text{hom}} = \frac{\lambda_{\text{hom}}}{4}\left(1 + \frac{4\bar{N}_\xi}{\mathcal{N}}\right). \tag{4.29}$$

The amount by which hypothesis testing with photon counting outperforms that of homodyne detection is quantified by the ratio $\bar{N}_{\text{hom}}/\bar{N}_{\text{pc}}$, which is plotted in Fig. 4.4 as a function of $\mathcal{N}$ and $\bar{N}_\xi$.

To understand how this ratio scales with N_ξ, note that, to hold the total expected number of noise photons $\bar{N}_\xi$ constant as the duration and bandwidth of the measurement $\mathcal{N} = 2BT$ is varied, the noise density α_ξ is varied. Since the variance of the Poisson distribution of the number of noise photons is $\bar{N}_\xi$, the minimum number of signal photons necessary to claim a detection for photon counting is $\bar{N}_{\text{pc}} \sim \sqrt{\bar{N}_\xi}$. The minimum signal photons necessary to claim a detection for homodyne detection is set by $\mathcal{N}$. Thus, with $\mathcal{N}$ constant, $\bar{N}_{\text{hom}}/\bar{N}_{\text{pc}} \propto 1/\sqrt{\bar{N}_\xi}$. That photon counting does better than homodyne detection with decreasing classical noise can be understood intuitively since the false

alarm rate for photon counting goes to zero as $\bar{N}_\xi$ vanishes, as we saw with the harmonic oscillator example, while the false alarm rate for homodyne detection is set by the number of modes $\mathcal{N}$ measured independent of the amount of classical noise. Of course, the amount of classical effects the false dismissal rate for both methods, however.

To see how this ratio scales with $\mathcal{N}$, note that, since the excess power has a noncentral χ^2 distribution $\mathcal{E} \sim \chi^2_{\mathcal{N}}(\lambda)$, for $\mathcal{N} \gg 1$ it is normally distributed as $\mathcal{E} \sim \mathrm{N}[\mathcal{N}+\lambda, 2(\mathcal{N}+2\lambda)]$.[1] Therefore, for a signal to be detectable $\lambda_{\mathrm{hom}} \approx \sqrt{\mathcal{N}}$ for large $\mathcal{N}$. If $\bar{N}_\xi$ is constant, so is $\bar{N}_{\mathrm{pc}}$, and so $\bar{N}_{\mathrm{hom}}/\bar{N}_{\mathrm{pc}} \propto \sqrt{\mathcal{N}}$.

When the classical noise is larger than the time-frequency product $\bar{N}_\xi \gtrsim \mathcal{N}$, $\bar{N}_{\mathrm{hom}}/\bar{N}_{\mathrm{pc}}$ for decreases with increasing $\mathcal{N}$ before increasing as $\sqrt{\mathcal{N}}$. This is explained by the conversion, Eqs. (4.28) and (4.29), between λ_{hom} and $\bar{N}_{\mathrm{hom}}$: when the classical noise is large, $\bar{N}_\xi \gtrsim \mathcal{N}$, the number of signal photons $\bar{N}_s$ necessary to reach a given λ increases.

4.4 Combining Multiple Measurements

We have described how hypothesis testing can be used to test whether a signal is present in a measurement. If multiple measurements of processes with possible signals are made, these measurements can be combined to test whether any of them contained a signal.

First, consider two measurements with signals s_1 and s_2. If photons were counted, suppose that the first measurement observes N_1 and the second observes N_2 photons. If instead a homodyne measurement was made, suppose an excess power of $\mathcal{E}_1$ was observed with $\mathcal{N}_1$ samples for the first measurement and an excess power $\mathcal{E}_2$ observed with $\mathcal{N}_2$ samples for the second. We can now compute the total number of photons $N_{\mathrm{tot}} = N_1 + N_2$

[1] The notation $X \sim D$ means, "The random variable X has the distribution D." The normal distribution with mean μ and variance σ^2 is denoted by $\mathrm{N}(\mu, \sigma^2)$, the Poisson distribution with mean (and variance) $\bar{N}$ is denoted by $\mathrm{Pois}(\bar{N})$, and the noncentral χ^2 distribution with $\mathcal{N}$ degrees of freedom and noncentral parameter λ is denoted by $\chi^2_{\mathcal{N}}(\lambda)$.

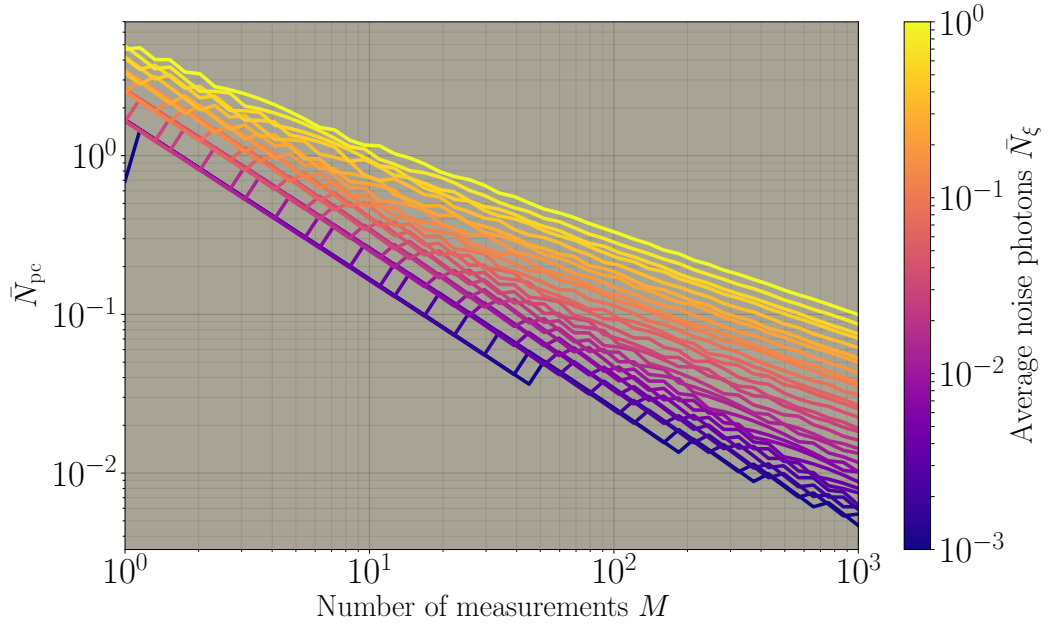

Figure 4.5: Scaling of the minimum number of signal photons for the example signal (4.26) for hypothesis testing by photon counting as a function of the number of identical measurements made.

observed over both measurements or the total excess power $\mathcal{E}_{\rm tot} = \mathcal{E}_1 + \mathcal{E}_2$. In this, case the $N_{\rm tot}$ is again Poisson distributed with mean $\bar{N}_1 + \bar{N}_2$

$$N_{\rm tot} \sim \text{Pois}(\bar{N}_1 + \bar{N}_2) \tag{4.30}$$

and $\mathcal{E}_{\rm tot}$ is again distributed as a non-central χ^2 distribution

$$\mathcal{E}_{\rm tot} \sim \chi^2_{\mathcal{N}_1+\mathcal{N}_2}(\lambda_1 + \lambda_2). \tag{4.31}$$

If we now consider M measurements of the same signal, the total number of photons $N_{\rm tot}$ and total excess power $\mathcal{E}_{\rm tot}$ are distributed as

$$N_{\rm tot} \sim \text{Pois}(M\bar{N}), \qquad \mathcal{E}_{\rm tot} \sim \chi^2_{M\mathcal{N}}(M\lambda). \tag{4.32}$$

For many measurements $M \gg 1$, both are approximated by normal distributions:

$$N_{\text{tot}} \sim \text{N}(M\bar{N}, M\bar{N}) \tag{4.33}$$

$$\mathcal{E}_{\text{tot}} \sim \text{N}[M(\lambda + \mathcal{N}), 2M(\mathcal{N} + 2\lambda)]. \tag{4.34}$$

This means that, for large M, both the total number of photons $\mathcal{N}_{\text{tot}}$ and the total excess $\mathcal{E}_{\text{tot}}$ power necessary to claim a detection scale as $\sqrt{M}$. Therefore, the minimum detectable signals for an individual signal for both methods scale as $\sqrt{M}/M = 1/\sqrt{M}$.

The situation is actually better for photon counting if the noise $\bar{N}_\xi$ is small. As $\bar{N}_\xi$ becomes much less than M, the minimum number of signal photons becomes constant. Therefore, the minimum signal for a single measurement scales as $1/M$ instead of $1/\sqrt{M}$. Fig. 4.5 shows how $\bar{N}_{\text{pc}}$ for the example signal (4.26) discussed above depends on the number of measurements M.

4.5 Application to Tests of General Relativity through Gravitational Wave Detection

In this section we discuss how hypothesis testing with photon counting and homodyne detection can be used to search for deviations from general relativity in observations of gravitational waves. To apply the formalism developed above, where the null hypothesis $\mathcal{H}_0$ is that no signal is present (i.e. no deviation from GR) and the alternate hypothesis $\mathcal{H}_1$ is that a signal exists (i.e. there is a deviation from GR), the GR prediction must be subtracted from the measured data.

To do so in practice, the inspiral of a gravitational wave would be used to estimate the parameters of the source. With space detectors, signals can be studied for months to years before entering the ground network bands and the parameters can thus be determined very accurately. Some sources may also stay in the low frequency band of

future gravitational wave detectors long enough to estimate the parameters of the source from the ground alone. These parameters would then be used to generate a numerical relativity waveform for the GR prediction, and this waveform would be used to actuate on the interferometer mirrors in such a way as to cancel the expected signal. Any signal detected after this subtraction would thus be evidence for a deviation from GR.

In interferometric gravitational wave detectors at low frequencies, radiation pressure causes the output signal to be in a squeezed state. As discussed above, photon counting is not useful in such a case. However, at higher frequencies, the signal is dominated by shotnoise and the output is in a coherent state. In a standard configuration of such interferometers, the output has the form of a low pass filter [35, 36]

$$H_{\rm det}(f) = \frac{g e^{-2\pi i f L/c}}{1 + i f/f_p}, \tag{4.35}$$

where L is the length of the arms, f_p is the cavity pole frequency, and g is the optical gain. For the remainder of this section we take numbers characteristic of the LIGO Voyager design [8], for which $L = 4$ km, $f_p \approx 250$ Hz, and $g \approx 10^{24}\ \sqrt{\text{photons/Hz}}/(\text{strain/Hz})$. At frequencies above the cavity pole, where shotnoise dominates and we would want to do photon counting, the dominant source of classical noise is coating thermal noise which scales as $S_\xi \propto 1/f$. The noise photon number density is thus

$$n_\xi = \frac{1}{2}\frac{S_\xi}{S_{\rm shot}} = \frac{1}{2}|H_{\rm det}|^2 S_\xi = \frac{k}{(f/f_p)[1 + (f/f_p)^2]}. \tag{4.36}$$

For Voyager parameters, $k \approx 0.2\,\text{photons/s/Hz}$.

4.5.1 Example GR Modification

Now consider a gravitational wave signal with a modification to general relativity of the form

$$h = h_{\rm GR} + \Delta h \tag{4.37}$$

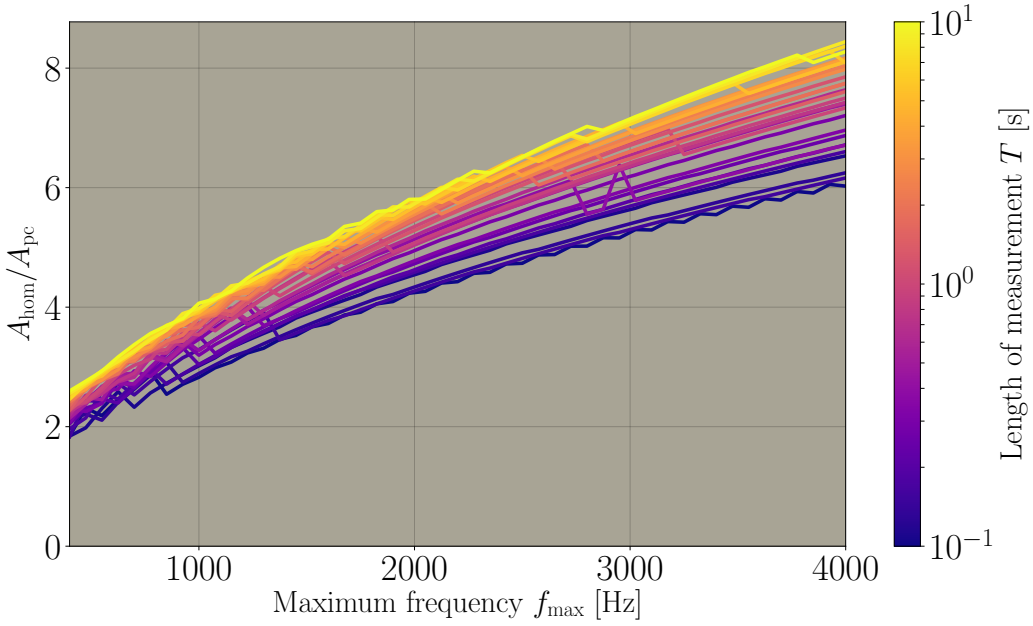

Figure 4.6: Ratio of the minimum detectable deviation from GR for hypothesis testing with homodyne detection to that of photon counting for the deviation (4.37) and (4.38)

where h_{GR} is the waveform predicted by general relativity and Δh is the deviation. We want to compare how large of a deviation Δh from GR is necessary before it can be detected by performing hypothesis tests with photon counting and homodyne detection.

As a simple example of a deviation from GR, suppose that the signal is modified by white noise with spectral density $S_{\Delta h} = A$, i.e.

$$\langle \Delta h^*(f')\Delta h(f)\rangle = \frac{1}{2}\delta(f-f')A. \tag{4.38}$$

The signal noise photon density is thus $n_s = TA/2S_{\text{shot}}$. The average number of signal photons is thus

$$\begin{aligned}\bar{N}_s &= \frac{TA}{2}\int_{f_{\text{min}}}^{f_{\text{max}}} \frac{g^2}{1+(f/f_p)^2}\,\mathrm{d}f \\ &= \frac{1}{2}TAg^2 f_p\left(\arctan\frac{f_{\text{max}}}{f_p} - \arctan\frac{f_{\text{min}}}{f_p}\right),\end{aligned} \tag{4.39}$$

and the average number of noise photons is

$$\begin{aligned}\bar{N}_\xi &= T\int_{f_{\min}}^{f_{\max}} \frac{k}{(f/f_p)[1+(f/f_p)^2]}\,\mathrm{d}f \\ &= Tkf_p \ln\left[\frac{f_{\max}}{f_{\min}}\sqrt{\frac{1+(f_{\min}/f_p)^2}{1+(f_{\max}/f_p)^2}}\right],\end{aligned} \tag{4.40}$$

For homodyne detection, the contribution to the noncentral parameter from the signal and noise are

$$\lambda_s = 2A\sum_{k=Tf_{\min}}^{Tf_{\max}} \frac{|H|^2}{1+2n_\xi} \tag{4.41}$$

$$\lambda_\xi = 4\sum_{k=Tf_{\min}}^{Tf_{\max}} \frac{n_\xi}{1+2n_\xi} \tag{4.42}$$

where H is given by (4.35) and n_ξ is given by (4.36).

The ratio of the minimum detectable deviation when performing hypothesis testing with homodyne detection A_{hom} to the minimum detectable deviation for photon counting A_{pc} is shown in Fig. 4.6. To see how the noise behaves when the duration and bandwidth of the measurement are changed, the minimum frequency is set at $f_{\min} = 300\,\mathrm{Hz}$ as $f_{\max}$ and T are varied. For photon counting, since both $\bar{N}_s$ and $\bar{N}_\xi$ are proportional to T, $A_{\mathrm{pc}} \propto 1/\sqrt{T}$. As the bandwidth increases, A_{pc} decreases initially since both more signal and more noise photons are detected; however, since both the detector response decreases like $|H|^2 \propto (f/f_p)^{-2}$ and the noise photon number density decreases like $n_\xi \propto (f/f_p)^{-3}$ for frequencies $f \gg f_p \approx 250\,\mathrm{Hz}$, further increase of the bandwidth leads to no further detection of either signal or noise photons. Therefore, once $f_{\max} \approx 600\,\mathrm{Hz}$, further increase of the bandwidth has no effect on the minimum detectable deviation.

The situation is worse for homodyne detection. Since increasing T increases both the magnitude of the excess power and the number of samples $\mathcal{N} = 2BT$, the minimum detectable signal also scales as $A_{\mathrm{hom}} \propto 1/\sqrt{T}$. As for photon counting, since the detector acts like a low-pass filter, no extra signal is detected by increasing the bandwidth past

$f_{\rm max} \approx 600\,{\rm Hz}$. However, homodyne detection always suffers from increasing the number of samples: $\mathcal{N} \propto f_{\rm max}$. Thus, $A_{\rm hom} \propto \sqrt{f_{\rm min}}$ after $f_{\rm max} \gtrsim 600\,{\rm Hz}$. The ratio of the minimum detectable signals thus scale as $A_{\rm hom}/A_{\rm pc} \propto \sqrt{f_{\rm max}}$ for large $f_{\rm max}$ and $A_{\rm hom}/A_{\rm pc}$ asymptotes to a constant ratio as T is increased.

Finally note that, if M measurements are combined to search for deviations, based on the general considerations described above, both $A_{\rm hom} \propto 1/\sqrt{M}$ and $A_{\rm pc} \propto 1/\sqrt{M}$.

4.5.2 Technical Sources of Photon Noise

When using hypothesis testing to look for deviations from general relativity, there are several sources of noise. First, there is the fundamental and technical noise of the detector itself. Ground-based interferometric detectors will be shot noise limited $S_\xi/S_{\rm shot} < 1$ above a few hundred Hz. In this regime, the largest source of classical noise is coating thermal noise, as discussed above. Second, losses in the interferometer, including imperfect photodiode quantum efficiency, increase the minimum detectable signal.

Third, the arms of an interferometer are not perfectly balanced. This results in some light leaking out of the interferometer even in the absence of a signal. This contrast defect will need to be removed before photons can be counted.

Finally, there is noise coming from imperfect subtraction of the waveform expected from general relativity under the null hypothesis. To make the subtraction, the parameters of the source must be known precisely; any uncertainties in these parameters are a source of noise. Furthermore, even with perfectly known parameters from the source, the deviations of the numerical relativity waveforms from the exact predictions of general relativity will result in imperfect waveform subtraction. Finally, errors in the actuation of the interferometer mirrors to cancel the expected signal will result in imperfect subtraction as well.

4.6 Conclusions

When deciding between the two hypotheses that there is vs. there is not a signal present in a coherent state of the electromagnetic field, we can either measure that field directly (homodyne detection) or can count photons in the field. Measuring the signal requires a local oscillator which adds quantum noise to the measurement through its beating with vacuum fluctuations. Photon counting does not suffer from vacuum fluctuations.

When looking for signals, one must limit the search to a certain time-frequency region. Increasing the size of this region increases the amount of signal that could be detected, but it also increases the noise in both methods. For photon counting the increased noise comes only from classical noise in the detection process: the larger the time-frequency region the more classical noise photons will be detected. Increasing the time-frequency region increases the number of modes a homodyne detection has to search and thus decreases the statistical significance of a given signal due to the multiple hypothesis testing.

We have shown in two examples that photon counting allows one to detect a weaker signal than homodyne detection. Furthermore, the extent to which photon counting surpasses homodyne detection increases as the classical noise in the detector becomes much less than the quantum noise $S_\xi/S_{\rm shot} \ll 1$: the probability of photon counting making a mistake decreases as the number of noise photons decreases.

The kind of hypothesis testing described here can, in principal, be used to search for deviations from general relativity in measurements of gravitational waves with interferometric gravitational wave detectors; however, many technical challenges remain to reduce the classical noise to acceptable levels.

Chapter 5

TianGO: A Space Interferometer Between the LISA and LIGO Bands

This chapter describes the TianGO space detector briefly mentioned in the introduction. Sec. 5.1 explains why using space interferometers, and TianGO in particular, is useful. Sec. 5.2 introduces some difficulties of space missions that do not exist for the terrestrial interferometers and explains how LISA addresses them. Sec. 5.3 explains the preliminary TianGO design, and Sec. 5.4 gives the noise budget. Future work is discussed in Sec. 5.5.

5.1 Why Space?

Ground detectors are limited by seismic noise at low frequencies, so one needs to put detectors in space to escape this noise. Furthermore, the sensitivity to gravitational waves is proportional to the arm length and it is easier to make long arms in space and thus to increase the sensitivity to gravitational waves.

A space detector can also localize source locations extremely accurately. When combined with a network of ground detectors, the long baseline between the space detector and the ground network allows for good triangulation. For sources that last for significant fractions of an orbit, as many signals detected by space detectors do, the large area that the detector sweeps out in it's orbit provides a long baseline with the space

detector itself. Furthermore, the modulation of the signal by the time dependence of the detector antenna patterns and the Doppler shifts imposed on the waveform by the detector's motion in its orbit help to localize the source [49].

As an example of TianGO's sky localization ability, consider the case of GW170817, the first binary neutron star observed with gravitational waves [4]. This binary had a chirp mass of $\mathcal{M} = 1.2\,M_\odot$ and a luminosity distance of $D_L = 40\,\mathrm{Mpc}$. The gravitational wave detector network was able to localize the source to a $28\,\mathrm{deg}^2$ region of the sky. TianGO would have seen the source long before it entered the ground detector band. It would take about 5 years to sweep through the band from 100 mHz to 160 mHz, during which time TianGO would detect it with a squared SNR of roughly $\rho^2 = 220$. As a rough estimate of TianGO's ability to estimate the source location over this time, one can use the geometric estimate from Ref. [50]. For an optimally oriented source, the angular uncertainty in the localization is

$$\Delta\Omega = \frac{c^2}{f^2\rho^2\pi R^2}, \tag{5.1}$$

where $R = 1\,\mathrm{AU}$ is the radius of TianGO's orbit around the sun. For GW170817, this is of order $10^{-3}\,\mathrm{deg}^2$ for TianGO.

With this ability to localize sources, space detectors can also give early warnings for both terrestrial gravitational wave detectors and, especially, for electromagnetic telescopes so that they know where and when to point to observe the electromagnetic counterparts to gravitational wave signals [51, 52].

The ability to point electromagnetic telescopes to sources of gravitational waves is especially useful for resolving the current tension between the two types of measurements of the Hubble constant [53–55]. One makes local measurements and relies on the astrophysics of stars to calibrate standard candles that can then be used to measure cosmological distances. The second fits observations of the CMB to models of the early

universe. These two types of measurements now disagree at the 3σ level.

Measurements of a gravitational wave signal from compact binary system provides an accurate estimate of the distance to the source but does not determine the redshift. If the host galaxy can also be identified, however, the redshift can be measured independently with electromagnetic telescopes. Combining the optical and gravitational observations thus provides a measurement of the Hubble constant [56–59]. It is possible to identify the host galaxy if the gravitational wave signal is accompanied by an optical counterpart, however this is not always the case. TianGO can be used to identify the measure the Hubble constant without an optical counterpart by combining its sky localization ability with statistical methods of extracting redshifts from clusters of galaxies [60].

5.2 TianGO is not Like LISA

There are many aspects of the TianGO design that can be borrowed from LISA, however the principle of operation is quite different. In this section we describe some unique aspects of interferometry in space and the way that LISA addresses them. The design of TianGO is described in Sec. 5.3.

The LISA detector is a set of three (not independent) interferometers in space. It consists of three spacecraft that form an equilateral triangle with 2×10^6 km long arms. Each spacecraft serves as the corner of one of the three interferometers with the links to the other two spacecraft forming the arms. Instead of the mirrors that serve as the test masses in terrestrial detectors, LISA uses cubes, known as proof masses, made out of an alloy of gold and platinum [14, 61–63]. Each spacecraft has two proof masses, one for each interferometer arm. Since it is the distance between the proof masses that is monitored to search for gravitational waves, the masses should be kept as inertial as possible. To accomplish this, the proof masses are not attached to the spacecraft.

Instead, in a technique known as drag-free flight, the spacecraft sense the position of the proof mass and fly around to follow their motion. TianGO will use drag-free flight as well, but the proof masses will be mirrors like are used for ground detectors.

TianGO is most similar to LISA in its orbit around the sun. The three spacecraft LISA constellation orbits the sun in an orbit trailing the Earth by 20°. Each spacecraft is in its own elliptical orbit around the sun and the plane of the constellation is tilted 60° with respect to the ecliptic plane. The orbits are arranged so that the triangular constellation tumbles as it advances in its orbit [64–68]. This rotation increases the angular resolution of the detector [49].

Due to the eccentricity of the orbits and gravitational perturbations from the Earth and other planets, the spacecraft move relative to one another throughout the orbits, and so the arms of the interferometers are not constant. Fig. 5.1 shows the arm length change for a LISA-like orbit that TianGO could use. These changing orbits leads to Doppler shifts in the lasers traveling between two spacecraft as is also shown in Fig. 5.1. The magnitude of the Doppler shifts increase linearly with increasing arm length. Since it is a gravitational force gradient between the Earth and the satellites that is mostly responsible for the arm length change, the Doppler shifts decrease as the cube of the distance from the Earth. For the LISA orbit trailing the Earth by 20° and with 2×10^6 km armts, the Doppler shifts can be around 10 MHz [14].

Another difficulty LISA faces is that the diffraction of the laser beams along its 2×10^6 km long arms results in only about 100 pW of power being received at the far spacecraft [14, 61]. This is far too little power to reflect back to the first spacecraft as is done with traditional interferometry. Since it is not possible to use a simple Michelson interferometer, each arm of the LISA interferometer consists of two laser links. The light from one spacecraft is received at the far spacecraft where it is phase-locked to a second laser on that spacecraft. This phase-locked light is then sent back to the first spacecraft.

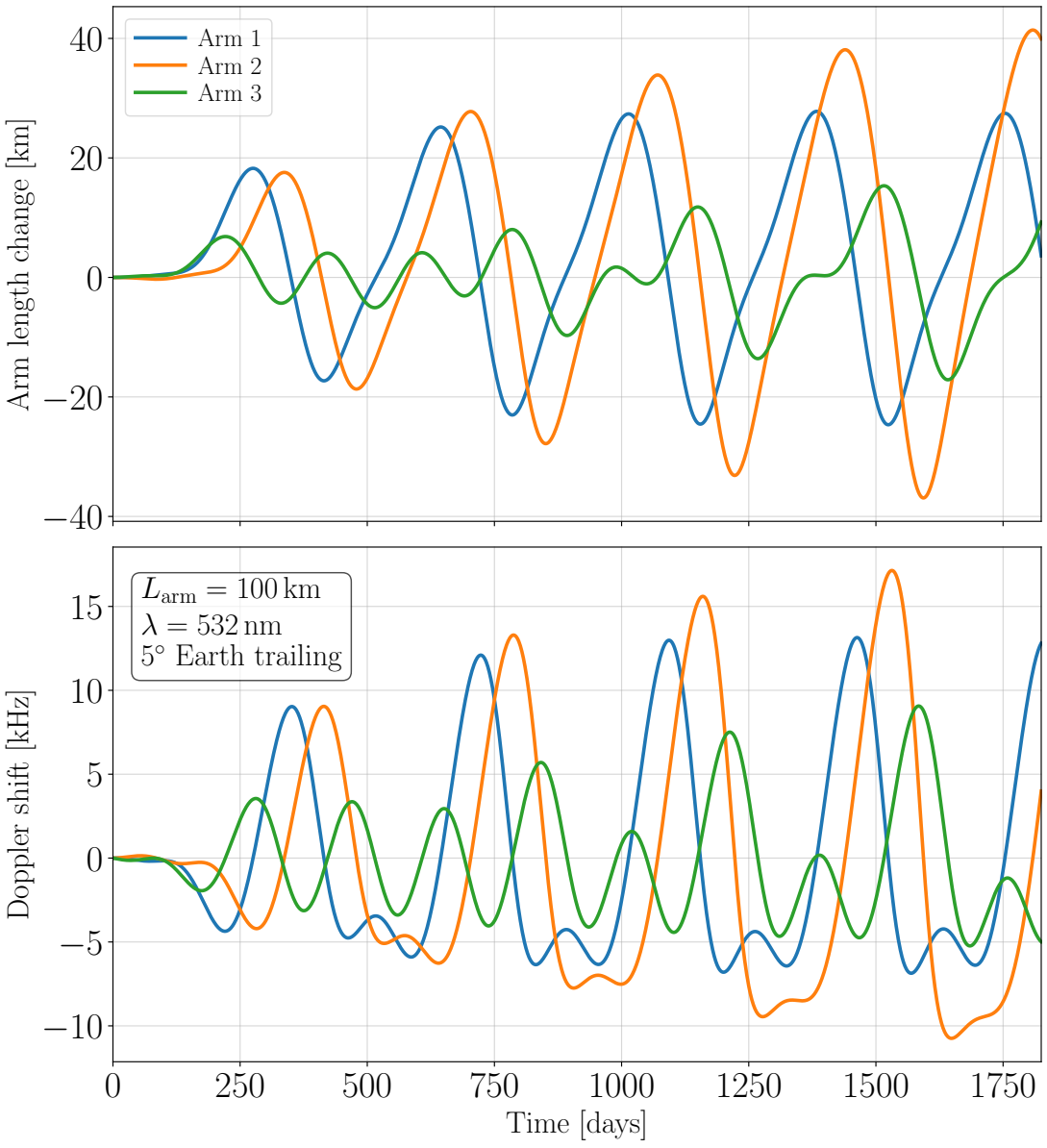

Figure 5.1: Arm length change and Doppler shifts of an uncontrolled TianGO orbit

The phase meter is designed to have enough dynamic range that it can track the phase on top of the Doppler shifts arising from the changing arm lengths.

A final difficulty arising from the changing arm lengths is susceptibility to laser noise. In traditional interferometers with equal arm lengths, noise from the laser is common to both arms and is canceled when recombined at the beam splitter, but LISA does not benefit from this common mode suppression. Instead, using a method known as time-delay interferometry (TDI) [69–71], the time-series of the phase measurements from each link of the interferometer are shifted and recombined in combinations that suppress the laser noise during post-processing.

5.3 TianGO Design

Fig. 5.2 shows an overview of the TianGO detector. It is comprised of three spacecraft that form a triangular constellation with 100 km long arms. Since the arms are short enough that a Gaussian beam can be sent between two spacecraft with less than 1% loss, TianGO operates as a simple Michelson interferometer. One spacecraft, the corner spacecraft, houses a laser and a beam splitter. Just as with terrestrial interferometric gravitational wave detectors, the laser is split at the beam splitter with half the light going to each spacecraft. Each of the other two spacecraft have mirrors that simply reflect the light back to the corner spacecraft where it is recombined at the beam splitter. To reduce quantum shot noise, TianGO will also employ 10 dB of phase squeezing.

The beam splitter in the corner spacecraft and the mirrors in the end spacecraft are under drag-free flight, as is done for the LISA proof masses. Sapphire and fused silica are being considered to be the proof mass substrates. The mirrors will be 10 kg.

The following sections describe aspects of the TianGO design in more detail. Sec. 5.3.1 describes TianGO's input and output optics in more detail. The TianGO telescopes are

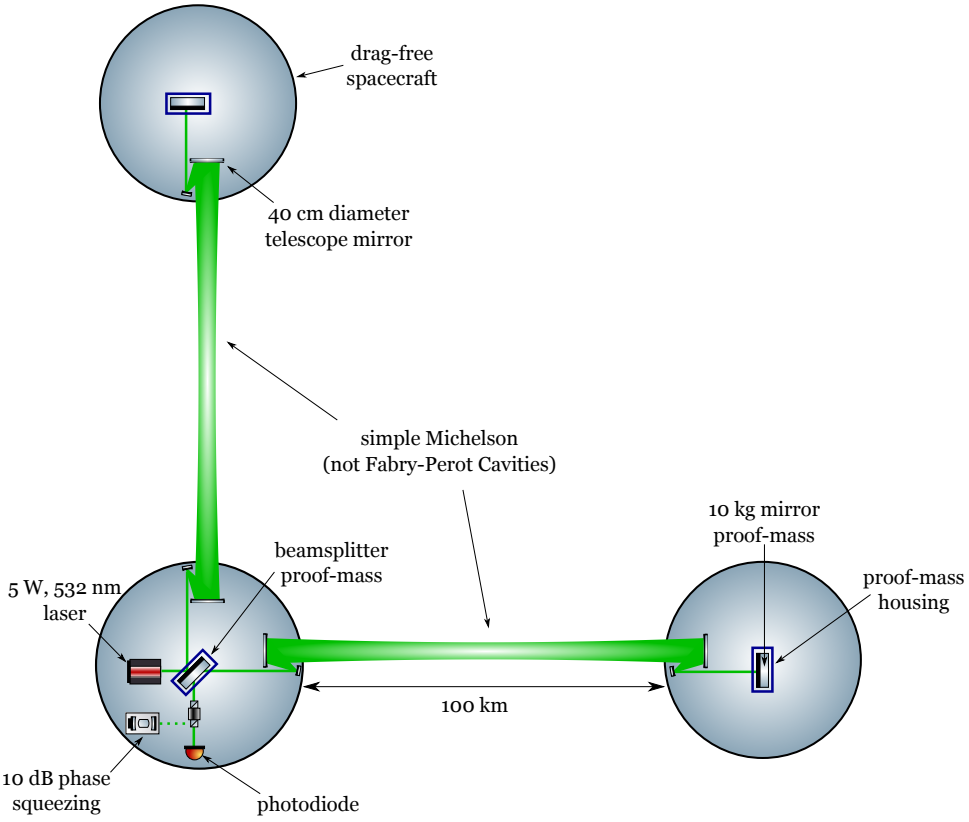

Figure 5.2: Overview of the TianGO detector

discussed in Sec. 5.3.2 and a basic control system for controlling the proof masses is described in Sec. 5.3.3.

5.3.1 Optics

TianGO will use a 5 W laser with a wavelength of $\lambda_0 = 532\,\mathrm{nm}$. As is discussed in Sec. 5.4 and shown in Fig. 5.6, the goal is to have a strain sensitivity of about $S_h^{1/2} = 10^{-22}/\sqrt{\mathrm{Hz}}$ at 1 Hz. Unlike LISA, TianGO benefits from the common mode rejection of a Michelson interferometer. If the difference in the lengths of the arms of the interferometer are ΔL, the equivalent displacement noise caused by laser frequency noise $S_\nu^{1/2}$ is $S_x^{1/2}/\Delta L = S_\nu^{1/2}/\nu_0$. So that the laser frequency noise is no larger than one-tenth the sensitivity goal of $10^{-22}/\sqrt{\mathrm{Hz}}$, this sets the requirement on the frequency noise of the laser to be

$$S_\nu^{1/2} < \frac{c}{\lambda_0}\frac{L}{\Delta L}\frac{S_h^{1/2}}{10} = 5.6\times 10^{-4}\frac{\mathrm{Hz}}{\sqrt{\mathrm{Hz}}}\left(\frac{1\,\mathrm{m}}{\Delta L}\right) \tag{5.2}$$

at 1 Hz. To keep the interferometer in the linear regime, ΔL should be no larger than roughly 1% of a wavelength, which sets the fairly easy requirement that $S_\nu^{1/2} < 100\,\mathrm{kHz}/\sqrt{\mathrm{Hz}}$.

The laser will first be stabilization with an unequal arm-length Mach-Zehnder interferometer. Ref. [72] demonstrated frequency stabilization down to 100 $\mathrm{Hz}/\sqrt{Hz}$ at 1 Hz with such an interferometer suitable for satellite flight. Alternatively, the laser could be locked to a reference cavity with PDH locking [73, 74] as is done with the LIGO pre-stabilized lasers [75]. Ref. [76] demonstrated stabilization to roughly $50\,\mathrm{mHz}/\sqrt{Hz}$ at 1 Hz with ultrastable reference cavities.

After frequency stabilization, the light is sent through a four mirror cavity known as the input mode cleaner (IMC). The IMC reduces the higher-order mode content from the input light since only the fundamental mode resonates in the cavity. The transmission

of light through the IMC is also sensed and used for intensity stabilization of the light as is done with the LIGO pre-stabilized laser [75]. The beam is sent through a Faraday isolator before going to te beam splitter to prevent light from the interferometer being reflected back towards the laser.

To reduce quantum shot noise, 10 dB of phase squeezed vacuum is injected into the asymmetric port of the interferometer through the output Faraday isolator. Research towards compact squeezed light sources using nonlinear waveguides is currently underway [77]. TianGO will use some of the stabilized light as a seed for such a waveguide squeezer. The coherent locking technique [78, 79] will be used to control the squeeze angle.

Another bowtie cavity at the asymmetric port, the output mode cleaner (OMC), filters out higher order modes and the coherent locking field before the signal is sensed with a balanced homodyne detector.

5.3.2 Telescope

Each spacecraft uses telescopes to expand the radius of the laser beams so that they can be sent between the spacecraft without appreciable dispersion. The radius of a Gaussian beam is [80]

$$w(z) = w_0\sqrt{1+(z/z_R)^2}, \qquad z_R = \frac{\pi w_0^2}{\lambda} \tag{5.3}$$

where w_0 is the radius of the beam waist and z is the distance along the beam from the waist. The Rayleigh range z_R is the distance from the waist over which Gaussian beams are well collimated. The intensity of a beam of power P a radial distance R from the beam axis is $(2P/\pi w^2)\mathrm{e}^{-2R^2/w^2}$ [80]. Therefore, if light of power P_{trans} is transmitted, the light received from a mirror of diameter D is

$$P_{\mathrm{rec}} = \left(1-\mathrm{e}^{-D^2/2w^2}\right)P_{\mathrm{trans}}. \tag{5.4}$$

To minimize the dispersion of a beam propagating between two mirrors a distance L apart, the waist should be located halfway between them. The power transmitted between two such mirrors is maximized by choosing

$$w_0 = \sqrt{\frac{\lambda L}{2\pi}}. \tag{5.5}$$

With this choice, the radius of curvature of the beams at the mirrors is L.

The TianGO telescopes are designed to have a diameter of 40 cm which results in a clipping loss of 0.9%. The g factor of the cavity formed between two telescopes with radii of curvature $R_{\rm tel}$ is $g = 1 - L/R_{\rm tel}$ and should satisfy $0 < g^2 < 1$ for the cavity to be stable [80]. The radii of curvature of the TianGO telescopes are therefore made slightly larger than L.

The possibility of eliminating separate telescopes and proof mass mirrors for the corner spacecraft and instead using the proof masses directly as their own telescopes warrants further study. The materials currently being considered for the proof masses have densities of $2 \times 10^3\,\mathrm{kg/m^3}$ for fused silica and $4 \times 10^3\,\mathrm{kg/m^3}$ for sapphire. Thus, for the proof masses to reach the 10 kg design goal, the mirrors need to have fairly large diameters of roughly 15–20 cm. If these proof masses can serve to directly reflect the light to the corner spacecraft, they would need to have diameters of 40 cm, which would increase their mass by a factor of roughly 5–10, thus reducing radiation pressure noise by the same amount. However, in addition to the engineering challenges, difficulties with residual gas noise, discussed below in Sec. 5.4.1, suggest that this may be difficult.

The TianGO sensitivity can be improved if the arm lengths are increased. However, doing so is impractical due to the beam divergence: increasing the arm length to 1000 km would result in a beam radius of about 40 cm on the spacecraft mirrors. Making mirrors big enough to reduce clipping loss to less than 1% is unrealistic with current technology. First, the mirrors have to fit inside a rocket to be launched into space. Second, larger,

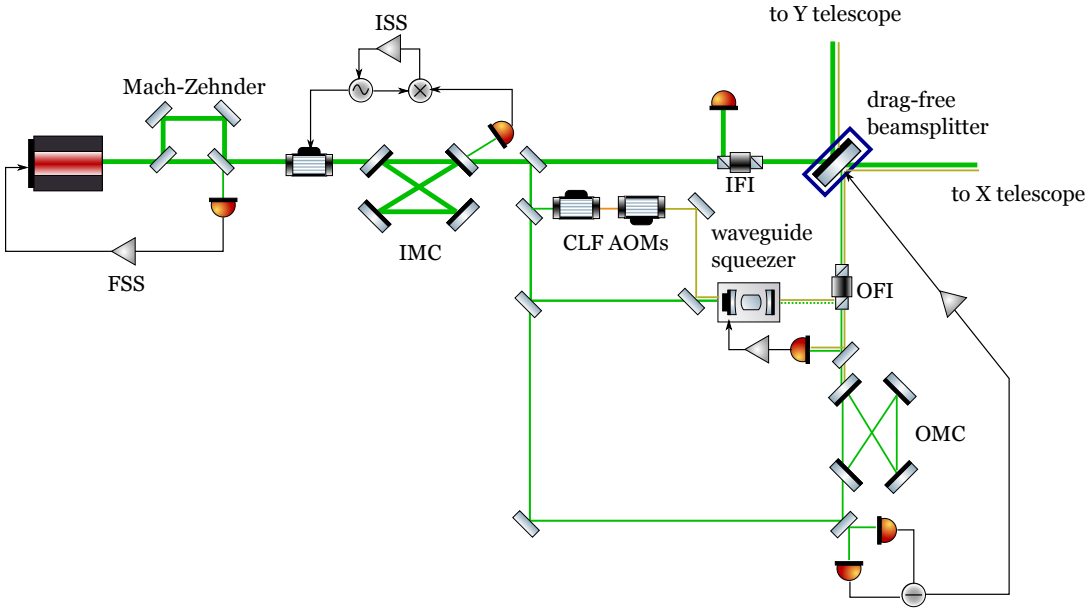

Figure 5.3: Details of the TianGO corner satellite. The following acronyms are described in the text. IMC: input mode cleaner; OMC: output mode cleaner; FSS: frequency stabilization servo; ISS: intensity stabilization servo; IFI: input Faraday isolator; OFI: output Faraday isolator; CLF AOMs: coherent locking field acousto-optic modulators.

and therefore more massive, mirrors are more costly in terms of rocket fuel to get into their final orbits. However, methods of making lightweight foldable telescope mirrors are currently being investigated [81–85]. If this technology matures enough, a hypothetical advanced TianGO (aTianGO) could improve on TianGO's strain sensitivity by a factor of 10 by employing 1.5 m diameter telescope mirrors with 1000 km long arms.

5.3.3 Control System

A diagram of the control loop for one of the proof masses is shown in Fig. 5.4. The proof mass and spacecraft plants, from force to position, are $P_{\rm pm} = 1/M_{\rm pm}\Omega^2$ and $P_{\rm sc} = 1/M_{\rm sc}\Omega^2$, respectively, where $M_{\rm pm}$ and $M_{\rm sc}$ are the masses of the proof mass and spacecraft. A position sensor $D_{\rm pm}$ measures the distance between the proof mass and spacecraft and feeds the signal back to the proof mass and spacecraft controllers $C_{\rm pm}$

and $C_{\rm sc}$. The resulting control signals are used to actuate on the proof mass with the actuators A and on the spacecraft with the thrusters T. Displacement noise from the position sensor enters in n_d and external forces act on the proof mass and spacecraft at $f_{\rm pm}$ and $f_{\rm sc}$. A feedforward signal r is used to suppress relative motion between two proof masses in different spacecraft due to the uncontrolled breathing of the orbits.

Newtonian gravity gradients and position dependent forces from the position sensors and actuators produce a spring-like coupling $k_{\rm sc}$ between the proof mass and spacecraft: $M_{\rm pm}a_{\rm pm} = k_{\rm sc}\Delta x$ and $M_{\rm sc}a_{\rm sc} = -k_{\rm sc}\Delta x$ where $\Delta x = x_{\rm pm} - x_{\rm sc}$. It is useful to define the spring frequency $\omega_{\rm sc}^2 = k_{\rm sc}/M_{\rm PM}$ and the dimensionless couplings $\Gamma_{\rm pm}$ and $\Gamma_{\rm sc}$ as

$$\omega_{\rm sc}^2 = \frac{k_{\rm sc}}{M_{\rm sc}}, \qquad \Gamma_{\rm pm} = P_{\rm pm}k_{\rm sc} = \frac{\omega_{\rm sc}^2}{\Omega^2}, \qquad \Gamma_{\rm sc} = -P_{\rm sc}k_{\rm sc} = -\frac{M_{\rm pm}}{M_{\rm sc}}\frac{\omega_{\rm sc}^2}{\Omega^2}. \tag{5.6}$$

Backaction forces from the position sensors and actuators are part of the forces $f_{\rm pm}$ and $f_{\rm sc}$.

If we define the open-loop transfer functions for the proof mass and spacecraft as

$$H_{\rm pm} = AP_{\rm pm}D_{\rm pm}C_{\rm pm}, \qquad H_{\rm sc} = TP_{\rm sc}D_{\rm sc}C_{\rm sc}, \tag{5.7}$$

the closed-loop position of the proof mass is

$$\begin{aligned} x_{\rm sc} = &\frac{1 + \Gamma_{\rm sc} - H_{\rm sc}}{1 + H_{\rm pm} - \Gamma_{\rm pm} - H_{\rm sc} + \Gamma_{\rm sc}}P_{\rm pm}a_{\rm pm} \\ &+ \frac{H_{\rm pm} - \Gamma_{\rm pm}}{1 + H_{\rm pm} - \Gamma_{\rm pm} - H_{\rm sc} + \Gamma_{\rm sc}}P_{\rm sc}a_{\rm sc} + \frac{H_{\rm sc}\Gamma_{\rm pm} - H_{\rm pm}\Gamma_{\rm sc} - H_{\rm pm}}{1 + H_{\rm pm} - \Gamma_{\rm pm} - H_{\rm sc} + \Gamma_{\rm sc}}n_d. \end{aligned} \tag{5.8}$$

Since $M_{\rm sc} \gg M_{\rm pm}$ we can take $\Gamma_{\rm sc} = 0$. Furthermore, for this discussion we are only concerned with the position of the proof mass along one arm of the interferometer. So that the measurement is limited by proof mass actuator noise, the proof mass controller should have negligible gain in the measurement band $|C_{\rm pm}| \ll 1$. With these simplifications setting $\Gamma_{\rm sc} = 0$ and $C_{\rm pm} = 0$, (5.8) becomes

$$x_{\rm sc} = \frac{1 - H_{\rm sc}}{1 - \Gamma_{\rm pm} - H_{\rm sc}}P_{\rm pm}a_{\rm pm} - \frac{\Gamma_{\rm pm}P_{\rm sc}}{1 - \Gamma_{\rm pm} - H_{\rm sc}}a_{\rm sc} + \frac{\Gamma_{\rm pm}H_{\rm sc}}{1 - \Gamma_{\rm pm} - H_{\rm sc}}n_d. \tag{5.9}$$

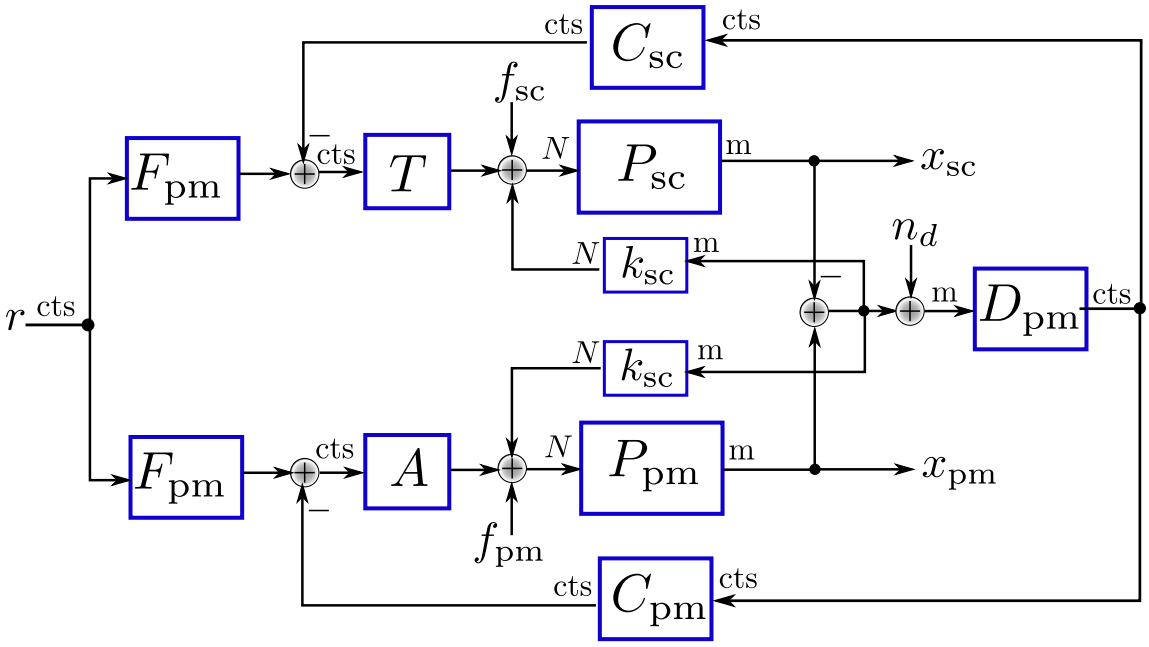

Figure 5.4: TianGO control system. P_{pm}, C_{pm}, and F_{pm} are the proof mass plant, controller, and feedforward controller, respectively. Similarly for P_{sc}, C_{sc}, and F_{sc} for the spacecraft. D_{pm} is the proof mass displacement sensor, A are the proof mass actuators, and T are the spacecraft thrusters. A spring-like coupling with spring constant k_{sc} couples the proof mass to the spacecraft. x_{pm} and f_{pm} are the proof mass position and the external forces acting on the proof mass, respectively, and similarly for x_{sc} and f_{sc} for the spacecraft. n_d is displacement noise of the position sensor. The units of every link are also labeled ("cts" stands for counts and labels digital signals).

5.4 Noise Budget

TianGO will employ drag-free flight and will benefit from the development of LISA's disturbance reduction system (DRS) used to keep the LISA proof masses in free fall as accurately as possible. Acceleration noises acting on the spacecraft, discussed in Sec. 5.4.4 are suppressed by the DRS. Acceleration noises acting directly on the proof mass, however, are not and are described in Secs. 5.4.1 and 5.4.2. Quantum noise is described in Sec. 5.4.3 and the full noise budget is given in Sec. 5.4.5.

5.4.1 Proof mass Environmental Acceleration Noises

Magnetic There are two sources of magnetic fields that contribute to proof mass acceleration noise: magnetic fields on the spacecraft itself $\mathbf{B}_{\rm sc}$ and magnetic fields in interplanetary space $\mathbf{B}_{\rm ip}$. The magnitude of the interplanetary field ranges from 5–50 nT and has a spectral density of roughly $S_{B_{\rm ip}}^{1/2} = (30 \times 10^{-8})(1\text{mHz}/f)\,\text{T}/\sqrt{\text{Hz}}$ [86].

These magnetic fields give rise to two noise sources. First, since the proof mass is moving through the interplanetary field with velocity $\mathbf{v}$, if it has a charge q, it will experience an acceleration due to the Lorentz force of [14, 86]

$$\mathbf{a} = \frac{1}{M_{\rm pm}}(q\,\mathbf{v} \times \mathbf{B}_{\rm ip}) = \frac{1}{M_{\rm pm}}(q\,\mathbf{v} \times \mathbf{B}_{\rm ip} + \delta q\,\mathbf{v} \times \mathbf{B}_{\rm ip} + q\,\mathbf{v} \times \delta\mathbf{B}_{\rm ip}). \tag{5.10}$$

The charge that accumulates on the proof mass will be periodically discharged, and between these events the first term grows linearly as $\dot{q}t$. The last two fluctuating terms give rise to the acceleration noise due to the Lorentz force of

$$S_a^{(\text{Lorentz})} = \frac{1}{M_{\rm pm}^2}\left[(v\bar{B}_{\rm ip})^2 S_q + (vq)^2 S_{B_{\rm ip}}\right]. \tag{5.11}$$

The charge fluctuations are due to shot noise in the current $I = \dot{q}_{\rm eff}$ flowing to the proof mass where $\dot{q}_{\rm eff} = \lambda_{\rm eff} e$ is an effective charging rate and e is the electron charge. Since

$S_I = 2e\dot{q}_{\rm eff}$, this noise is

$$S_q^{1/2} = \frac{e\sqrt{2\lambda_{\rm eff}}}{2\pi f}. \tag{5.12}$$

LISA Pathfinder measured $\lambda_{\rm eff}$ to be between 1000 and 1400 $\rm s^{-1}$, a factor of roughly 5 higher than expected [87], though the exact value will likely be different for the TianGO proof masses. Magnetic noise is not close to being a limiting noise according to the noise budget Fig. 5.6, so finding an exact value is not critical at this time.

Second, the interaction of any proof mass dipole moment $\mathbf{m}$ with the magnetic fields will give rise to a force $\nabla(\mathbf{m}\cdot\mathbf{B})$. The total dipole moment is the sum of an intrinsic dipole moment $\mathbf{m}_0$ and an induced magnetic moment from the spacecraft magnetic field:

$$\mathbf{m} = \mathbf{m}_0 + \frac{\chi V_{\rm pm}}{\mu_0}\mathbf{B}_{\rm sc} \tag{5.13}$$

where χ is the magnetic susceptibility and $V_{\rm pm}$ is the proof mass volume. The acceleration due to this force to first order in magnetic field fluctuations is thus [88]

$$\mathbf{a} = \left[\frac{\mathbf{m}_0}{m_{\rm pm}} + \frac{\chi}{\rho\mu_0}(2\mathbf{B}_{\rm sc} + \mathbf{B}_{\rm ip})\right]\cdot\nabla\mathbf{B}_{\rm sc} + \frac{\chi}{\rho\mu_0}(2\delta\mathbf{B}_{\rm sc} + \delta\mathbf{B}_{\rm ip})\cdot\nabla\mathbf{B}_{\rm sc} \tag{5.14}$$

where ρ is the density of the proof mass and we have ignored gradients of the interplanetary field. The first term is a DC force canceled by the control systems. The total acceleration noise due to forces on the magnetic dipole moment are

$$S_a^{(\rm dip)} = \left(\frac{\chi}{\rho\mu_0}|\nabla B_{\rm ip}|\right)^2 \left(4S_{B_{\rm sc}} + S_{B_{\rm ip}}\right). \tag{5.15}$$

It is possible to partially shield the proof mass from electric and magnetic fields [14, 86]. Taking this possibility into account, the total magnetic noise is the sum of the noise due to the Lorentz force and the noise due to the interaction of the dipole moment with the magnetic fields

$$S_a^{(\rm mag)} = \frac{1}{\xi_e^2}S_a^{(\rm Lorentz)} + \frac{1}{\xi_m^2}S_a^{(\rm dip)} \tag{5.16}$$

where ξ_m and ξ_e are magnetic and electric shielding factors.

Residual Gas Damping Residual gas molecules striking the proof mass lead to a Brownian force noise which is given by the fluctuation-dissipation theorem [89–91]

$$S_F^{(\mathrm{RG})} = 4k_B T\beta \tag{5.17}$$

where β is the gas damping coefficient of the gas, which depends on the geometry and environment of the proof mass. The geometry relevant for TianGO is that of a cylindrical mirror of radius R_{pm} and height h_{pm} enclosed in a housing separated by a gap d. If such a cylinder were in an infinite volume of gas of molecular mass m at pressure P without the housing, the gas damping coefficient would be [90]

$$\beta^{\infty} = \pi R_{\mathrm{pm}}^2 P\sqrt{\frac{8}{\pi}}\left(1 + \frac{h_{\mathrm{pm}}}{2R_{\mathrm{pm}}} + \frac{\pi}{4}\right)\sqrt{\frac{32m}{\pi k_B T}}. \tag{5.18}$$

The presence of the housing increases the force noise since a molecule will bounce several times between the proof mass and the housing. A full calculation of this effect requires simulation. However Ref. [89] showed that, for a cube of side length L in the limit $d \ll L$, the damping coefficient is increased from its infinite volume limit by

$$\beta = \frac{\beta^{\infty}}{\ln(L_{\mathrm{pm}}/d)(d/L_{\mathrm{pm}})^2} \tag{5.19}$$

and found the result in agreement with a torsion balance experiment to within 10%.

A rough estimate based on (5.19) suggests that $\beta/\beta^{\infty} \approx 50$ for TianGO's proof masses, though this is likely overly pessimistic. The proof mass housing likely does not have to fully surround the proof mass. Residual gas damping between the test and reaction masses was an important source of noise in advanced LIGO [91] until the reaction masses, hanging behind the test masses and used to actuate on them, were changed from cylinders to annuluses [92]. Gaps in the TianGO proof mass housing can likely be introduced as well.

Even if the increase from β^{∞} to β is reduced, residual gas damping is a serious source of noise. In the noise budget shown in Fig. 5.6, the residual gas trace is plotted

with $\beta = \beta^{\infty}$ and is still the dominant source of noise below about 100 mHz. This suggest investigating changing the shape of the proof masses to minimize the residual gas damping. Since this is such an important source of noise, it merits future detailed numerical study.

Classical Radiation Pressure The force exerted on a perfect reflector by light of power P due to radiation pressure is $2P/c$. The acceleration noise caused by classical fluctuations in this power is thus

$$\left[S_a^{(\text{class. RP})}\right]^{1/2} = \frac{2P}{cM_{\text{pm}}} S_{\delta P/P}^{1/2}, \tag{5.20}$$

where $S_{\delta P/P}^{1/2}$ is the relative intensity noise of the stabilized laser. The intensity stabilization servo will stabilize the laser to around $S_{\delta P/P}^{1/2} = (10^8 \text{ RIN}/\sqrt{\text{Hz}}) \times (0.1 + f)/f$ and the common mode rejection of the interferometer will provide another factor of about 1000 suppression of the intensity noise.

Thermal Radiation Pressure In addition to the classical radiation pressure from the lasers, thermal photons emitted from the proof mass housing will also exert radiation pressure on the proof mass. Thermal fluctuations across the proof mass thus lead to fluctuating thermal radiation pressure. The power radiated from the proof mass housing in the sensitive direction is $P = \pi R_{\text{pm}}^2 \sigma T^4$ where σ is the Stefan-Boltzmann constant and the radiation pressure force is $2P/3c$ with the extra factor of three accounting for the fact that not all photons radiated from the housing strike the proof mass at normal incidence. The force due to a small thermal gradient δT is thus

$$F = \frac{8\sigma}{3c} \pi R_{\text{pm}}^2 T^3 \delta T \tag{5.21}$$

leading to an acceleration noise [93, 94]

$$\left[S_a^{(\text{therm. RP})}\right]^{1/2} = \kappa_{\text{RP}} \frac{8\sigma}{3M_{\text{pm}}c} \pi R_{\text{pm}}^2 T^3 S_T^{1/2} \tag{5.22}$$

where S_T is the PSD of the temperature fluctuations. The factor $\kappa_{\rm RP}$ accounts for the edge effect of photons with a component of momentum normal to one of the proof mass faces striking a neighboring face. This factor also accounts for the absorption of the proof mass and whether the reflection is specular or diffuse. $\kappa_{\rm RP}$ must be calculated through simulations, which depend on the proof mass geometry, and can range from 0.32–1.17 in the simulations presented in Tables I and II of Ref. [93], which calculates it for a cube. Though the estimate used here is not exact, thermal radiation pressure is not one of the dominant noise sources and so a more in depth numerical study is not critical.

Radiometric Thermal fluctuations across the proof mass lead to differential pressure fluctuations in the residual gas. The force due to a small temperature gradient δT is [93, 94]

$$F = \kappa_R \frac{\pi R_{\rm pm}^2 P}{4T} \delta T, \tag{5.23}$$

where κ_R is again a factor accounting for edge effects coming from gas molecules striking neighboring sides of the proof mass. This leads to an acceleration noise

$$\left[S_F^{(\rm rad)}\right]^{1/2} = \kappa_R \frac{\pi R_{\rm pm}^2 P}{4 M_{\rm pm} T} S_T^{1/2}. \tag{5.24}$$

As with thermal radiation pressure, this calculation is not exact, but it is not expected to be one of the dominant noise sources.

Differential Outgassing The outgassing of molecules from the proof mass enclosure depends on temperature and thus leads to a fluctuating force in the presence of temperature fluctuations. A simple model for this effect is to consider a gas flow of $Q = Q_0 \mathrm{e}^{-\Theta/T}$ where Θ is an activation temperature [93, 95]. According to this model, the force produced by a differential outgassing rate δQ is $F = \pi R_{\rm pm}^2 \delta Q / C_{\rm eff}$ where $C_{\rm eff}$ is a geometric factor estimated in [95] to be roughly $4.3 \cdot 10^{-2}\,\mathrm{m}^3/\mathrm{s}$ for the LISA geometry. The equiv-

alent acceleration noise is thus

$$\left[S_a^{(\text{outgas})}\right]^{1/2} = \frac{\pi R_{\text{pm}}^2}{M_{\text{pm}} C_{\text{eff}}} \frac{Q_0 \Theta}{T^2} \mathrm{e}^{-\Theta/T} S_T^{1/2}. \tag{5.25}$$

This effect is difficult to accurately model, but values of $Q_0 \sim 1.4\,\text{nJ/s}$ and $\Theta \sim 3 \cdot 10^4\,\text{K}$ are characteristic of the materials used for the LISA proof mass and enclosure [93]. Again, this is not expected to be a dominant noise source.

Newtonian The spacecraft itself exerts a classical Newtonian gravitational force on the proof mass. The distribution of the spacecraft mass will change in the presence of thermal fluctuations due to thermal expansion. Ref. [86] made a crude estimate of this effect by considering a mass M_{dis} a distance x_{dis} moving by thermal expansion. The length fluctuations of a mass a distance x_{dis} from the proof mass are $S_x^{1/2} = \alpha x_{\text{dis}} S_T^{1/2}$ where α is the coefficient of thermal expansion of the spacecraft. The acceleration noise due to the fluctuating distance of this disturbing mass from the proof mass is thus

$$\left[S_a^{(\text{Newt})}\right]^{1/2} = \frac{2GM_{\text{dis}}}{x_{\text{dis}}^3} S_x^{1/2} = \frac{2\alpha G M_{\text{dis}}}{x_{\text{dis}}^2} S_T^{1/2}. \tag{5.26}$$

This crude estimate shows that the gravity gradients are possibly one of the dominant noise sources for TianGO and this effect thus warrants a more detailed analysis.

Cosmic Rays Cosmic rays with enough energy to penetrate the spacecraft impart momentum to the proof mass. Protons with energy $E_{\text{pr}} \gtrsim 300\,\text{eV}$ have enough energy to penetrate the spacecraft and arrive at a rate of $n_{\text{pr}} \approx 30\,\text{protons/s}$ [86]. The acceleration noise to the proof mass caused by cosmic ray impacts is

$$\left[S_a^{(\text{CR})}\right]^{1/2} = \frac{\sqrt{2 n_{\text{pr}} m_{\text{pr}} E_{\text{pr}}}}{M_{\text{pm}}}, \tag{5.27}$$

where m_{pr} is the proton mass.

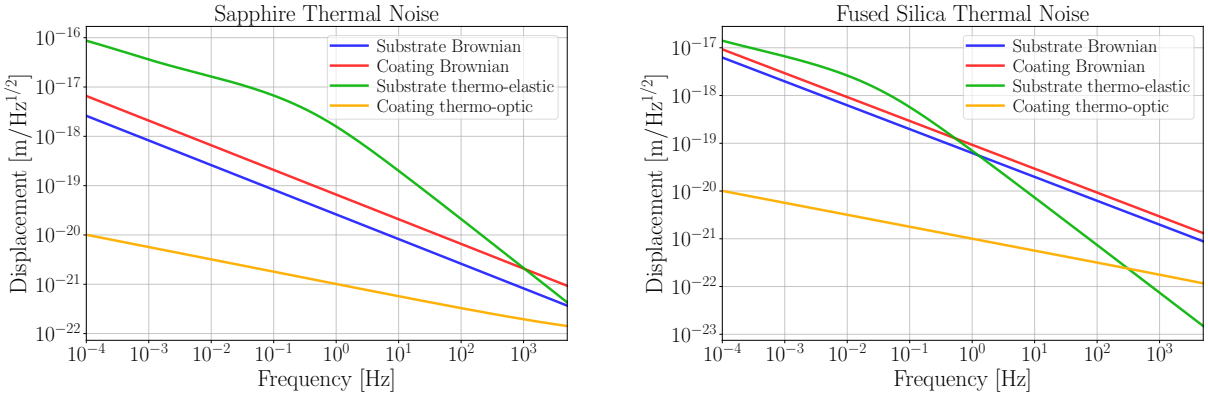

Figure 5.5: TianGO proof mass thermal noise

5.4.2 Thermal Noise

Thermal noise in the mirrors is another source source of spacecraft environmental noise, but it is present in the telescopes as well. The thermal noise is split into thermal noise in the coatings on the surface of the mirrors and thermal noise in the bulk or substrate.

Brownian Noise Brownian noise in the coatings and the substrate cause a displacement noise of [96–98]

$$S_x^{(\text{Brown})} = \frac{2k_B T}{\pi^{3/2} f} \frac{1-\nu^2}{wE} \left[\phi_s + \frac{2(1-2\nu) d_c \phi_c}{\sqrt{\pi}(1-\nu) w} \right] \tag{5.28}$$

where w is the beam spot size on the mirror, ϕ_s and ϕ_c are the loss angles of the substrate and coating, respectively, E is the Young's modulus, d_c is the coating thickness, and ν is the Poisson ratio. Eq. (5.28) is for an infinite size test mass, but Ref. [98] includes finite size effects, which are included in the calculations here as well.

Substrate Thermo-elastic Noise Thermal fluctuations lead to fluctuations in the coefficient of thermal expansion which then lead to displacement fluctuations [98–100].

Quantity	Symbol	Fused Silica	Sapphire	Units
Young's modulus	E	7.2×10^{10}	4×10^{11}	Pa
Poisson ratio	ν	0.17	0.23	-
Heat capacity	C	1.64×10^{6}	3.09×10^{6}	J/K/m^3
Coefficient of thermal expansion	α	5.1×10^{-7}	5.4×10^{-6}	1/K
Thermal conductivity	κ	1.38	33	W/m/K
Index of refraction	n	1.45	1.76	-
Density	ρ	2.2×10^{3}	4×10^{3}	kg/m^3

Table 5.1: TianGO mirror substrate parameters from [103].

This noise in the infinite test mass limit is [100]

$$S_x^{(\text{sub. TE})} = \frac{4\alpha^2(1+\nu)^2 k_B T^2 w}{\sqrt{\pi}\kappa} J(f/f_c) \tag{5.29}$$

where α is the coefficient of thermal expansion, κ is the thermal conductivity, $f_c = \kappa/\pi C w^2$, C is the specific heat per unit volume,[1] ρ is the density, and [102]

$$J(x) = \text{Re}\left\{\frac{e^{ix/2}(1-ix)}{x^2}\left[\text{erf}\,\frac{\sqrt{x}(1+i)}{2} - 1\right]\right\} + \frac{1}{x^2} - \frac{1}{\sqrt{\pi x^3}}. \tag{5.30}$$

For $x \gg 1$, $J(x) \to 1/x^2$ and so, for $f \gg f_c$,

$$S_x^{(\text{sub. TE})}(f \gg f_c) = \frac{4k_B T^2}{\pi^{5/2} f^2} \frac{\alpha^2(1+\nu)^2\kappa}{C^2 w^3}. \tag{5.31}$$

Ref. [98] again includes finite size effects to (5.29), which are included in the calculations here as well.

Coating Thermo-optic Noise In addition to thermo-elastic noise, thermal fluctuations lead to fluctuations in the index of refraction [101, 104, 105]. The combination of thermo-elastic and thermo-refractive noise is called thermo-optic noise. Since both of these noises come from the same thermal fluctuations, they must add coherently to give the total thermo-optic noise [106, 107]. The spectrum of thermal fluctuations responsible

[1] Note that Refs. [98–101] use the specific heat per unit mass $C_V = C/\rho$ where C is the specific heat per unit volume used here.

for thermo-optic noise in the coatings is [101]

$$S_T = \frac{2k_B T^2}{\pi^{3/2} w^2 \sqrt{fC\kappa}} \tag{5.32}$$

and the total thermo-optic noise is [106]

$$S_x^{(\text{coat. TO})} = \Gamma_{\text{tc}} S_T \left(\alpha_c d_c - \beta_c \lambda_0 - \alpha_s d_c \frac{C_c}{C_s} \right)^2 \tag{5.33}$$

where λ_0 is the wavelength of the light, α_c, β_c, and C_c are the coefficient of thermal expansion, coefficient of thermal refraction, and heat capacity of the coating, and α_s and C_s are the same for the substrate. Γ_{tc} is a correction factor accounting for the thickness of the coating which goes to 1 if the coating thickness d_c is much less than the thermal diffusion length $r_T = \sqrt{\kappa/2\pi fC}$. In the calculations here we use the details of the LIGO Voyager coatings [8].

5.4.3 Quantum Noise

There are two sources of quantum noise: shot noise and radiation pressure. For all frequencies above 1 Hz, the interferometer sensitivity is limited by photon shot noise. As discussed in Sec. 5.3.1, TianGO uses squeezing to decrease shot noise at the expense of increasing quantum radiation pressure.

The phase noise due to shot noise is

$$S_\phi^{(\text{shot})} = \frac{2\hbar\omega_0}{P_{\text{bs}}} \left[(1-\epsilon) 10^{-r_{\text{sqz}}/10} + \epsilon \right] \tag{5.34}$$

where r_{sqz} is the squeeze factor and ϵ are losses, and the radiation pressure is

$$\left[S_F^{(\text{quant. RP})} \right]^{1/2} = \frac{2}{c} \sqrt{2\hbar\omega_0 P_{\text{bs}}}\, 10^{r_{\text{anti}}/20} \tag{5.35}$$

where r_{anti} is the anti-squeeze factor.

5.4.4 Spacecraft Environmental Acceleration Noises

Solar Radiation Pressure In addition to the various sources of radiation pressure acting directly on the proof masses, radiation pressure from the sun acts on the spacecraft. The DC solar irradiance is $W = 1.3\,\mathrm{kW/m^2}$ and the relative intensity of the solar irradiance is $S^{1/2}_{\delta W/W} = (1.3 \times 10^{-3})(1\,\mathrm{mHz}/f)^{1/3}/\sqrt{\mathrm{Hz}}$ [86, 108]. The acceleration noise *on the spacecraft* due to solar radiation pressure is

$$\left[S_a^{(\text{sc RP})}\right]^{1/2} = \frac{2A_{\text{sc}}W}{cM_{\text{sc}}} S^{1/2}_{\delta W/W} \tag{5.36}$$

where A_{sc} is the area of the spacecraft.

Thrusters The drag-free thrusters used for LISA are expected to produce a force noise of roughly $\left[S_F^{(\text{thr})}\right]^{1/2} = 10^{-7}\,\mathrm{N}/\sqrt{\mathrm{Hz}}$ [86]. The TianGO thrusters may be different, but this is not a limiting source of noise. Furthermore, the coupling of the thruster noise to the proof mass acceleration can be changed with the spacecraft controller C_{sc} discussed in Sec. 5.3.3 and Fig. 5.4.

5.4.5 Full Noise Budget

To compute the full noise budget, we need to propagate the above noises through the control system described in Sec. 5.3.3. So that the acceleration noises from the spacecraft minimally disturb the proof mass, the spacecraft controller gain should be large $|C_{\text{sc}}| \gg 1$. In this limit, the closed loop position of the proof mass (5.9) becomes

$$x_{\text{pm}} = \frac{1}{\Omega^2}\left(a_{\text{pm}} - \frac{1}{H_{\text{sc}}}\frac{\omega_{\text{sc}}^2}{\Omega^2}a_{\text{sc}} - \omega_{\text{sc}}^2 n_d\right). \tag{5.37}$$

The total strain noise is, therefore,

$$S_h^{1/2} = \frac{1}{L\Omega^2}\sqrt{S_a^{(\text{pm})} + S_a^{(\text{ba})} + \left(\frac{1}{H_{\text{sc}}}\frac{\omega_{\text{sc}}^2}{\Omega^2}\right)^2 S_a^{(\text{sc})} + \omega_{\text{sc}}^4 S_x^{(\text{sens})}}, \tag{5.38}$$

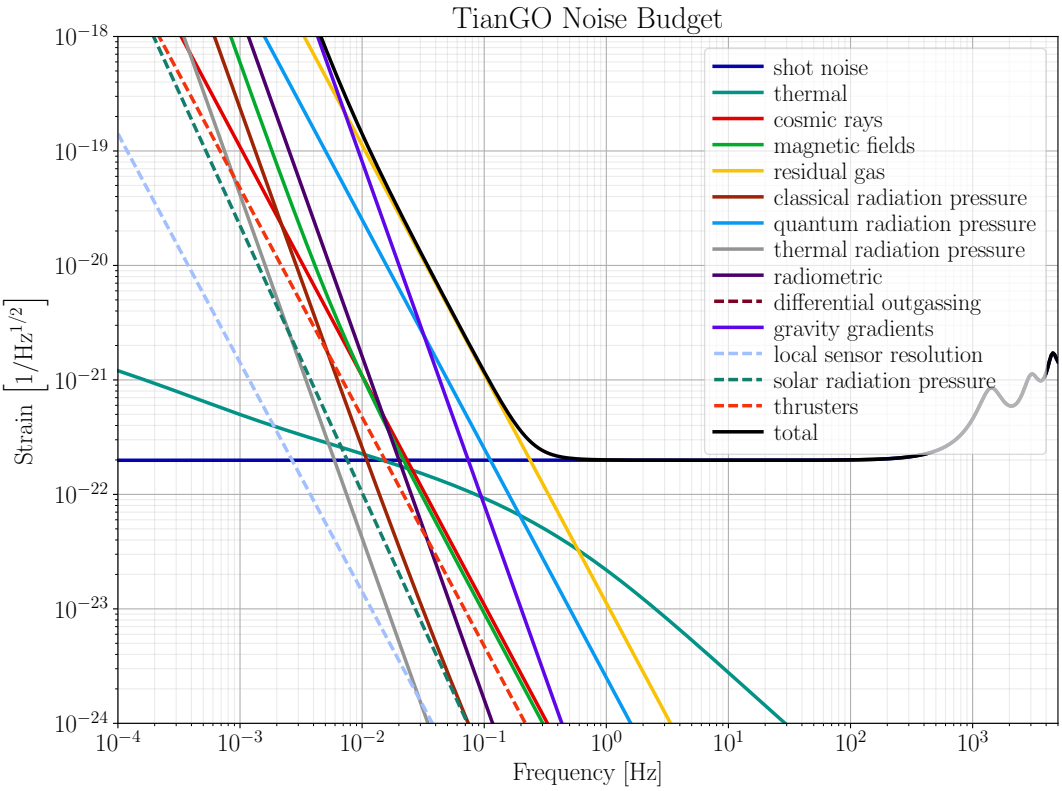

Figure 5.6: TianGO noise budget with sapphire mirrors. For fused silica mirrors the thermal noise is better, see Fig. 5.5, but the residual gas damping is worse because sapphire is denser than fused silica. Fused silica mirrors have to be bigger for the same mass, which increases residual gas damping, see (5.18).

where $S_x^{(\mathrm{sens})}$ is displacement noise due to the proof mass displacement sensor D_{pm} in Fig. 5.4. The full noise budget is shown in Fig. 5.6.

5.5 Future Work

There is much to be done both in developing the technical aspects of the TianGO detector and evaluating its scientific promise.

The above analysis did not incorporate the way the proof masses are actuated. One possibility may be to use electrostatic actuators as are used for the LIGO test masses [109], however excess noise has been observed in previous aLIGO observing runs

due to charging from these actuators [110]. This could also make the magnetic noises discussed above worse. It is also unclear how to control all degrees of freedom of the cylindrical proof masses. It is important to know how the proof masses will be controlled because, in addition to the direct force noise from the actuators, the control will create some kind of spring-like coupling between the spacecraft and the proof masses. These are all important effects for noise budgeting.

The above description of the control system was also heuristic. It should be checked in more detail that the necessary controller gains can be achieved and that the actuator noise is tolerable. The operation of TianGO also relies on us actively suppressing the arm length changes of the uncontrolled orbits with spacecraft thrusters, as are illustrated in Fig. 5.1 for example. The fuel requirements also need to be investigated to see if this is feasible [111, 112].

More accurate estimates of TianGO's ability to localize sources and its ability to estimate astrophysical source parameters, both by itself and when integrated with a terrestrial detector network, need to be made. This has proven technically difficult for numerous reasons, but the waveforms described in Appendix C combined with a Fisher matrix analysis [113–116] should make this possible.

Finally, the choice of orbit will also affect the details of the control scheme and the scientific promise of the detector. Orbits near L2, which is 0.01 AU from the Earth, require less forces to control than Earth trailing orbits to keep the arm lengths constant but are closer to the Earth and thus provide a smaller baseline with the ground detectors for sky localization. Orbits near L2 also require less fuel to get into and are thus cheaper. An in depth study of these trade offs needs to be made once more accurate estimates of sky localization have been done.

Appendix A

Recycling Cavity Lengths

A dual-recycled Fabry-Perot Michelson interferometer (see Fig.3.1), such as the 40 m interferometer or LIGO, have five length degrees of freedom: the common and differential arm lengths (CARM and DARM), the power recycling cavity length (PRCL), the signal recycling cavity length (SRCL), and the Michelson length (MICH) which is the difference in the distance between the two ITMs and the beam splitter. To simultaneously control these lengths, two sets of RF phase sidebands are added to the main laser before it enters the interferometer. These are known as the f_1 and $f_2 = 5f_1$ sidebands. At the 40 m, $f_1 = 11\,\mathrm{MHz}$ and $f_2 = 55\,\mathrm{MHz}$. These sidebands have different resonance conditions in the different interferometer cavities which enables one to monitor the lengths of the cavities. See, for example, Ref. [39] for a description of how these sidebands are used to sense and control these five degrees of freedom.

For this control scheme to work, both the f_1 and f_2 sidebands are resonant in the PRC, the f_2, but not the f_1, sidebands are resonant in the SRC, and neither the f_1 or f_2 sidebands are resonant in the arms. Here we are only concerned with how the macroscopic lengths of the recycling cavities are chosen to satisfy these conditions.

The reflectivity of a Fabry-Perot cavity of length L with input mirror reflectivity r_i

and end mirror reflectivity r_e is

$$r(\phi) = \frac{-r_i + r_e e^{-2i\phi}}{1 - r_i r_e e^{-2i\phi}} \tag{A.1}$$

where $\phi = \omega L/c$ is the phase a field of frequency ω accrues going one-way along the cavity. Eq. (A.1) also holds when the mirrors are compound cavities with complex reflectivities. A cavity is said to be resonant if the round-trip phase is zero and anti-resonant if the round-trip phase is π. Taking the possibly complex arm reflectivities into account, these conditions are

$$\text{resonant :} \qquad \arg\left(r_i r_e e^{-2i\phi}\right) = 2\pi n \tag{A.2a}$$

$$\text{anti-resonant :} \qquad \arg\left(r_i r_e e^{-2i\phi}\right) = (2k+1)\pi. \tag{A.2b}$$

Eq. (A.1) is the fundamental relation that sets the macroscopic cavities lengths.

A.1 Arm Cavities

The arm cavities are chosen to be resonant for the carrier ω_0 and (nearly) anti-resonant for the sidebands $\omega_0 \pm \Omega_i$. The end mirrors are highly reflective $r_e \approx 1$ and so

$$r_{\text{arm}}(\omega_0) = \frac{-r_{\text{itm}} + 1}{1 - r_{\text{itm}}} = 1. \tag{A.3}$$

If the sidebands were exactly anti-resonant

$$r_{\text{arm}}(\omega_0 + \Omega_i) = \frac{-r_{\text{itm}} - 1}{1 + r_{\text{itm}}} = -1. \tag{A.4}$$

In practice the sidebands are chosen to not be exactly anti-resonant in order to avoid higher harmonics from resonating in the arms. The sidebands thus have complex reflectivities

$$r_{\text{arm}}(\omega_0 + \Omega_i) = |r_{\text{arm}}(\Omega_i)| e^{i\theta_i} \tag{A.5}$$

where $|\pi - \theta_i| \ll 1$. For the 40 m arm cavities, $\theta_1 = 180.5°$ and $\theta_2 = 182.5°$.

A.2 Power Recycling Cavity

The power recycling cavity length is chosen so that the carrier and both sidebands are resonant in the PRC when the arms are resonant for the carrier. For the carrier

$$\arg\left[r_{\mathrm{prm}} r_{\mathrm{arm}}(\omega_0) \mathrm{e}^{-2\mathrm{i}\omega_0 L_{\mathrm{prc}}/c}\right] = 2\pi n \tag{A.6}$$

and so L_{prc} is microscopically adjusted such that $\omega_0 L_{\mathrm{prc}}/c = n\pi$. For the f_1 sideband

$$\arg\left[r_{\mathrm{prm}}|r_{\mathrm{arm}}(\Omega_1)|\mathrm{e}^{\mathrm{i}\theta_1}\mathrm{e}^{-2\mathrm{i}\omega_0 L_{\mathrm{prc}}/c}\mathrm{e}^{-2\mathrm{i}\Omega_1 L_{\mathrm{prc}}/c}\right] = \theta_1 + 0 - \frac{2\Omega_1 L_{\mathrm{prc}}}{c} = 2\pi n \tag{A.7}$$

and so the power recycling length must satisfy

$$L_{\mathrm{prc}} = \left(k + \frac{\theta_1}{2\pi}\right)\frac{c}{2f_1}. \tag{A.8}$$

If (A.8) is satisfied for f_1 then it is automatically satisfied for $f_2 = 5f_1$ if $\theta_2 - \pi = 5(\theta_1 - \pi)$. For the 40 m, we choose $k = 0$ giving $L_{\mathrm{prc}} = 6.753\,\mathrm{m}$.

A.3 Signal Recycling Cavity

The signal recycling cavity length is chosen so that the f_2 sideband is resonant and the f_1 sideband is non-resonant in the SRC when the arms are resonant for the carrier. Since the phase the carrier accrues in the SRC differs between signal recycling and resonant sideband extraction, the two cases have different requirements for the SRC length.

Signal Recycling With signal recycling the carrier does not acquire any phase in the SRC. This is the same as with the PRC. Since the f_2 sideband is also resonant in the PRC, the same condition (A.8) is necessary for L_{src} and f_2. Since f_1 has to be non-resonant in the SRC, however, the conditions that must be simultaneously satisfied are

$$L_{\mathrm{src}} = \left(n + \frac{\theta_2}{2\pi}\right)\frac{c}{2f_2} \tag{A.9a}$$

$$L_{\mathrm{src}} \neq \left(m + \frac{\theta_1}{2\pi}\right)\frac{c}{2f_1}. \tag{A.9b}$$

For the 40 m the first three lengths satisfying (A.9) are $1.336, 4.044$, and 9.463 m. For the ponderomotive squeezing experiment described in Chap. 3, we choose $n = 1$ giving $L_{\mathrm{src}} = 4.044$ m.

Resonant Sideband Extraction With RSE, the carrier has a one-way phase shift of $\pi/2$. So for the f_2 sideband to be resonant in the SRC,

$$\arg\left[r_{\mathrm{srm}}|r_{\mathrm{arm}}(\Omega_2)|\mathrm{e}^{\mathrm{i}\theta_2}\mathrm{e}^{-2\mathrm{i}\omega_0 L_{\mathrm{src}}/c}\mathrm{e}^{-2\mathrm{i}\Omega_2 L_{\mathrm{src}}/c}\right] = \theta_2 + \pi - \frac{2\Omega_2 L_{\mathrm{src}}}{c} = 2\pi n. \tag{A.10}$$

The conditions that must be simultaneously satisfied are thus

$$L_{\mathrm{src}} = \left(n + \frac{1}{2} + \frac{\theta_2}{2\pi}\right)\frac{c}{2f_2} \tag{A.11a}$$

$$L_{\mathrm{src}} \neq \left(m + \frac{1}{2} + \frac{\theta_1}{2\pi}\right)\frac{c}{2f_1}. \tag{A.11b}$$

General Detuning For a general detuning, leading to an optical spring, the carrier picks up a one-way phase of ϕ. Thus, for f_2 to be resonant,

$$\arg\left[r_{\mathrm{srm}}|r_{\mathrm{arm}}(\Omega_2)|\mathrm{e}^{\mathrm{i}\theta_2}\mathrm{e}^{2\phi}\mathrm{e}^{-2\mathrm{i}\Omega_2 L_{\mathrm{src}}/c}\right] = \theta_2 + 2\phi - \frac{2\Omega_2 L_{\mathrm{src}}}{c} = 2\pi n. \tag{A.12}$$

The conditions that must be simultaneously satisfied are thus

$$L_{\mathrm{src}} = \left(n + \frac{2\phi + \theta_2}{\pi}\right)\frac{c}{2f_2} \tag{A.13a}$$

$$L_{\mathrm{src}} \neq \left(m + \frac{2\phi + \theta_1}{\pi}\right)\frac{c}{2f_1} \tag{A.13b}$$

$$\tag{A.13c}$$

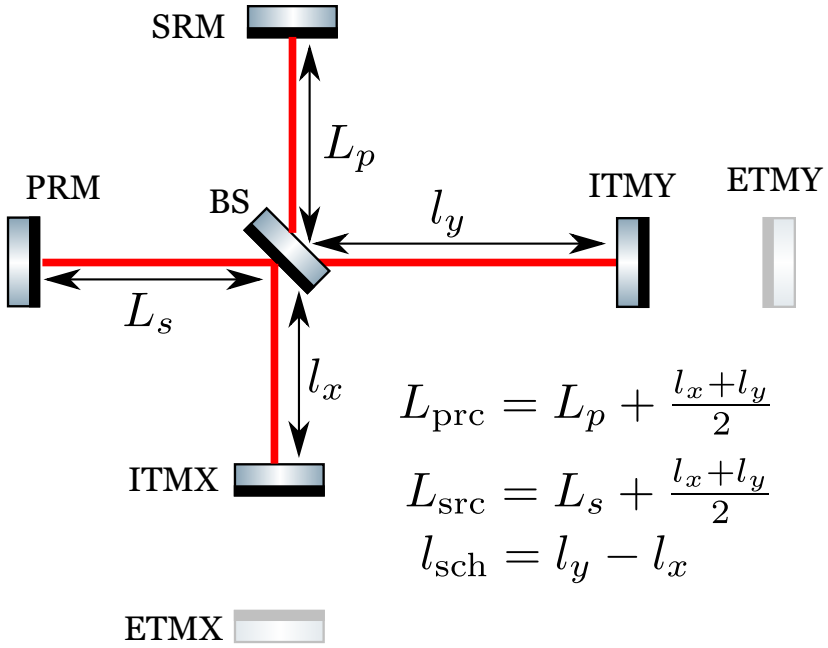

Figure A.1: Recycling cavity lengths

A.4 Schnupp Asymmetry

Once the lengths of the recycling cavities are set, the Schnupp asymmetry is chosen so that the f_2 sideband is critically coupled into the SRC. To find the couplings we need the transmission from the PRC to the SRC in a dual recycled Michelson interferometer with X and Y mirror reflectivities given by (A.5). With the lengths defined as

$$L_{\mathrm{prc}} = L_p + \frac{l_y + l_x}{2}, \qquad L_{\mathrm{src}} = L_s + \frac{l_y + l_x}{2}, \qquad l_{\mathrm{sch}} = l_y - l_x, \tag{A.14}$$

see Fig. A.1, we define the following phases:

$$\phi_x = \frac{\omega l_x}{c}, \qquad \phi_y = \frac{\omega l_y}{c}, \qquad \phi_\pm = \frac{\phi_y \pm \phi_x}{2} = \frac{\omega l_{\mathrm{sch}}}{2c}, \tag{A.15a}$$

$$\phi_p = \frac{\omega L_p}{c}, \qquad \phi_{\mathrm{prc}} = \frac{\omega L_{\mathrm{prc}}}{c} = \phi_p + \phi_+, \tag{A.15b}$$

$$\phi_s = \frac{\omega L_s}{c}, \qquad \phi_{\mathrm{src}} = \frac{\omega L_{\mathrm{src}}}{c} = \phi_s + \phi_+. \tag{A.15c}$$

The transmission and reflection of a simple Michelson formed by the beam splitter

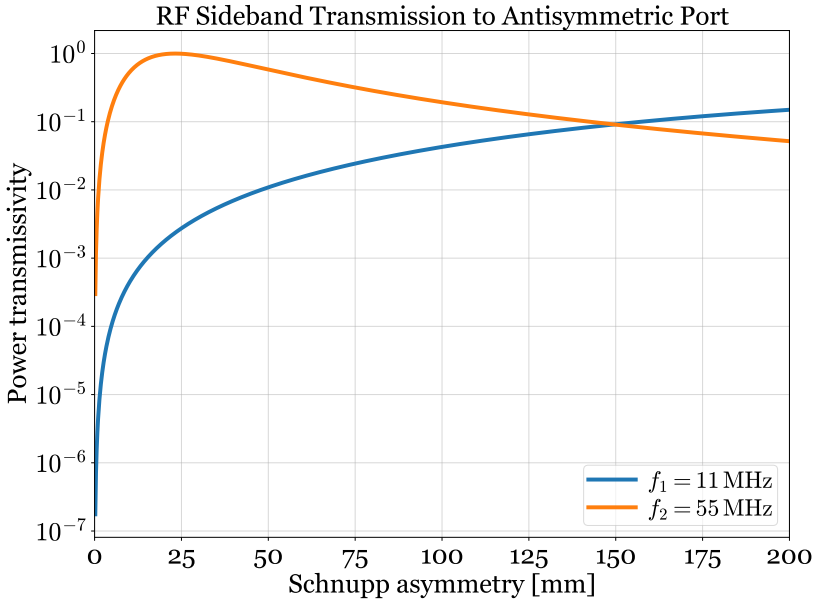

Figure A.2: RF sideband transmission to the asymmetric port for the 40 m interferometer configured for signal recycling. The maximum transmission for f_2 is 0.997 and occurs for $l_{\mathrm{sch}} = 23.2\,\mathrm{mm}$.

and end mirrors with reflectivities given by (A.5) are

$$t_{\mathrm{mich}} = \frac{r_{\mathrm{arm}}}{2} \mathrm{e}^{-2\mathrm{i}\phi_+} \left(\mathrm{e}^{2\mathrm{i}\phi_-} - \mathrm{e}^{-2\mathrm{i}\phi_-} \right) = \mathrm{i} r_{\mathrm{arm}} \mathrm{e}^{-2\mathrm{i}\phi_+} \sin 2\phi_- \tag{A.16}$$

$$r_{\mathrm{mich}} = \frac{r_{\mathrm{arm}}}{2} \mathrm{e}^{-2\mathrm{i}\phi_+} \left(\mathrm{e}^{2\mathrm{i}\phi_-} + \mathrm{e}^{-2\mathrm{i}\phi_-} \right) = r_{\mathrm{arm}} \mathrm{e}^{-2\mathrm{i}\phi_+} \cos 2\phi_- . \tag{A.17}$$

Using this, the transmission from the PRC to SRC is

$$t_{\mathrm{prc}\to\mathrm{src}} = t_{\mathrm{prm}} t_{\mathrm{srm}} \frac{\mathrm{i} r_{\mathrm{arm}} \mathrm{e}^{-\mathrm{i}(\phi_+ + \phi_{\mathrm{src}})} \sin 2\phi_-}{1 - r_{\mathrm{arm}} (r_{\mathrm{prm}} \mathrm{e}^{-2\mathrm{i}\phi_{\mathrm{prc}}} + r_{\mathrm{srm}} \mathrm{e}^{-2\mathrm{i}\phi_{\mathrm{src}}}) \cos 2\phi_- + r_{\mathrm{arm}}^2 r_{\mathrm{prm}} r_{\mathrm{srm}} \mathrm{e}^{-2\mathrm{i}(\phi_{\mathrm{prc}} + \phi_{\mathrm{src}})}} . \tag{A.18}$$

Eq. (A.18) can be simplified by noting that all fields we are considering are resonant in the PRC and so $\theta - 2\phi_{\mathrm{prc}} = 0$:

$$t_{\mathrm{prc}\to\mathrm{src}} = t_{\mathrm{prm}} t_{\mathrm{srm}} \frac{\mathrm{i} r_{\mathrm{arm}} \mathrm{e}^{-\mathrm{i}(\phi_+ + \phi_{\mathrm{src}})} \sin 2\phi_-}{1 - |r_{\mathrm{arm}}| [r_{\mathrm{prm}} + r_{\mathrm{srm}} \mathrm{e}^{\mathrm{i}(\theta - 2\phi_{\mathrm{src}})}] \cos 2\phi_- + |r_{\mathrm{arm}}|^2 r_{\mathrm{prm}} r_{\mathrm{srm}} \mathrm{e}^{\mathrm{i}(\theta - 2\phi_{\mathrm{src}})}} . \tag{A.19}$$

Eq. (A.19) must be used for general fields resonant in the PRC. However, for f_2 which

also must be resonant in the SRC, $\theta_2 - 2\phi_{\mathrm{src}} = 0$ and the transmission is

$$t_{\mathrm{prc}\to\mathrm{src}}(f_2) = t_{\mathrm{prm}} t_{\mathrm{srm}} \frac{\mathrm{i} r_{\mathrm{arm}} \mathrm{e}^{-\mathrm{i}(\phi_+ + \phi_{\mathrm{src}})} \sin 2\phi_-}{1 - |r_{\mathrm{arm}}|(r_{\mathrm{prm}} + r_{\mathrm{srm}}) \cos 2\phi_- + |r_{\mathrm{arm}}|^2 r_{\mathrm{prm}} r_{\mathrm{srm}}}. \tag{A.20}$$

Fig. A.2 shows the power transmissivity of the f_1 and f_2 sidebands to the asymmetric port as a function of Schnupp asymmetry l_{sch} for the 40 m. The maximum power transmission for f_2 is 0.997 and occurs at $l_{\mathrm{sch}} = 23.3\,\mathrm{mm}$.

Appendix B

Homodyne Detection

This appendix describes how signals are measured with balanced homodyne detection (BHD). Sec. B.1 describes the basic BHD setup where a local oscillator (LO) at the same frequency as the signal is used to optically demodulate the signal down from optical frequencies. As mentioned in Appendix. A, the laser is phase modulated with two sets of RF sidebands before entering the interferometer. These sidebands need to be removed using an output mode cleaner (OMC). Sec. B.2 describes an idea due to Koji Arai [19] which cleans both the LO and the signal with a single OMC by making the signal p-polarized and the LO s-polarized. Secs. B.3–B.5 analyze the displacement noise of this setup.

B.1 Basic Balanced Homodyne Detection

The basic balanced homodyne detector is shown in Fig. B.1. A strong local oscillator $E_{\mathrm{LO}}e^{i\zeta} = \sqrt{P_{\mathrm{LO}}}e^{i(\zeta+\omega t)}$ is mixed with the signal from the interferometer $E_{\mathrm{IFO}} = \sqrt{P_{\mathrm{IFO}}}e^{i\omega t}$ on a beam splitter where P_{LO} and P_{IFO} are the LO and interferomter power and ζ is the angle between the interferometer and LO quadratures. Assuming $P_{\mathrm{LO}} \gg P_{\mathrm{IFO}}$ the power

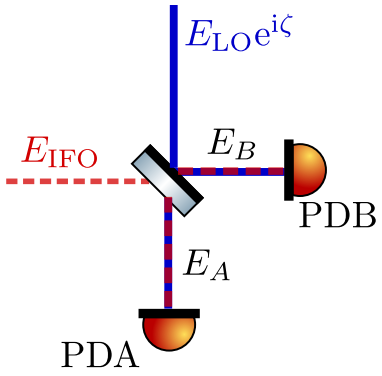

Figure B.1: Basic balanced homodyne detector

on the two photodiodes in Fig. B.1 is

$$P_A = \frac{1}{2}\left[P_{\mathrm{LO}} - 2\sqrt{P_{\mathrm{LO}}P_{\mathrm{IFO}}}(e^{i\zeta} + e^{-i\zeta})\right] \tag{B.1a}$$

$$P_B = \frac{1}{2}\left[P_{\mathrm{LO}} + 2\sqrt{P_{\mathrm{LO}}P_{\mathrm{IFO}}}(e^{i\zeta} + e^{-i\zeta})\right]. \tag{B.1b}$$

Subtracting the two photocurrents thus gives a signal proportional to the interferometer signal

$$P = \frac{P_B - P_A}{2} = \sqrt{P_{\mathrm{LO}}P_{\mathrm{IFO}}}\cos\zeta. \tag{B.2}$$

Ref. [117] analyzes noise from nonidealities in a BHD.

B.2 Two polarization OMC for BHD

When using a BHD to measure the signal from an interferometer, as in the experiment described in Chap. 3 and Fig. 3.1, the RF sidebands need to be cleaned off of both the signal and LO. A scheme for using a single OMC to filter both the LO and signal is shown in Fig. B.2. The signal from the interferometer is p-polarized and the LO is s-polarized. Since the signal and LO are in orthogonal quadratures they do not mix while they are simultaneously resonating in the OMC. A polarized beam splitter is placed before the two photodiodes. Before the signal and LO reach the PBS they are rotated by $\pi/4$.

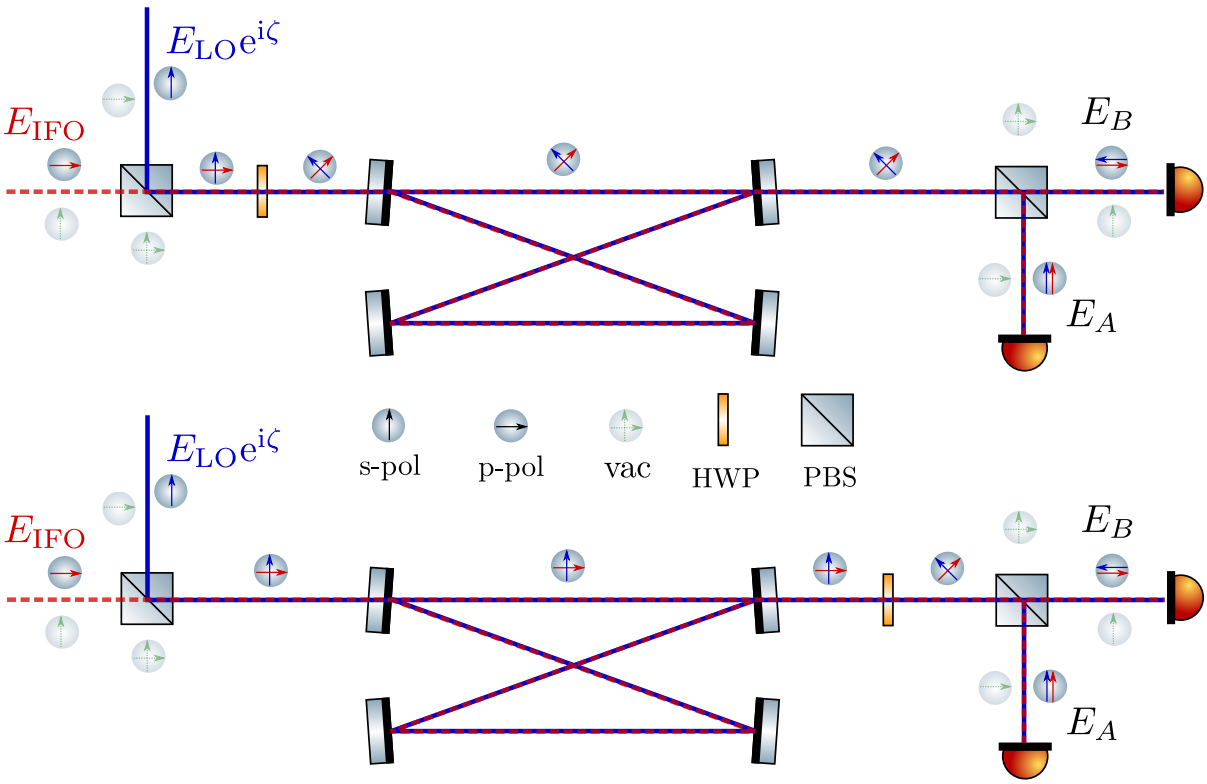

Figure B.2: Polarization OMC for BHD

Then, after the beam splitter the s-polarized field has signal and LO in phase and the p-polarized signal has the signal and LO out of phase. The signals from both photodiodes can then be subtracted as in regular BHD (B.2).

As shown in Fig. B.2, a half-wave plate can be used to rotate the polarizations by $\pi/4$ either before or after the OMC. These cases are analyzed in Secs. B.3 and B.4, respectively. In general the polarizations just need to have a net rotation of $\pi/4$ before the second PBS. It is thus possible to have a half-wave plate both before and after the OMC. This case is analyzed in Sec. B.5.

With the standard BHD scheme a single beam splitter is used. No extra quantum noise is added by this setup since there are no open ports for vacuum fluctations to enter through. On the other hand, the setup shown in Fig. B.2 has two PBS with one open port

each. Vacuum noise enters each of these open ports but does not add any extra quantum noise. For both PBS the vacuum that enters the system is polarized orthogonal to the signal. For the PBS before the PDs, PDB measures the p-polarized signal and PDA measures the s-polarized signals. But the s-polarized vacuum entering the PBS's open port is reflected to PDB and the p-polarized vacuum is transmitted to PDA. Similarly, no extra noise is added from the first PBS.

In the following, the field from the interferometer E_{IFO} is p-polarized and the LO field E_{LO} is s-polarized. The p-component is the field incident on PDB and the s-component is the field incident on PDA.

The OMC mirror coatings are birefringent and do not have the same reflectivity for s- and p-polarizations. The two polarizations have different cavity finesse and free spectral ranges and have different transfer functions through the OMC. The OMC is critically coupled and so the transfer function is approximately

$$G(f) = \frac{1}{1 + \mathrm{i}f/f_c} = \frac{\mathrm{e}^{\mathrm{i}\phi}}{1 + (f/f_c)^2} = |G|\mathrm{e}^{\mathrm{i}\phi} \tag{B.3}$$

where $f_c = f_{\mathrm{FSR}}/2\mathcal{F}$ is the cavity pole. We are interested in frequencies $f \ll f_c$. In this case the magnitude $|G| \approx 1$ and the phase $\phi \approx 0$. Since s and p have different transfer functions, we keep $|G|$ and ϕ general below to analyze the effects of OMC length fluctuations. However, once these effects have been calculated we can set $|G| = 1$ and $\phi = 0$ for both s and p and obtain the standard BHD signal (B.2).

The circulating power for the s- and p-polarizations in the OMC is shown schematically in Fig. B.3. The s-polarization has a higher finesse and a larger FSR than the p-polarization and so the circulating s-polarization is resonant at a higher frequency than the p-polarization. The cavity can be locked halfway between the two resonances.

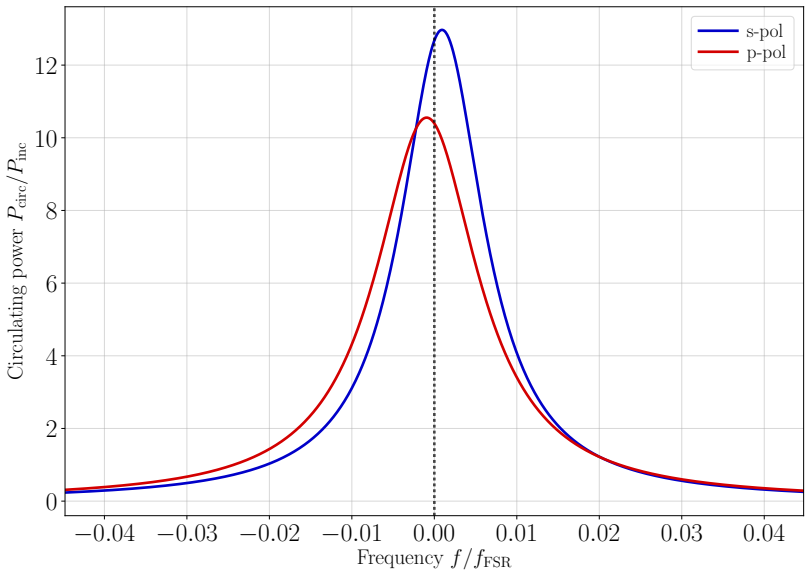

Figure B.3: OMC circulating power. The cavity finesse plotted is a factor of 10 less than the aLIGO OMCs and the frequency shift is exaggerated. For the aLIGO OMCs, $\delta f_{\rm FSR}/f_{\rm FSR} \approx 10^{-5}$.

B.3 Noise with the half-wave plate before the OMC

With the HWP before the OMC, the polarizations are rotated before entering the OMC. The field incident on the second PBS is thus

$$E = \frac{1}{\sqrt{2}} G_p \left(E_{\rm IFO} - E_{\rm LO} e^{i\zeta}\right) \hat{\mathbf{p}} + \frac{1}{\sqrt{2}} G_s \left(E_{\rm IFO} + E_{\rm LO} e^{i\zeta}\right) \hat{\mathbf{s}}. \tag{B.4}$$

and the homodyne signal is

$$P = \frac{1}{4}(P_{\rm IFO} + P_{\rm LO})\left(|G_s|^2 - |G_p|^2\right) + \frac{1}{2}\sqrt{P_{\rm IFO} P_{\rm LO}}\left(|G_s|^2 + |G_p|^2\right)\cos\zeta. \tag{B.5}$$

Since the cavity is locked off resonance for both polarizations, OMC length fluctuations lead to first order fluctuations in the circulating power. The slope of the magnitude of the transfer function is

$$\frac{\partial |G|^2}{\partial f} = -\frac{2 f/f_c^2}{[1 + (f/f_c)^2]^2}. \tag{B.6}$$

Since the cavity is locked halfway between the two resonances at $\pm\delta f_{\rm FSR}/2$, for $f \ll f_c$,

$$\frac{\partial |G_p|^2}{\partial x} = \frac{\delta f_{\rm FSR}}{f_c^2}\frac{f_{\rm FSR}}{\lambda} = -\frac{\partial |G_s|^2}{\partial x}. \tag{B.7}$$

If the cavity gets longer the p-polarized circulating power increases and the s-polarized power decreases, and vice versa.

The power fluctuations in the homodyne power (B.5) due to OMC length fluctuations are thus

$$\frac{\partial P}{\partial x} = \frac{1}{4}(P_{\rm IFO} + P_{\rm LO})(-2)\frac{f_{\rm FSR}}{\lambda}\frac{\delta f_{\rm FSR}}{f_c^2}. \tag{B.8}$$

The power fluctuations in the beet between the LO and signal cancel while the fluctuations in the DC power add. The OMC displacement noise is thus

$$S_P^{1/2} = \frac{P_{\rm IFO} + P_{\rm LO}}{2}\frac{f_{\rm FSR}}{\lambda}\frac{\delta f_{\rm FSR}}{f_c^2} S_x^{1/2}. \tag{B.9}$$

B.4 Noise with the half-wave plate after the OMC

With the HWP after the OMC the field incident on the second PBS is

$$E = \frac{1}{\sqrt{2}}\left(G_p E_{\rm IFO} - G_s E_{\rm LO} e^{i\zeta}\right)\hat{\mathbf{p}} + \frac{1}{\sqrt{2}}\left(G_p E_{\rm IFO} + G_s E_{\rm LO} e^{i\zeta}\right)\hat{\mathbf{s}} \tag{B.10}$$

and the homodyne signal is thus

$$P = \sqrt{P_{\rm IFO} P_{\rm LO}}\,|G_p||G_s|\cos(\zeta + \Delta\phi). \tag{B.11}$$

where $\Delta\phi = \phi_s - \phi_p$. As with the case above, power fluctuations in s and p due to length fluctuations cancel.

However, since s and p have different cavity finesse, the phase change due to cavity length fluctuations is different:

$$\frac{\partial \phi}{\partial x} = \frac{2\mathcal{F}}{\pi}\frac{2\pi}{\lambda} \qquad \Rightarrow \qquad \frac{\partial \Delta\phi}{\partial x} = \frac{4\delta\mathcal{F}}{\lambda} \tag{B.12}$$

where $\delta\mathcal{F} = \mathcal{F}_s - \mathcal{F}_p$. The noise is thus

$$S_P^{1/2} = \sqrt{P_{\mathrm{IFO}} P_{\mathrm{LO}}}\, \frac{4\delta\mathcal{F}}{\lambda} |\sin\zeta| S_x^{1/2}. \tag{B.13}$$

This noise could be significant if P_{IFO} as a large contrast defect component. This noise is largest when reading out the phase quadrature since the LO and CD are orthogonal. However, there is no displacement noise when reading out the amplitude quadrature. In this case the LO and CD are aligned and so there is no first order change in the rates of rotation for the s- and p-polarizations.

B.5 Noise with half-wave plates on both sides of the OMC

Since it is only necessary that there is a net $\pi/4$ polarization rotation before the second PBS, it is possible to us a HWP before the OMC that rotates the polarizations by θ and a second HWP after the OMC which rotates the polarizations by $\varphi = \pi/4 - \theta$. In this case, the fields after the PBS are

$$\begin{bmatrix} E_A \\ E_B \end{bmatrix} = \frac{1}{\sqrt{2}} \begin{bmatrix} \cos\theta + \sin\theta & \sin\theta - \cos\theta \\ \cos\theta - \sin\theta & \cos\theta + \sin\theta \end{bmatrix} \begin{bmatrix} G_p \cos\theta & -G_p \sin\theta \\ G_s \sin\theta & G_s \cos\theta \end{bmatrix} \begin{bmatrix} E_{\mathrm{IFO}} \\ E_{\mathrm{LO}} \mathrm{e}^{\mathrm{i}\zeta} \end{bmatrix} \tag{B.14}$$

where the top component is p and the bottom component is s. In this case it can be shown that $P = P_1 + P_2$ where

$$\begin{aligned} P_1 = \frac{1}{8}[&(\sin 4\theta - 2\sin 2\theta)(|G_p|^2 P_{\mathrm{LO}} - |G_s|^2 P_{\mathrm{IFO}}) \\ &+ (\sin 4\theta + 2\sin 2\theta)(|G_s|^2 P_{\mathrm{LO}} - |G_p|^2 P_{\mathrm{IFO}})] - \frac{1}{4}\sin 4\theta\, |G_p||G_s|(P_{\mathrm{LO}} - P_{\mathrm{IFO}})\cos\Delta\phi \end{aligned} \tag{B.15a}$$

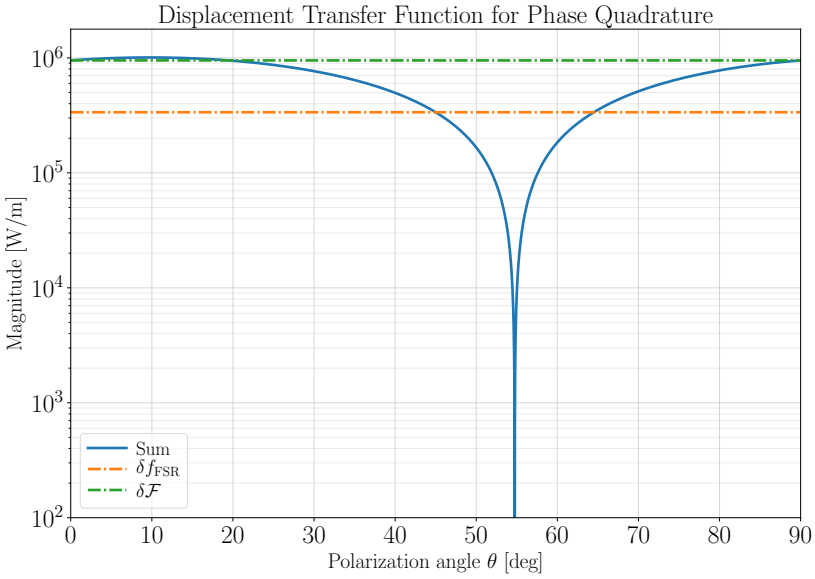

Figure B.4: OMC sensitivity to displacement noise when the phase quadrature ($\zeta = \pi/2$) is readout. The parameters for the aLIGO OMCs are used with $P_{\mathrm{LO}} = 10\,\mathrm{mW}$ and $P_{\mathrm{CD}} = 1\,\mathrm{mW}$. The line marked δf_{FSR} is the sensitivity due to the FSR difference which would be obtained if a single HWP is placed before the OMC ($\theta = \pi/4$). The line marked $\delta\mathcal{F}$ is the sensitivity due to the finesse difference which would be obtained if a single HWP is placed after the OMC ($\theta = 0$).

and

$$P_2 = \frac{1}{2}\sqrt{P_{\mathrm{LO}}P_{\mathrm{IFO}}}\{\sin^2 2\theta\,(|G_s|^2 + |G_p|^2)\cos\zeta + 2|G_s||G_p|\cos 2\theta\big[\cos^2\theta\cos(\zeta+\Delta\phi) - \sin^2\theta\cos(\zeta-\Delta\phi)\big]\}. \quad \text{(B.15b)}$$

Note that when $|G_s| = |G_p| = 1$ and $\Delta\phi = 0$, $P_1 = 0$ and $P_2 = \sqrt{P_{\mathrm{LO}}P_{\mathrm{IFO}}}\cos\zeta$ regardless of θ, as it should.

The length fluctuations of these terms are

$$\frac{\partial P_1}{\partial x} = -\frac{1}{2}\frac{f_{\mathrm{FSR}}}{\lambda}\frac{\delta f_{\mathrm{FSR}}}{f_c^2}(P_{\mathrm{LO}} + P_{\mathrm{IFO}})\sin 2\theta \quad \text{(B.16a)}$$

$$\frac{\partial P_2}{\partial x} = -\sqrt{P_{\mathrm{IFO}}P_{\mathrm{LO}}}\frac{4\delta\mathcal{F}}{\lambda}\cos 2\theta\sin\zeta \quad \text{(B.16b)}$$

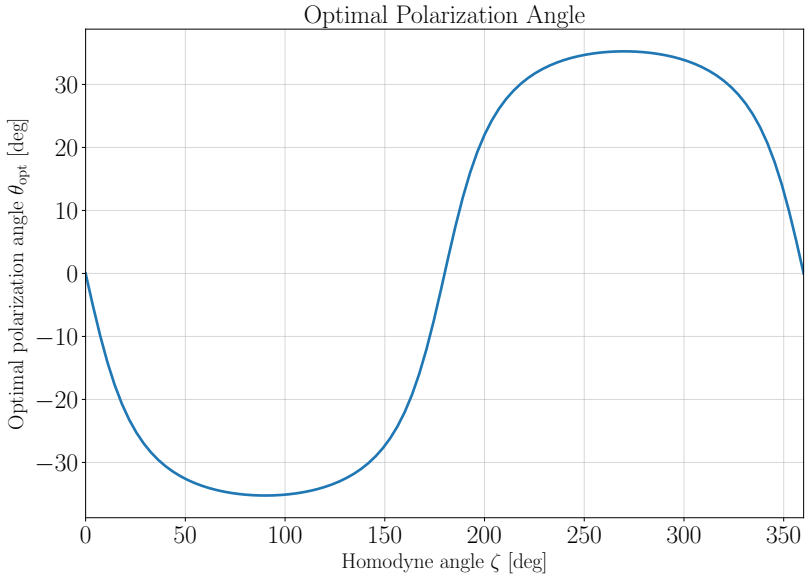

Figure B.5: Optimal polarization angle for an aLIGO OMC with $P_{\mathrm{LO}} = 10\,\mathrm{mW}$ and $P_{\mathrm{CD}} = 1\,\mathrm{mW}$.

and so the total displacement noise is

$$S_P^{1/2} = \left| \frac{1}{2}(P_{\mathrm{LO}} + P_{\mathrm{IFO}}) \frac{f_{\mathrm{FSR}}}{\lambda} \frac{\delta f_{\mathrm{FSR}}}{f_c^2} \sin 2\theta + \sqrt{P_{\mathrm{LO}} P_{\mathrm{IFO}}} \frac{4\delta\mathcal{F}}{\lambda} \sin\zeta \cos 2\theta \right| S_x^{1/2}. \tag{B.17}$$

It is thus possible to cancel the displacement noise by choosing the polarization angle appropriately. In the case that the interferometer beam is dominated by contrast defect P_{CD} and $P_{\mathrm{LO}} \gg P_{\mathrm{CD}}$, the optimal angle is

$$\theta_{\mathrm{opt}} = -\frac{1}{2} \arctan\left(\sqrt{\frac{P_{\mathrm{CD}}}{P_{\mathrm{LO}}}} \frac{8\delta\mathcal{F}}{f_{\mathrm{FSR}}} \frac{f_c^2}{\delta f_{\mathrm{FSR}}} \sin\zeta \right). \tag{B.18}$$

Note that the angle is $\pi/2$ periodic.

For the aLIGO OMCs, $\delta\mathcal{F} \approx 80$, $\delta f_{\mathrm{FSR}} \approx 30\,\mathrm{kHz}$, $f_{\mathrm{FSR}} \approx 268\,\mathrm{MHz}$, and $f_c \approx 340\,\mathrm{kHz}$. The coatings can presumably be designed to minimize the birefringence, but for concreteness the sensitivity of the OMC to displacement noise $S_P^{1/2}/S_x^{1/2}$ when the phase quadrature $\zeta = \pi/2$ is readout is shown in Fig. B.4 for aLIGO parameters. The optimal rotation angle as a function of homodyne angle is plotted in Fig. B.5.

Appendix C

Compact Binary Waveforms for Combined Networks of Ground and Space Detectors

Analyzing the gravitational wave signal from a single source with a network of both ground and space detectors is challenging for a few reasons. First, since the space detectors are sensitive to lower frequencies than the ground detectors, the signals will stay in the space detectors' sensitivity band longer than the ground detectors' band; see Fig. C.1 below. While the signal from a ground detector can be computed by projecting the gravitational wave signal onto the antenna pattern for that detector at the time the wave hits the detector, space detectors have to account for the Doppler shift of the wave's frequency as well as the changing antenna pattern caused by the motion of the detector in its orbit. Sec. C.1 gives rough estimates for the timescales over which these time dependent effects are important.

Second, since the waves will often merge in the ground detectors' band, the merger and ringdown must be computed in addition to the inspiral. Waveforms used for low frequency missions such as LISA or TianQin, see for example [49, 118–120], include only the inspiral, and the current methods of calculating high frequency waveforms that include the merger and ringdown do not include the time dependent effects necessary for

the low frequencies.

Finally, on a more practical level, since the low frequency waveforms last for so long, it is impractical to compute them with linearly spaced frequency points as is currently done for these high frequency waveforms. Any attempt to add the time dependence to the high frequency waveforms will be further complicated by the need to generate the waveforms at logarithmically spaced frequency points. One approach is generate the waveforms in two pieces: a high frequency linearly spaced waveform, and a low frequency logarthmically spaced waveform with Doppler shifts and time dependent antenna patterns built in. These two waveforms could then be joined, though this is difficult to achieve in practice.

For a detector such as TianGO, which is sensitive to an intermediate frequency band where a source will both spend a significant amount of time and merge, it is especially important to account for both the merger and ringdown as well as the time dependence and Doppler shifts.

This appendix describes such a waveform that can be simultaneously used for both ground and space detectors. Sec. C.2 describes the basic waveform from Refs. [121, 122]. Sec. C.3 then describes the projection of this basic waveform onto ground detectors, and Sec. C.4 describes how the waveform used to analyze low frequency LISA signals from Ref. [49] can be modified to project the waveform from Sec. C.2 onto a space detector. Since the waveform is analytic, it is also straightforward to evaluate at logarithmically spaced frequency points.

Throughout this appendix the following mass quantities are used. The mass of each binary in the compact binary system is M_1 and M_2, and the total mass of the system is $M = M_1 + M_2$. The reduced mass is $\mu = M_1 M_2 / M$ and the symmetric mass ratio is

$\eta = M_1 M_2 / M^2$. The chirp mass is

$$\mathcal{M} = \mu^{3/5} M^{2/5} = \eta^{3/5} M. \tag{C.1}$$

C.1 Time Dependent Effects of Low Frequency Waveforms

The time it takes a binary system to coalesce from the time it is at the frequency f is [123]

$$\tau = \frac{1}{\pi^{8/3}} \frac{5}{256} \left(\frac{G M_\odot}{c^3} \right)^{-5/3} \left(\frac{\mathcal{M}}{M_\odot} \right)^{-5/3} f^{-8/3} \tag{C.2}$$

Less massive systems therefore merge slower than more massive systems. If the frequency at which a gravitational wave enters a detector's band is sufficiently low, the time until merger will be sufficiently long that Doppler shifts and time dependent antenna patterns will need to be accounted for. In this section we give estimates for when these effects become important.

Doppler shift This estimate for the magnitude of the Doppler shifts follows Ref. [123]. For a gravitational wave of frequency $f_{\rm gw}$, the observed frequency in a detector moving with velocity $\mathbf{v}$ with respect to the source is

$$f = f_{\rm gw} \left(1 + \frac{\mathbf{v} \cdot \hat{\mathbf{r}}}{c} \right), \tag{C.3}$$

where $\hat{\mathbf{r}}$ is the unit vector in the direction of the source. Therefore, the change in frequency over a time T is $\Delta f = f_{\rm gw} \Delta v / c$ where Δv is the change in velocity in the direction of the source over this time. Let the rotational velocity of the detector be $v_{\rm rot} = R \omega_{\rm rot}$ where R is the radius of the orbit. If we are considering the rotation of the detector around the sun then $R = R_\odot$, and if we are consider the rotation of the earth around its axis

$R = R_\oplus$. These estimates are in the worst case where the detector is at the equator and facing the source head on. The change in angle of the detector around the axis of rotation is $\Delta\theta = T\omega_{\rm rot}$. If $\Delta\theta \ll 1$

$$\Delta v \sim v_{\rm rot}\Delta\theta \sim T v_{\rm rot}\omega_{\rm rot} \sim R\omega_{\rm rot}^2 T. \tag{C.4}$$

If the source is observed for a time T, then the frequency resolution is $\Delta f = 1/T$. The Doppler shift is not important if the frequency shift due to the Doppler effect is less than this frequency resolution:

$$f_{\rm gw} R\frac{\omega_{\rm rot}^2}{c} T \lesssim \frac{1}{T} \tag{C.5}$$

or

$$T \lesssim \frac{1}{\omega_{\rm rot}}\sqrt{\frac{c}{f_{\rm gw}R}}. \tag{C.6}$$

For the rotation of the Earth about its axis, this is

$$T_\oplus \lesssim 50\,{\rm min}\,\sqrt{\frac{1\,{\rm kHz}}{f_{\rm gw}}}, \tag{C.7}$$

and for the rotation a detector around the sun, this is

$$T_\odot \lesssim 120\,{\rm min}\,\sqrt{\frac{1\,{\rm kHz}}{f_{\rm gw}}}. \tag{C.8}$$

There is a distance between two binaries beyond which no stable orbit exists. This orbit is called the innermost stable circular orbit (ISCO) and occurs at a frequency of

$$f_{\rm ISCO} = \frac{1}{12\sqrt{6}\pi}\left(\frac{c^3}{GM_\odot}\right)\left(\frac{M_\odot}{M_{\rm tot}}\right). \tag{C.9}$$

This is roughly the frequency at which the merger occurs and, since the gravitational wave frequency is twice the orbital frequency, the maximum frequency observed in a detector that sees the merger and ringdown is a little more than $f_{\rm gw} = 2f_{\rm ISCO}$. This is the value that should be used in the estimates in (C.6).

f	$M_{\rm tot}/M_\odot$	τ	$2f_{\rm ISCO}$	$T_\odot$	$T_\oplus$	$\lvert\delta F/F\rvert_\odot$	$\lvert\delta F/F\rvert_\oplus$
10 Hz	8	170 s	550 Hz	160 min	67 min	7.3×10^{-5}	2.6×10^{-2}
10 Hz	80	3.8 s	55 Hz	8.5 hr	3.6 hr	1.5×10^{-6}	5.6×10^{-4}
10 Hz	800	81 ms	5.5 Hz	27 hr	11.2 hr	3.2×10^{-8}	1.2×10^{-5}
10 mHz	8	550 yr	550 Hz	160 min	67 min	1	1
10 mHz	80	11.9 yr	55 Hz	8.5 hr	3.6 hr	1	1
10 mHz	800	95 days	5.5 Hz	27 hr	11.2 hr	1	1

Table C.1: Importance of Doppler shifts and time dependent antenna patterns. The time to coalescence τ is for the frequency f in the table, the maximum allowable times in band $T_{\odot,\oplus}$ are for $2f_{\rm ISCO}$, and the magnitude of the relative antenna pattern change $|\delta F/F|_{\odot,\oplus}$ are for the duration τ. As described in the text, for Doppler shifts to be unimportant $\tau < T_\odot, T_\oplus$, and for antenna pattern variations to be unimportant $|\delta F/F|_{\odot,\oplus} \ll 1$. The time dependent effects are thus negligible for ground detectors with sources entering their sensitivity band around 10 Hz, but are significant for space detectors with sources entering their sensitivity bands extending down to 10 mHz or lower.

Amplitude modulation The antenna patterns for the plus and cross polarizations are

$$F_+ = \frac{1}{2}\big(1+\cos^2\theta\big)\cos 2\phi, \qquad F_\times = \cos\theta \sin 2\phi \tag{C.10}$$

For the rest of this estimate we take the maximum amplitude to get the worst case amplitude modulation. The maximum values of the rate of change of these amplitudes is

$$\left|\dot{F}_+\right| = \left|\dot{F}_\times\right| = 2\dot{\phi} = 2\omega_{\rm rot} \tag{C.11}$$

and the change in the amplitudes during a time T is $\delta F_{+,\times} = \dot{F}_{+,\times} T$. The maximum value of the relative intensities is thus

$$\left|\frac{\delta F_+}{F_+}\right|_{\rm max} = \left|\frac{\delta F_\times}{F_\times}\right|_{\rm max} \sim 2\omega_{\rm rot} T. \tag{C.12}$$

For the rotation of the Earth about its axis this is

$$\left|\frac{\delta F}{F}\right|_{\rm max,\oplus} \sim 1.5\times10^{-4}\,\frac{T}{1\,{\rm s}}, \tag{C.13}$$

and for the rotation of the detector about the sun this is

$$\left|\frac{\delta F}{F}\right|_{\max,\odot} \sim 4\times 10^{-7}\,\frac{T}{1\,\mathrm{s}} \sim 2.4\times 10^{-5}\,\frac{T}{1\,\mathrm{min}}. \tag{C.14}$$

Tab. C.1 shows the estimates of the importance of Doppler shifts and time dependent antenna patterns for various sources as detected in a ground or space detector. It is assumed that the detector sees the source for the entire frequency band from f to $2f_{\mathrm{ISCO}}$. As the table shows, the effects described in this section are significant for space detectors but not for ground detectors. These effects may start to become important for the third generation of ground based gravitational wave detectors which will be sensitive to lower frequencies, however.

C.2 Basic Waveform

The waveform described in Refs. [121, 122] is an analytic phenomenological waveform found by matching a numerical relativity waveform with a post Newtonian wave form. It is written in the frequency domain as

$$u(f) = A_{\mathrm{eff}}(f)\,\mathrm{e}^{\mathrm{i}\Psi_{\mathrm{eff}}(f)} \tag{C.15}$$

where the amplitude is broken up into an inspiral, merger, and ringdown phase:

$$A_{\mathrm{eff}}(f) = C\begin{cases} (f/f_{\mathrm{merg}})^{-7/6} & f < f_{\mathrm{merg}} \\ (f/f_{\mathrm{merg}})^{-2/3} & f_{\mathrm{merg}} < f < f_{\mathrm{ring}} \\ w\mathcal{L}(f, f_{\mathrm{ring}}, \sigma) & f_{\mathrm{ring}} < f < f_{\mathrm{cut}} \end{cases}. \tag{C.16}$$

The ringdown is described by a Lorentzian of width σ centered on the ringdown frequency f_{ring}

$$\mathcal{L}(f, f_{\mathrm{ring}}, \sigma) = \frac{1}{2\pi}\frac{\sigma}{(f - f_{\mathrm{ring}})^2 + \sigma^2/4}, \tag{C.17}$$

Quantity	a_k	b_k	c_k
$f_{\rm ring}$	5.9411×10^{-1}	8.9794×10^{-2}	1.9111×10^{-1}
$f_{\rm merg}$	2.9740×10^{-1}	4.4810×10^{-2}	9.5560×10^{-2}
$f_{\rm cut}$	8.4845×10^{-1}	1.2848×10^{-1}	2.7299×10^{-1}
σ	5.0801×10^{-1}	7.7515×10^{-2}	2.2369×10^{-2}

Table C.2: Parameters for waveform frequencies and Lorentzian width.

and

$$w = \frac{\pi\sigma}{2}\left(\frac{f_{\rm ring}}{f_{\rm merg}}\right) \tag{C.18}$$

is chosen to make the waveform continuous at the transition between the merger and ringdown. The overall amplitude is

$$C = \sqrt{\frac{5}{24}}\frac{c^{1/6}}{\pi^{2/3}D_L}\left(\frac{GM_\odot}{c^2}\right)^{5/6}\left(\frac{\mathcal{M}}{M_\odot}\right)^{5/6} f_{\rm merg}^{-7/6}. \tag{C.19}$$

where $\mathcal{M}$ is the chirp mass and D_L is the luminosity distance.

The merger, ringdown, and cutoff frequencies as well as the Lorentzian width are given by matching to a numerical relativity waveform. If $\alpha_1 = f_{\rm merg}$, $\alpha_2 = f_{\rm ring}$, $\alpha_3 = f_{\rm cut}$, and $\alpha_4 = \sigma$, the parameters are

$$\alpha_k = \frac{c^3}{\pi G M_\odot}\left(\frac{M_\odot}{M}\right)\left(a_k\eta^2 + b_k\eta + c_k\right), \tag{C.20}$$

where the constants a_k, b_k, and c_k are given in Tab. C.2

The phase is

$$\Psi_{\rm eff}(f) = 2\pi f t_0 + \psi_0 + \sum_{k=0}^{7}\psi_k f^{(k-5)/3} \tag{C.21}$$

where

$$\psi_k = \frac{1}{\eta}\left(\frac{c^3}{\pi G M_\odot}\right)^{(5-k)/3}\left(\frac{M}{M_\odot}\right)^{(k-5)/3}(x_k\eta^2 + y_k\eta + z_k). \tag{C.22}$$

The phase parameters are given in Tab. C.3.

k	x_k	y_k	z_k
0	1.7516×10^{-1}	7.9483×10^{-2}	-7.2390×10^{-2}
1	0	0	0
2	-5.1571×10^{1}	-1.7595×10^{1}	1.3253×10^{1}
3	6.5866×10^{2}	1.7803×10^{2}	-1.5972×10^{2}
4	-3.9031×10^{3}	-7.7493×10^{2}	8.8195×10^{2}
5	0	0	0
6	-2.4874×10^{4}	-1.4892×10^{3}	4.4588×10^{3}
7	2.5196×10^{4}	3.3970×10^{2}	-3.9573×10^{3}

Table C.3: Parameters for waveform phase.

C.3 Projection onto Ground Detectors

Projecting the gravitational wave signal (C.15) onto a ground detector is relatively straightforward since the detector itself can be treated as fixed in time. We use (C.15) to write the plus and cross polarizations as [123]

$$h_+(f) = A_{\rm eff}(f)\, \mathrm{e}^{\mathrm{i}\Psi_{\rm eff}(f)} \left(\frac{1+\cos^2\iota}{2}\right) \tag{C.23a}$$

$$h_\times(f) = A_{\rm eff}(f)\, \mathrm{e}^{\mathrm{i}[\Psi_{\rm eff}(f)+\pi/2]}\, \cos\iota, \tag{C.23b}$$

where ι is the source inclination. The antenna patterns for an interferometer are

$$F_+ = \left(\frac{1+\cos^2\theta}{2}\right) \cos 2\phi \cos 2\psi - \cos\theta \sin 2\phi \sin 2\psi \tag{C.24a}$$

$$F_\times = \left(\frac{1+\cos^2\theta}{2}\right) \cos 2\phi \sin 2\psi + \cos\theta \sin 2\phi \cos 2\psi, \tag{C.24b}$$

where ϕ and θ are the azimuthal and polar angles, respectively, of the source relative to the detector and ψ is the polarization phase. Instead of ϕ and θ, right ascension $\alpha = \phi$ and declination $\delta = \pi/2 - \theta$ are often used. The waveform observed in a given detector is then

$$h(f) = F_+ h_+(f) + F_\times h_\times(f). \tag{C.25}$$

C.4 Projection onto Space Detectors

We follow the approach of Ref. [49] to modify the waveform (C.15) to account for the Doppler shifts and the time dependence of the space detector antenna pattern. The strategy to account for the time dependence is to find the source location in the frame of the detector as a function of time. The source location relative to the ecliptic plane ϕ, θ, and ψ is fixed and the location in the detector frame $\tilde{\phi}(t), \tilde{\theta}(t)$, and $\tilde{\psi}(t)$ is a function of time. Once these angles are known, they are used to calculate the Doppler shift and the antenna patterns (C.24) as a function of time. Finally, a post-Newtonian expansion is used to find the frequency of the waveform as a function of time so that the waveform can be written in the frequency domain.

The post-Newtonian expansion is done in the parameter [49, 114]

$$x = \left(\frac{G}{c^3}\pi M_\odot\right)^{2/3} \frac{\mathcal{M}}{\mu}\left[\left(\frac{\mathcal{M}}{M_\odot}\right) f\right]^{2/3}. \tag{C.26}$$

The time as a function of frequency is

$$t_f = t_c - t_x\left[1 + \frac{4}{3}\left(\frac{743}{336} + \frac{11}{4}\frac{\mu}{M}\right)x - \frac{32\pi}{5}x^{3/2}\right], \tag{C.27}$$

where t_c is the coalescence time and

$$t_x = 5c^{5/3}(8\pi f)^{-8/3}\left(\frac{GM_\odot}{c^2}\right)^{-5/3}\left(\frac{\mathcal{M}}{M_\odot}\right)^{-5/3}. \tag{C.28}$$

Now we summarize the time dependence of the source location [49]. The azimuthal angle of the detector in its orbit around the sun is $\bar{\phi}(t_f) = 2\pi t_f/T$ where T is the period of the orbit. Let $\hat{\mathbf{n}}$ be the unit vector from the detector to the source and let $\hat{\mathbf{L}}$ be the unit vector of the source angular momentum in the ecliptic frame. The azimuthal and polar angles of the angular momentum are ϕ_L and θ_L, respectively. If $\hat{\mathbf{z}}$ is the unit vector along the z direction, the polar angle of the source in the detector frame is

$$\cos\tilde{\theta}(t_f) = \hat{\mathbf{z}}\cdot\hat{\mathbf{n}} = \frac{1}{2}\cos\theta - \frac{\sqrt{3}}{2}\sin\theta\cos(\bar{\phi}(t_f) - \phi), \tag{C.29}$$

the azimuthal angle of the source in the detector frame is

$$\tilde{\phi}(t_f) = \bar{\phi}(t_f) + \arctan\left[\frac{\sqrt{3}\cos\theta + \sin\theta\cos(\bar{\phi}(t_f) - \phi)}{2\sin\theta\sin(\bar{\phi}(t_f) - \phi)}\right], \tag{C.30}$$

and the polarization phase of the source in the detector frame is

$$\tan\tilde{\psi}(t_f) = \frac{\hat{\mathbf{L}}\cdot\hat{\mathbf{z}} - (\hat{\mathbf{L}}\cdot\hat{\mathbf{n}})(\hat{\mathbf{z}}\cdot\hat{\mathbf{n}})}{\hat{\mathbf{n}}\cdot(\hat{\mathbf{L}}\times\hat{\mathbf{z}})} \tag{C.31}$$

where

$$\hat{\mathbf{L}}\cdot\hat{\mathbf{z}} = \frac{1}{2}\cos\theta_L - \frac{\sqrt{3}}{2}\sin\theta_L\cos(\bar{\phi}(t_f) - \phi_L) \tag{C.32}$$

$$\hat{\mathbf{L}}\cdot\hat{\mathbf{n}} = \cos\theta_L\cos\theta + \sin\theta_L\sin\theta\cos(\phi_L - \phi), \tag{C.33}$$

and

$$\begin{aligned}\hat{\mathbf{n}}\cdot(\hat{\mathbf{L}}\times\hat{\mathbf{z}}) = {}& \frac{1}{2}\sin\theta_L\sin\theta\sin(\phi_L - \phi) \\ & - \frac{\sqrt{3}}{2}\cos\bar{\phi}(t_f)\left(\cos\theta_L\sin\theta\sin\phi - \cos\theta\sin\theta_L\sin\phi_L\right) \\ & - \frac{\sqrt{3}}{2}\sin\bar{\phi}(t_f)\left(\cos\theta\sin\theta_L\sin\phi_L - \cos\theta_L\sin\theta\sin\phi\right).\end{aligned} \tag{C.34}$$

Eqs. (C.29)–(C.31) are a function of frequency through (C.27).

The antenna patterns as a function of time are given by plugging the detector frame angles (C.29)–(C.31) into (C.24). The amplitude of the waveform in the detector is modulated by

$$\Lambda(f) = \sqrt{[1 + (\hat{\mathbf{L}}\cdot\hat{\mathbf{n}})^2]^2 F_+^2(f) + 4(\hat{\mathbf{L}}\cdot\hat{\mathbf{n}})^2 F_\times^2(f)} \tag{C.35}$$

as the detector orbits the sun. The time dependence of the antenna pattern also adds the additional polarization phase

$$\tan\phi_p(f) = \frac{2(\hat{\mathbf{L}}\cdot\hat{\mathbf{n}})F_\times(f)}{[1 + (\hat{\mathbf{L}}\cdot\hat{\mathbf{n}})^2]F_+(f)} \tag{C.36}$$

to the overall phase. Finally, the motion of the detector around the sun Doppler shifts the wave's frequency and adds the additional phase

$$\phi_D(f) = \frac{2\pi f}{c} R\sin\theta\cos(\bar{\phi}(t_f) - \phi) \tag{C.37}$$

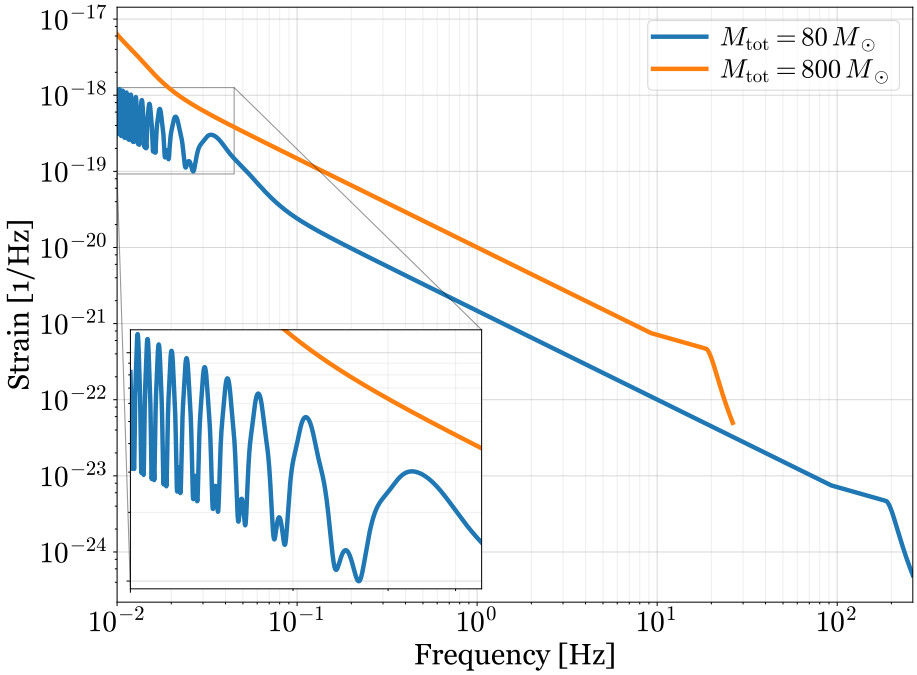

Figure C.1: Amplitude of the waveform (C.38) for two equal mass binary systems at a redshift of $z = 0.1$. The legend denotes the total mass of the binary system. The time the $80\,M_\odot$ binary stays in the zoomed in region of the plot is approximately 11.7 years. In contrast, the time it takes the $800\,M_\odot$ binary to sweep through the same frequency band (of approximately 35 mHz) is approximately 3 months.

where R is the radius of the orbit.

The full waveform projected onto the space detector's time-dependent antenna pattern and accounting for the Doppler shift is

$$h(f) = \frac{\sqrt{3}}{2}\Lambda(f)A_{\rm eff}(f)\,{\rm e}^{{\rm i}[\Psi_{\rm eff}(f)-\phi_D(f)-\phi_p(f)]}. \tag{C.38}$$

The factor of $\sin(\pi/3) = \sqrt{3}/2$ accounts for a detector forming an equilateral triangle: the antenna patterns for an interferometer with arms at 60° is $\sin(\pi/3)$ times those for an interferometer with perpendicular arms.

Finally, note that this projection onto a space detector is most convenient in terms of the source location θ and ϕ in the ecliptic frame and the orientation of the source angular momentum θ_L and ϕ_L, while calculations are more commonly done in terms of the

inclination ι and polarization phase ψ. The relation between the two parameterizations is given by

$$\cos\iota = \cos\theta_L \sin\delta + \sin\theta_L \cos\delta \cos(\phi_L - \alpha) \tag{C.39}$$

$$\tan\psi = \frac{\cos\theta_L + \cos\iota \sin\delta}{\cos\delta \sin\theta_L \sin(\phi_L - \alpha)} \tag{C.40}$$

where $\alpha = \phi$ is the right ascension and $\delta = \pi/2 - \theta$ is the declination of the source.

Bibliography

[1] LIGO Scientific Collaboration, *Advanced LIGO*, *Classical and Quantum Gravity* **32** (2015), no. 7 074001.

[2] Virgo Collaboration, *Advanced virgo: a second-generation interferometric gravitational wave detector*, *Classical and Quantum Gravity* **32** (dec, 2015) 024001.

[3] LIGO Scientific Collaboration and Virgo Collaboration, *Observation of gravitational waves from a binary black hole merger*, *Phys. Rev. Lett.* **116** (Feb, 2016) 061102.

[4] LIGO Scientific Collaboration and Virgo Collaboration, *GW170817: Observation of gravitational waves from a binary neutron star inspiral*, *Phys. Rev. Lett.* **119** (Oct, 2017) 161101.

[5] LIGO Scientific Collaboration and Virgo Collaboration, *GWTC-1: A Gravitational-Wave Transient Catalog of Compact Binary Mergers Observed by LIGO and Virgo during the First and Second Observing Runs*, arXiv:1811.1290.

[6] Y. Aso, Y. Michimura, K. Somiya, M. Ando, O. Miyakawa, T. Sekiguchi, D. Tatsumi, and H. Yamamoto, *Interferometer design of the KAGRA gravitational wave detector*, *Phys. Rev. D* **88** (Aug, 2013) 043007.

[7] C. Affeldt, K. Danzmann, K. L. Dooley, H. Grote, M. Hewitson, S. Hild, J. Hough, J. Leong, H. Lck, M. Prijatelj, S. Rowan, A. Rdiger, R. Schilling, R. Schnabel, E. Schreiber, B. Sorazu, K. A. Strain, H. Vahlbruch, B. Willke, W. Winkler, and H. Wittel, *Advanced techniques in GEO 600*, *Classical and Quantum Gravity* **31** (nov, 2014) 224002.

[8] R. X. Adhikari, N. Smith, A. Brooks, L. Barsotti, B. Shapiro, B. Lantz, D. McClelland, E. K. Gustafson, D. V. Martynov, V. Mitrofanov, D. Coyne, K. Arai, C. Torrie, and C. Wipf, *LIGO voyager upgrade: Design concept*, Tech. Rep. LIGO-T1400226, 2018.

[9] LIGO Scientific Collaboration, *Exploring the sensitivity of next generation gravitational wave detectors*, *Classical and Quantum Gravity* **34** (2017), no. 4 044001.

[10] S. Dwyer, D. Sigg, S. W. Ballmer, L. Barsotti, N. Mavalvala, and M. Evans, *Gravitational wave detector with cosmological reach*, *Phys. Rev. D* **91** (Apr, 2015) 082001.

[11] S. Hild, et al., *Sensitivity studies for third-generation gravitational wave observatories*, *Classical and Quantum Gravity* **28** (2011), no. 9 094013.

[12] M. Punturo, et al., *The third generation of gravitational wave observatories and their science reach*, *Classical and Quantum Gravity* **27** (2010), no. 8 084007.

[13] M. Punturo, et al., *The Einstein Telescope: a third-generation gravitational wave observatory*, *Classical and Quantum Gravity* **27** (2010), no. 19 194002.

[14] *LISA system and technology study report*, 2000.

[15] J. Luo, L.-S. Chen, H.-Z. Duan, Y.-G. Gong, S. Hu, J. Ji, Q. Liu, J. Mei, V. Milyukov, M. Sazhin, C.-G. Shao, V. T. Toth, H.-B. Tu, Y. Wang, Y. Wang, H.-C. Yeh, M.-S. Zhan, Y. Zhang, V. Zharov, and Z.-B. Zhou, *Tianqin: a space-borne gravitational wave detector*, *Classical and Quantum Gravity* **33** (2016), no. 3 035010.

[16] S. Sato, *The status of DECIGO*, *Journal of Physics: Conference Series* **840** (2017), no. 1 012010.

[17] N. Seto, S. Kawamura, and T. Nakamura, *Possibility of direct measurement of the acceleration of the universe using 0.1 hz band laser interferometer gravitational wave antenna in space*, *Phys. Rev. Lett.* **87** (Nov, 2001) 221103.

[18] T. Corbitt, Y. Chen, F. Khalili, D. Ottaway, S. Vyatchanin, S. Whitcomb, and N. Mavalvala, *Squeezed-state source using radiation-pressure-induced rigidity*, *Phys. Rev. A* **73** (Feb, 2006) 023801.

[19] K. Arai, G. Venugopalan, A. Markowitz, K. Kuns, A. Wade, and R. Adhikari, *Some thoughts on polarization BHD*, Tech. Rep. LIGO-G1802013, 2018.

[20] C. C. Gerry and P. L. Knight, *Introductory Quantum Optics*. Cambridge University Press, Cambridge, 2005.

[21] L. Mandel and E. Wolf, *Optical Coherence and Quantum Optics*. Cambridge University Press, Cambridge, 1995.

[22] C. Cohen-Tannoudji, J. Dupont-Roc, and G. Grynberg, *Photons and Atoms: Introduction to Quantum Electrodynamics*. Wiley Science Paperback Series. John Wiley and Sons, Inc., New York, 1989.

[23] C. M. Caves and B. L. Schumaker, *New formalism for two-photon quantum optics. i. quadrature phases and squeezed states*, *Phys. Rev. A* **31** (May, 1985) 3068–3092.

[24] B. L. Schumaker and C. M. Caves, *New formalism for two-photon quantum optics. ii. mathematical foundation and compact notation*, *Phys. Rev. A* **31** (May, 1985) 3093–3111.

[25] H. J. Kimble, Y. Levin, A. B. Matsko, K. S. Thorne, and S. P. Vyatchanin, *Conversion of conventional gravitational-wave interferometers into quantum nondemolition interferometers by modifying their input and/or output optics*, *Phys. Rev. D* **65** (Dec, 2001) 022002.

[26] S. L. Danilishin and F. Y. Khalili, *Quantum measurement theory in gravitational-wave detectors*, *Living Reviews in Relativity* **15** (Apr, 2012) 5.

[27] Y. Chen, *Macroscopic quantum mechanics: theory and experimental concepts of optomechanics*, *Journal of Physics B: Atomic, Molecular and Optical Physics* **46** (2013), no. 10 104001.

[28] M. Aspelmeyer, T. J. Kippenberg, and F. Marquardt, *Cavity optomechanics*, *Rev. Mod. Phys.* **86** (Dec, 2014) 1391–1452.

[29] A. Buonanno and Y. Chen, *Signal recycled laser-interferometer gravitational-wave detectors as optical springs*, *Phys. Rev. D* **65** (Jan, 2002) 042001.

[30] H. Rehbein, H. Müller-Ebhardt, K. Somiya, S. L. Danilishin, R. Schnabel, K. Danzmann, and Y. Chen, *Double optical spring enhancement for gravitational-wave detectors*, *Phys. Rev. D* **78** (Sep, 2008) 062003.

[31] C. M. Caves, *Quantum limits on noise in linear amplifiers*, *Phys. Rev. D* **26** (Oct, 1982) 1817–1839.

[32] C. M. Caves, J. Combes, Z. Jiang, and S. Pandey, *Quantum limits on phase-preserving linear amplifiers*, *Phys. Rev. A* **86** (Dec, 2012) 063802.

[33] S. Pandey, Z. Jiang, J. Combes, and C. M. Caves, *Quantum limits on probabilistic amplifiers*, *Phys. Rev. A* **88** (Sep, 2013) 033852.

[34] J. Combes, N. Walk, A. P. Lund, T. C. Ralph, and C. M. Caves, *Models of reduced-noise, probabilistic linear amplifiers*, *Phys. Rev. A* **93** (May, 2016) 052310.

[35] A. Buonanno and Y. Chen, *Quantum noise in second generation, signal-recycled laser interferometric gravitational-wave detectors*, *Phys. Rev. D* **64** (Jul, 2001) 042006.

[36] E. D. Hall, C. Cahillane, K. Izumi, R. J. E. Smith, and R. X. Adhikari, *Systematic calibration error requirements for gravitational-wave detectors via the Cramér-Rao bound*, arXiv:1712.0971.

[37] S. L. Braunstein, C. M. Caves, and G. Milburn, *Generalized uncertainty relations: Theory, examples, and lorentz invariance*, *Annals of Physics* **247** (1996), no. 1 135 – 173.

[38] H. Miao, R. X. Adhikari, Y. Ma, B. Pang, and Y. Chen, *Towards the fundamental quantum limit of linear measurements of classical signals*, *Phys. Rev. Lett.* **119** (Aug, 2017) 050801.

[39] A. Staley, D. Martynov, R. Abbott, R. X. Adhikari, K. Arai, S. Ballmer, L. Barsotti, A. F. Brooks, R. T. DeRosa, S. Dwyer, A. Effler, M. Evans, P. Fritschel, V. V. Frolov, C. Gray, C. J. Guido, R. Gustafson, M. Heintze, D. Hoak, K. Izumi, K. Kawabe, E. J. King, J. S. Kissel, K. Kokeyama, M. Landry, D. E. McClelland, J. Miller, A. Mullavey, B. OReilly, J. G. Rollins, J. R. Sanders, R. M. S. Schofield, D. Sigg, B. J. J. Slagmolen, N. D. Smith-Lefebvre, G. Vajente, R. L. Ward, and C. Wipf, *Achieving resonance in the advanced LIGO gravitational-wave interferometer*, *Classical and Quantum Gravity* **31** (2014), no. 24 245010.

[40] P. Fritschel, M. Evans, and V. Frolov, *Balanced homodyne readout for quantum limited gravitational wave detectors*, *Opt. Express* **22** (Feb, 2014) 4224–4234.

[41] T. Zhang, K. Strain, and S. Hild, *On different mode cleaner arrangements for aLIGO BHD*, Tech. Rep. LIGO-G1800173, 2018.

[42] J. A. Sidles and D. Sigg, *Optical torques in suspended fabryperot interferometers*, *Physics Letters A* **354** (2006), no. 3 167 – 172.

[43] E. Hirose, K. Kawabe, D. Sigg, R. Adhikari, and P. R. Saulson, *Angular instability due to radiation pressure in the LIGO gravitational-wave detector*, *Appl. Opt.* **49** (Jun, 2010) 3474–3484.

[44] K. L. Dooley, L. Barsotti, R. X. Adhikari, M. Evans, T. T. Fricke, P. Fritschel, V. Frolov, K. Kawabe, and N. Smith-Lefebvre, *Angular control of optical cavities in a radiation-pressure-dominated regime: the enhanced LIGO case*, *J. Opt. Soc. Am. A* **30** (Dec, 2013) 2618–2626.

[45] LIGO Scientific Collaboration and Virgo Collaboration, *Tests of general relativity with gw150914*, *Phys. Rev. Lett.* **116** (May, 2016) 221101.

[46] LIGO Scientific Collaboration and Virgo Collaboration, *Tests of General Relativity with GW170817*, arXiv:1811.0036.

[47] M. Vallisneri, *Testing general relativity with gravitational waves: A reality check*, *Phys. Rev. D* **86** (Oct, 2012) 082001.

[48] W. G. Anderson, P. R. Brady, J. D. E. Creighton, and E. E. Flanagan, *Excess power statistic for detection of burst sources of gravitational radiation*, *Phys. Rev. D* **63** (Jan, 2001) 042003.

[49] C. Cutler, *Angular resolution of the LISA gravitational wave detector*, *Phys. Rev. D* **57** (Jun, 1998) 7089–7102.

[50] L. Wen and Y. Chen, *Geometrical expression for the angular resolution of a network of gravitational-wave detectors*, *Phys. Rev. D* **81** (Apr, 2010) 082001.

[51] A. Sesana, *Prospects for multiband gravitational-wave astronomy after gw150914*, *Phys. Rev. Lett.* **116** (Jun, 2016) 231102.

[52] S. Vitale, *Multiband gravitational-wave astronomy: Parameter estimation and tests of general relativity with space- and ground-based detectors*, *Phys. Rev. Lett.* **117** (Jul, 2016) 051102.

[53] Freedman Wendy L., *Cosmology at a crossroads*, *Nature Astronomy* **1** (may, 2017) 0121.

[54] A. G. Riess, L. M. Macri, S. L. Hoffmann, D. Scolnic, S. Casertano, A. V. Filippenko, B. E. Tucker, M. J. Reid, D. O. Jones, J. M. Silverman, R. Chornock, P. Challis, W. Yuan, P. J. Brown, and R. J. Foley, *A 2.4% determination of the local value of the hubble constant*, *The Astrophysical Journal* **826** (2016), no. 1 56.

[55] Planck Collaboration, *Planck 2015 results. XIII. Cosmological parameters*, *Astronomy and Astrophysics* **594** (Sept., 2016) A13, [arXiv:1502.0158].

[56] Schutz Bernard F., *Determining the Hubble constant from gravitational wave observations*, *Nature* **323** (sep, 1986) 310.

[57] K. Kyutoku and N. Seto, *Gravitational-wave cosmography with LISA and the Hubble tension*, *Phys. Rev. D* **95** (Apr, 2017) 083525.

[58] C. Cutler and D. E. Holz, *Ultrahigh precision cosmology from gravitational waves*, *Phys. Rev. D* **80** (Nov, 2009) 104009.

[59] D. E. Holz and S. A. Hughes, *Using gravitational-wave standard sirens*, *The Astrophysical Journal* **629** (2005), no. 1 15.

[60] C. L. MacLeod and C. J. Hogan, *Precision of Hubble constant derived using black hole binary absolute distances and statistical redshift information*, *Phys. Rev. D* **77** (Feb, 2008) 043512.

[61] O. Jennrich, *LISA technology and instrumentation*, *Classical and Quantum Gravity* **26** (2009), no. 15 153001.

[62] D. Gerardi, G. Allen, J. W. Conklin, K.-X. Sun, D. DeBra, S. Buchman, P. Gath, W. Fichter, R. L. Byer, and U. Johann, *Invited article: Advanced drag-free concepts for future space-based interferometers: acceleration noise performance*, *Review of Scientific Instruments* **85** (2014), no. 1 011301, [https://doi.org/10.1063/1.4862199].

[63] W. J. Weber, A. Cavalleri, R. Dolesi, G. Fontana, M. Hueller, and S. Vitale, *Position sensors for LISA drag-free control*, *Classical and Quantum Gravity* **19** (2002), no. 7 1751.

[64] J. C. Amato, *Flying in formation: The orbital dynamics of LISA's three spacecraft*, *American Journal of Physics* **87** (2019), no. 1 18–23, [https://doi.org/10.1119/1.5075722].

[65] S. V. Dhurandhar, K. R. Nayak, S. Koshti, and J.-Y. Vinet, *Fundamentals of the LISA stable flight formation*, *Classical and Quantum Gravity* **22** (2005), no. 3 481.

[66] K. R. Nayak, S. Koshti, S. V. Dhurandhar, and J.-Y. Vinet, *On the minimum flexing of LISA's arms*, *Classical and Quantum Gravity* **23** (2006), no. 5 1763.

[67] G. Li, Z. Yi, G. Heinzel, A. Rudiger, O. Jennrich, L. Wang, Y. Xia, F. Zeng, and H. Zhao, *Methods for orbit optimization for the LISA gravitational wave observatory*, *International Journal of Modern Physics D* **17** (2008), no. 07 1021–1042, [https://www.worldscientific.com/doi/pdf/10.1142/S021827180801267X].

[68] Y. Xia, G. Li, G. Heinzel, A. Rüdiger, and Y. Luo, *Orbit design for the laser interferometer space antenna (LISA)*, *Science China Physics, Mechanics and Astronomy* **53** (Jan, 2010) 179–186.

[69] M. Tinto and S. V. Dhurandhar, *Time-delay interferometry*, *Living Reviews in Relativity* **17** (Aug, 2014) 6.

[70] M. Tinto and J. W. Armstrong, *Cancellation of laser noise in an unequal-arm interferometer detector of gravitational radiation*, *Phys. Rev. D* **59** (Apr, 1999) 102003.

[71] M. Tinto, J. W. Armstrong, and F. B. Estabrook, *Discriminating a gravitational wave background from instrumental noise in the LISA detector*, *Phys. Rev. D* **63** (Dec, 2000) 021101.

[72] O. Gerberding, K.-S. Isleif, M. Mehmet, K. Danzmann, and G. Heinzel, *Laser-frequency stabilization via a quasimonolithic mach-zehnder interferometer with arms of unequal length and balanced dc readout*, *Phys. Rev. Applied* **7** (Feb, 2017) 024027.

[73] R. W. P. Drever, J. L. Hall, F. V. Kowalski, J. Hough, G. M. Ford, A. J. Munley, and H. Ward, *Laser phase and frequency stabilization using an optical resonator*, *Applied Physics B* **31** (Jun, 1983) 97–105.

[74] J. I. Thorpe, K. Numata, and J. Livas, *Laser frequency stabilization and control through offset sideband locking to optical cavities*, *Opt. Express* **16** (Sep, 2008) 15980–15990.

[75] P. Kwee, C. Bogan, K. Danzmann, M. Frede, H. Kim, P. King, J. Pöld, O. Puncken, R. L. Savage, F. Seifert, P. Wessels, L. Winkelmann, and B. Willke, *Stabilized high-power laser system for the gravitational wave detector advanced LIGO*, *Opt. Express* **20** (May, 2012) 10617–10634.

[76] K. Numata, A. Kemery, and J. Camp, *Thermal-noise limit in the frequency stabilization of lasers with rigid cavities*, *Phys. Rev. Lett.* **93** (Dec, 2004) 250602.

[77] A. Wade, *New ways to squeeze: Compact integraded waveguide non-linear devices*, Tech. Rep. LIGO-G1700231, 2017.

[78] S. Chelkowski, H. Vahlbruch, K. Danzmann, and R. Schnabel, *Coherent control of broadband vacuum squeezing*, *Phys. Rev. A* **75** (Apr, 2007) 043814.

[79] H. Vahlbruch, S. Chelkowski, B. Hage, A. Franzen, K. Danzmann, and R. Schnabel, *Coherent control of vacuum squeezing in the gravitational-wave detection band*, *Phys. Rev. Lett.* **97** (Jul, 2006) 011101.

[80] A. E. Siegman, *Lasers*. University Science Books, Sausalito, California, 1986.

[81] K. Patterson and S. Pellegrino, *Ultralightweight deformable mirrors*, *Appl. Opt.* **52** (Aug, 2013) 5327–5341.

[82] S. P. Kate Jackson, J. Kent Wallace, *Co-phasing primary mirror segments of an optical space telescope using a long stroke zernike wfs*, 2016.

[83] Patterson Keith, Yamamoto Namiko, and Pellegrino Sergio, *Thin deformable mirrors for a reconfigurable space telescope*. Structures, Structural Dynamics, and Materials and Co-located Conferences. American Institute of Aeronautics and Astronautics, apr, 2012. doi:10.2514/6.2012-1668.

[84] J. Steeves, K. Jackson, S. Pellegrino, D. Redding, J. K. Wallace, S. C. Bradford, and T. Barbee, *Multilayer active shell mirrors for space telescopes*, 2016.

[85] J. Steeves, I. Laslandesa, S. Pellegrinoa, D. Reddingb, S. B. Case, and Bradfordb, *Design, fabrication and testing of active carbon shell mirrors for space telescope applications*, 2015.

[86] B. L. Schumaker, *Disturbance reduction requirements for LISA*, *Classical and Quantum Gravity* **20** (2003), no. 10 S239.

[87] LISA Pathfinder Collaboration, *Charge-induced force noise on free-falling test masses: Results from LISA pathfinder*, *Phys. Rev. Lett.* **118** (Apr, 2017) 171101.

[88] J. Hanson, G. M. Keiser, S. Buchman, R. Byer, D. Lauben, D. DeBra, S. Williams, D. Gill, B. Shelef, and G. Shelef, *St-7 gravitational reference sensor: analysis of magnetic noise sources*, *Classical and Quantum Gravity* **20** (2003), no. 10 S109.

[89] A. Cavalleri, G. Ciani, R. Dolesi, A. Heptonstall, M. Hueller, D. Nicolodi, S. Rowan, D. Tombolato, S. Vitale, P. J. Wass, and W. J. Weber, *Increased brownian force noise from molecular impacts in a constrained volume*, *Phys. Rev. Lett.* **103** (Sep, 2009) 140601.

[90] A. Cavalleri, G. Ciani, R. Dolesi, M. Hueller, D. Nicolodi, D. Tombolato, S. Vitale, P. Wass, and W. Weber, *Gas damping force noise on a macroscopic test body in an infinite gas reservoir*, *Physics Letters A* **374** (2010), no. 34 3365 – 3369.

[91] R. Dolesi, M. Hueller, D. Nicolodi, D. Tombolato, S. Vitale, P. J. Wass, W. J. Weber, M. Evans, P. Fritschel, R. Weiss, J. H. Gundlach, C. A. Hagedorn, S. Schlamminger, G. Ciani, and A. Cavalleri, *Brownian force noise from molecular collisions and the sensitivity of advanced gravitational wave observatories*, *Phys. Rev. D* **84** (Sep, 2011) 063007.

[92] M. Evans, P. Fritschel, and R. Weiss, *Gas damping monte carlo*, Tech. Rep. LIGO-T0900582, 2011.

[93] L. Carbone, A. Cavalleri, G. Ciani, R. Dolesi, M. Hueller, D. Tombolato, S. Vitale, and W. J. Weber, *Thermal gradient-induced forces on geodesic reference masses for LISA*, *Phys. Rev. D* **76** (Nov, 2007) 102003.

[94] A. Cavalleri, G. Ciani, R. Dolesi, M. Hueller, D. Nicolodi, D. Tombolato, P. J. Wass, W. J. Weber, S. Vitale, and L. Carbone, *Direct force measurements for testing the LISA pathfinder gravitational reference sensor*, *Classical and Quantum Gravity* **26** (2009), no. 9 094012.

[95] R. Dolesi, D. Bortoluzzi, P. Bosetti, L. Carbone, A. Cavalleri, I. Cristofolini, M. DaLio, G. Fontana, V. Fontanari, B. Foulon, C. D. Hoyle, M. Hueller, F. Nappo, P. Sarra, D. N. A. Shaul, T. Sumner, W. J. Weber, and S. Vitale,

Gravitational sensor for LISA and its technology demonstration mission, *Classical and Quantum Gravity* **20** (2003), no. 10 S99.

[96] Y. Levin, *Internal thermal noise in the LIGO test masses: A direct approach*, *Phys. Rev. D* **57** (Jan, 1998) 659–663.

[97] G. M. Harry, A. M. Gretarsson, P. R. Saulson, S. E. Kittelberger, S. D. Penn, W. J. Startin, S. Rowan, M. M. Fejer, D. R. M. Crooks, G. Cagnoli, J. Hough, and N. Nakagawa, *Thermal noise in interferometric gravitational wave detectors due to dielectric optical coatings*, *Classical and Quantum Gravity* **19** (2002), no. 5 897.

[98] Y. T. Liu and K. S. Thorne, *Thermoelastic noise and homogeneous thermal noise in finite sized gravitational-wave test masses*, *Phys. Rev. D* **62** (Nov, 2000) 122002.

[99] V. Braginsky, M. Gorodetsky, and S. Vyatchanin, *Thermodynamical fluctuations and photo-thermal shot noise in gravitational wave antennae*, *Physics Letters A* **264** (1999), no. 1 1 – 10.

[100] M. Cerdonio, L. Conti, A. Heidmann, and M. Pinard, *Thermoelastic effects at low temperatures and quantum limits in displacement measurements*, *Phys. Rev. D* **63** (Mar, 2001) 082003.

[101] Y. Levin, *Fluctuationdissipation theorem for thermo-refractive noise*, *Physics Letters A* **372** (2008), no. 12 1941 – 1944.

[102] K. Somiya, K. Kokeyama, and R. Nawrodt, *Remarks on thermoelastic effects at low temperatures and quantum limits in displacement measurements*, *Phys. Rev. D* **82** (Dec, 2010) 127101.

[103] M. M. Fejer, S. Rowan, G. Cagnoli, D. R. M. Crooks, A. Gretarsson, G. M. Harry, J. Hough, S. D. Penn, P. H. Sneddon, and S. P. Vyatchanin, *Thermoelastic dissipation in inhomogeneous media: loss measurements and displacement noise in coated test masses for interferometric gravitational wave detectors*, *Phys. Rev. D* **70** (Oct, 2004) 082003.

[104] V. Braginsky, M. Gorodetsky, and S. Vyatchanin, *Thermo-refractive noise in gravitational wave antennae*, *Physics Letters A* **271** (2000), no. 5 303 – 307.

[105] V. Braginsky and S. Vyatchanin, *Thermodynamical fluctuations in optical mirror coatings*, *Physics Letters A* **312** (2003), no. 3 244 – 255.

[106] M. Evans, S. Ballmer, M. Fejer, P. Fritschel, G. Harry, and G. Ogin, *Thermo-optic noise in coated mirrors for high-precision optical measurements*, *Phys. Rev. D* **78** (Nov, 2008) 102003.

[107] W. Yam, S. Gras, and M. Evans, *Multimaterial coatings with reduced thermal noise*, *Phys. Rev. D* **91** (Feb, 2015) 042002.

[108] J. Pap, M. Anklin, C. Frhlich, C. Wehrli, F. Varadi, and L. Floyd, *Variations in total solar and spectral irradiance as measured by the virgo experiment on soho*, *Advances in Space Research* **24** (1999), no. 2 215 – 224. Helioseismology and Solar Variability.

[109] L. Carbone, S. M. Aston, R. M. Cutler, A. Freise, J. Greenhalgh, J. Heefner, D. Hoyland, N. A. Lockerbie, D. Lodhia, N. A. Robertson, C. C. Speake, K. A. Strain, and A. Vecchio, *Sensors and actuators for the advanced LIGO mirror suspensions*, *Classical and Quantum Gravity* **29** (2012), no. 11 115005.

[110] LIGO Scientific Collaboration, *Sensitivity of the advanced ligo detectors at the beginning of gravitational wave astronomy*, *Phys. Rev. D* **93** (Jun, 2016) 112004.

[111] W. M. Folkner, F. Hechler, T. H. Sweetser, M. A. Vincent, and P. L. Bender, *Lisa orbit selection and stability*, *Classical and Quantum Gravity* **14** (1997), no. 6 1405.

[112] F. Hechler and W. Folkner, *Mission analysis for the laser interferometer space antenna (lisa) mission*, *Advances in Space Research* **32** (2003), no. 7 1277 – 1282. Fundamental Physics in Space.

[113] M. Vallisneri, *Use and abuse of the fisher information matrix in the assessment of gravitational-wave parameter-estimation prospects*, *Phys. Rev. D* **77** (Feb, 2008) 042001.

[114] C. Cutler and E. E. Flanagan, *Gravitational waves from merging compact binaries: How accurately can one extract the binary's parameters from the inspiral waveform?*, *Phys. Rev. D* **49** (Mar, 1994) 2658–2697.

[115] E. E. Flanagan and S. A. Hughes, *Measuring gravitational waves from binary black hole coalescences. i. signal to noise for inspiral, merger, and ringdown*, *Phys. Rev. D* **57** (Apr, 1998) 4535–4565.

[116] E. E. Flanagan and S. A. Hughes, *Measuring gravitational waves from binary black hole coalescences. ii. the waves' information and its extraction, with and without templates*, *Phys. Rev. D* **57** (Apr, 1998) 4566–4587.

[117] S. Steinlechner, B. W. Barr, A. S. Bell, S. L. Danilishin, A. Gläfke, C. Gräf, J.-S. Hennig, E. A. Houston, S. H. Huttner, S. S. Leavey, D. Pascucci, B. Sorazu, A. Spencer, K. A. Strain, J. Wright, and S. Hild, *Local-oscillator noise coupling in balanced homodyne readout for advanced gravitational wave detectors*, *Phys. Rev. D* **92** (Oct, 2015) 072009.

[118] E. Berti, A. Buonanno, and C. M. Will, *Estimating spinning binary parameters and testing alternative theories of gravity with LISA*, *Phys. Rev. D* **71** (Apr, 2005) 084025.

[119] L. Barack and C. Cutler, *LISA capture sources: Approximate waveforms, signal-to-noise ratios, and parameter estimation accuracy*, *Phys. Rev. D* **69** (Apr, 2004) 082005.

[120] W.-F. Feng, H.-T. Wang, X.-C. Hu, Y.-M. Hu, and Y. Wang, *Preliminary study on parameter estimation accuracy of supermassive black hole binary inspirals for TianQin*, arXiv:1901.0215.

[121] P. Ajith, S. Babak, Y. Chen, M. Hewitson, B. Krishnan, A. M. Sintes, J. T. Whelan, B. Brügmann, P. Diener, N. Dorband, J. Gonzalez, M. Hannam, S. Husa, D. Pollney, L. Rezzolla, L. Santamar´ia, U. Sperhake, and J. Thornburg, *Template bank for gravitational waveforms from coalescing binary black holes: Nonspinning binaries*, *Phys. Rev. D* **77** (May, 2008) 104017.

[122] P. Ajith, S. Babak, Y. Chen, M. Hewitson, B. Krishnan, J. T. Whelan, B. Brgmann, P. Diener, J. Gonzalez, M. Hannam, S. Husa, M. Koppitz, D. Pollney, L. Rezzolla, L. Santamara, A. M. Sintes, U. Sperhake, and J. Thornburg, *A phenomenological template family for black-hole coalescence waveforms*, *Classical and Quantum Gravity* **24** (2007), no. 19 S689.

[123] M. Maggiore, *Gravitation Waves: Theory and Experiments*, vol. 1. Oxford University Press, 2008.